Optical Layers for Thin-film Silicon Solar Cells

THÈSE N^{O} 5190 (2011)

PRÉSENTÉE LE 11 NOVEMBRE 2011

À LA FACULTÉ SCIENCES ET TECHNIQUES DE L'INGÉNIEUR
LABORATOIRE DE PHOTOVOLTAÏQUE ET COUCHES MINCES ÉLECTRONIQUES
PROGRAMME DOCTORAL EN SCIENCE ET GÉNIE DES MATÉRIAUX

ÉCOLE POLYTECHNIQUE FÉDÉRALE DE LAUSANNE

POUR L'OBTENTION DU GRADE DE DOCTEUR ÈS SCIENCES

PAR

Peter CUONY (BUEHLMANN)

acceptée sur proposition du jury:

Prof. C. Hébert, présidente du jury
Prof. C. Ballif, Dr M. Despeisse, directeurs de thèse
Dr A. Howling, rapporteur
Prof. B. Rech, rapporteur
Dr T. Roschek, rapporteur

ÉCOLE POLYTECHNIQUE
FÉDÉRALE DE LAUSANNE

Suisse
2011

Résumé en Français

Dans ce travail nous avons développé et analysé différentes couches constitutives de cellules solaires Micromorphes en vue d'améliorer leurs propriétés optiques. Une cellule Micromorphe est une configuration tandem intégrant une cellule supérieure en silicium amorphe et une cellule inférieure en silicium microcristallin. La morphologie de l'électrode antérieure a un rôle décisif dans l'optimisation du rendement de ces cellules solaires. Pour une meilleure compréhension des exigences de la surface de l'électrode antérieure, nous présentons une large gamme de morphologies qui peuvent être obtenues avec de l'oxyde de zinc (ZnO) rugueux et des traitements de surface par plasma d'argon. Notre travail permet de corréler les paramètres morphologiques de l'électrode avec la diffusion de la lumière en transmission et en réflexion ; nous identifions les angles d'inclinaison des pyramides de ZnO comme étant le paramètre le plus pertinent pour leur application dans les cellules solaires en couche mince de silicium. Nous montrons qu'il n'y a pas de pertes par réflexion à l'interface entre le ZnO rugueux et le silicium, et nous quantifions les pertes par réflexion pour des interfaces plus lisses. Avec du dioxyde de titane, produit par pulvérisation cathodique réactive, nous montrons que des pertes par réflexion jusqu'à 7,4% peuvent être annulées pour une longueur d'onde de 550 nm. Au lieu d'insérer un matériau additionnel, nous montrons qu'un oxyde de silicium (SiO_x) avec un dopage de type p, peut également être utilisé dans une cellule en silicium microcristalline pour réduire les pertes par réflexion, tout en agissant comme couche dopée pour créer le champ électrique nécessaire pour séparer les porteurs photo-générés.

Nous montrons les caractéristiques optiques et électriques de couches SiO_x ; avec la microscopie électronique à transmission filtrée en énergie, nous révélons leur nanostructure filamenteuse. Un découplage partiel des propriétés électriques et optiques est obtenu pour de tels films, permettant la réalisation de films transparents avec un faible indice de réfraction (dû à la matrice d'oxyde de silicium) tout en conservant une conductivité transversale suffisante pour l'utilisation dans les cellules solaires (grâce aux filaments en silicium de quelques

nanomètres de largeur). Pour les cellules solaires en couches minces de silicium, nous montrons qu'une couche $SiO_{x\sim0.5}$ de type p est optimale comme couche d'entrée de la lumière, alors qu'une couche $SiO_{x\sim1}$ de type n, fortement dopée au phosphore, est la plus adaptée pour une utilisation comme couche réfléchissante intermédiaire dans des cellules tandem grâce à son faible indice de réfraction de 1.8. La résistance ajustable par le contrôle de la phase silicium dans les couches dopées SiO_x peut être utilisée à divers endroits dans la cellule Micromorphe pour réduire l'influence de zones poreuses sur les performances électriques de la cellule. La mise en œuvre de ces différentes fonctionnalités dans les cellules Micromorphes a considérablement contribué à augmenter le meilleur rendement initial de 11,8% en 2006 à 13,5% en 2010.

Le ZnO rugueux et le réflecteur intermédiaire en SiO_x aident à améliorer l'efficacité des cellules Micromorphes ; cependant, nous montrons qu'ils peuvent également rendre les dispositifs plus sensibles à des effets de dégradation liés à la vapeur d'eau. Par thermographie, nous démontrons que la contamination de l'eau affecte principalement les bords de cellule, ce qui a pour conséquence une distribution non uniforme de la tension de circuit-ouvert locale. Enfin, nous montrons comment l'absorption des porteurs libres et des plasmons de surface peuvent réduire la réflectivité du réflecteur postérieur et nous présentons des résultats préliminaires en vue de la réalisation d'un réflecteur postérieur sans absorption utilisant un ZnO poli en combinaison avec une couche d'argent.

Mots-clés:
Couche minces, cellules solaires, Micromorphe, silicium amorphe, silicium microcristallin, oxyde de zinc, oxyde de titane, oxyde de silicium, argent, antireflet, réflecteur intermédiaire, réflecteur postérieur, conductivité transverse, mélange de phases, séparation de phases, nanostructure, filaments, EFTEM, rugosité, morphologie de surface, angles d'inclinaison, SOIR, SOIR asymétrique, rendements, dégradation V_{oc}, stabilité V_{oc}, absorption par plasmon.

Abstract

In this work we develop and analyze optical layers for use in Micromorph solar cells, a tandem configuration with an amorphous silicon top cell and a microcrystalline silicon bottom cell. The morphology of the front electrode has a decisive role in maximizing the efficiency of a solar cell. To reach a better understanding of the requirements for the front electrode surface, we present a wide range of morphologies that can be obtained with as-grown rough zinc oxide (ZnO) and post-deposition argon plasma surface treatments. We correlate the morphological parameters to light scattering in transmission and reflection, and identify the inclination angles of ZnO pyramids as the most pertinent parameter for thin-film silicon solar cells. We show that there are no reflection losses at the interface between as-grown rough ZnO and silicon, and we quantify the reflection losses for smoother interfaces. With titanium dioxide, produced by reactive magnetron sputtering, we demonstrate that for flat interfaces reflection losses of up to 7.4% can be canceled at 550 nm wavelength. We show that in microcrystalline silicon cells p-type silicon sub-oxide (SiO_x) can also be used to reduce reflection losses, and at the same time can act as field-creating window layer.

We develop a wide range of mixed-phase SiO_x layers and with energy-filtered transmission electron microscopy we reveal the filamentous nanostructure of films produced with high hydrogen dilution of the precursor gas mixture. A partial decoupling of electrical and optical parameters is achieved for such films, where the transparency and the refractive index are determined mostly by the silicon oxide matrix, while sufficient transverse conductivity for the use in solar cells is maintained by few-nanometer-wide silicon filaments. In thin-film silicon solar cells, p-type $SiO_{x\sim0.5}$ shows the best results as a window layer with enhanced transparency, while strongly phosphorous-doped n-type $SiO_{x\sim1}$ is best suited for use as an intermediate reflecting layer in tandem cells due to a low refractive index of 1.8 with sufficient transverse conductivity. The tunable resistance of doped SiO_x layers can be used at various locations in a Micromorph cell to quench shunts or bad diodes in spatially non-uniform devices. Implementation of SiO_x

with these three functionalities in Micromorph cells has significantly contributed to increasing the best initial efficiency from 11.8% in 2006 to 13.5% in 2010.
While rough ZnO front electrodes and SiO_x-based intermediate reflecting layers both help to improve Micromorph cell efficiencies, they render the devices more sensitive to water-vapor-induced degradation. With lock-in thermography measurements we demonstrate that water contamination affects mainly the cell borders resulting in non-uniform distribution of the local open circuit voltage. Finally we show how free-carrier absorption and surface plasmon polariton absorption can reduce the reflectivity of the back reflector, and we present preliminary results aimed toward the realization of an absorption-free back reflector making use of polished ZnO and sputtered silver layers.

Key words:
optical layers, thin-film, silicon, solar cells, Micromorph, amorphous silicon, microcrystalline silicon, zinc oxide, titanium dioxide, silicon oxide, silver, anti-reflection, intermediate reflector, back reflector, shunt quenching, transverse conductivity, mixed-phase, phase separation, nanostructure, silicon filaments, filamentous SiO_x, EFTEM, energy-filtered transmission electron microscopy, roughness, surface morphology, inclination angles, SOIR, asymmetric SOIR, tunneling recombination junction, V_{oc} degradation, V_{oc} stability, surface plasmon absorption

A copy of this document can be downloaded from http://peter.cuony.ch/PhD/

Written contributions of Peter Cuony (Buehlmann):

- Articles as first author: [1-7]
- Patents: [8,9]
- Articles as co-author: [10-25]

Oral contributions of Peter Cuony (Buehlmann):

- Presentation at MRS fall meeting 2008 in Boston, USA.
- Presentation at ICANS 2009 in Utrecht, NL.
- Presentation at MRS spring meeting 2011 in San Francisco, USA.

Poster contributions of Peter Cuony (Buehlmann):

- 22nd EU-PVSEC 2007 in Milano, IT.
- 25th EU-PVSEC 2010 in Valencia, ES.

Remark: I changed my name from Buehlmann to Cuony at my marriage in 2008.

1 Introduction

In this PhD thesis report we present different materials that are used in thin-film silicon solar cells to enhance the absorption of light and so increase the solar cell conversion efficiency. More specifically, these optical layers are developed for the Micromorph cell, which is a tandem configuration with an amorphous silicon (a-Si) top cell and a microcrystalline silicon (µc-Si) bottom cell. In this chapter we first motivate our research in photovoltaics (PV) and put it in context with the exciting evolution of the PV market in the recent years. Then, we give a short introduction to thin-film silicon solar cells, describe the current status of research on thin-film silicon solar cells, draw the outline of this thesis report, and point out the main contribution of this work to the field of research.

1.1 Current status of photovoltaics for energy production

Fossil fuels are non-renewable, their reserves are limited and their exploitation causes pollution, war, and global warming. They will therefore be replaced by renewable energies in the future. The sun is by far the biggest source of renewable energy with 86 PW of solar radiation reaching the earth's surface.[26] If absorbed, this radiation can be converted, for example, into heat, into electricity (photovoltaic effect), into biomass (photosynthesis), and into potential energy (evaporation of water). The advantage of the photovoltaic effect is that solar radiation is converted directly into electricity, a "noble" form of energy, which can be easily transported and converted into other energies. Furthermore, the photovoltaic effect requires only small quantities of photo-active materials (0.2–200 µm thick layers of a semiconductor such as silicon), hardly needs maintenance, and requires no consumables. If covered with PV modules with 10% efficiency, 1/10 of the surface of the Sahara desert could produce the equivalent of the global energy consumption.

In the year 2000, the German government acknowledged the potential of renewable energy sources including photovoltaics (PV) for large-scale energy production by implementation of a strong market-introduction law. This has led to an exponential growth of the worldwide PV market with growth rates of 40% per year as illustrated Figure 1-1 (a). In 2010, PV was the second most important technology with respect to its increase in peak electricity production capacity. As PV is a stochastic energy source, it has to be normalized to its equivalent full-time energy production capacity as illustrated in Figure 1-1 (b). Nonetheless, considering this corrected comparison, the full-time equivalent PV capacity in 2010 was still in fourth place of all energy sources and in second place for renewable energies, with almost unlimited potential

for further growth. The European Photovoltaic Industry Association forecasts that 20% of the world electricity demand could be covered by PV in 2050.[27] The more conservative International Energy Agency predicts that in 2050, 22% of the electricity demand worldwide could be covered by combined PV and thermal concentrated solar power (CSP) capacities.[28]

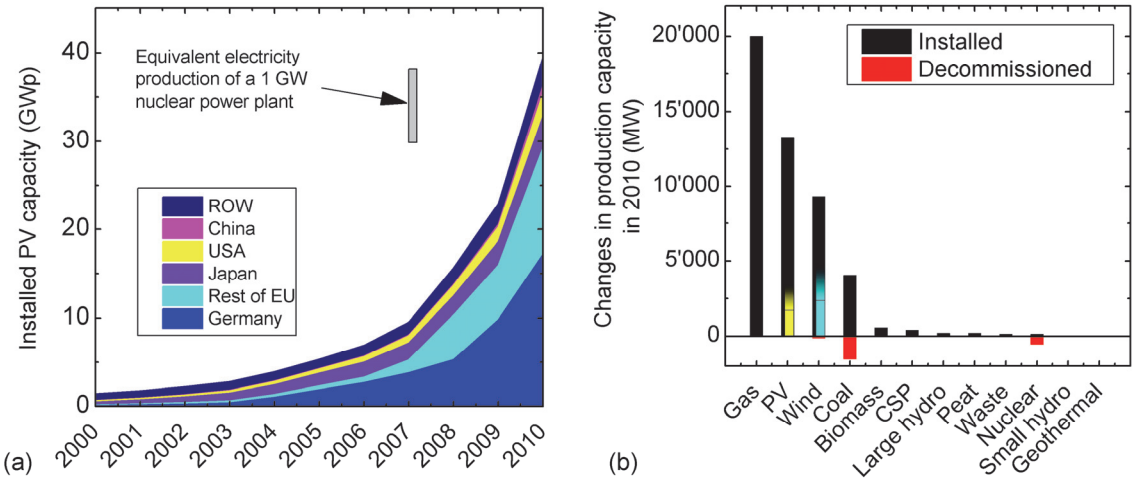

Figure 1-1: (a) Evolution of installed PV capacity.[29] (b) Newly installed and decommissioned electricity production capacities in 2010 for different technologies.[29] PV and wind power are stochastic energy sources and their full production capacity is rarely reached. The yellow and blue bars represent the equivalent full-time production capacity, which is typically a factor 4–8 lower than the nominal installed capacity for PV, and a factor 2–4 lower for wind, depending on the localization.

Due to increasing production levels and continuous product improvements, this exponential growth has led to a decrease of PV module prices as illustrated in Figure 1-2 (a). PV electricity costs (in SFr/kWh) depend not only on PV module prices, but also on installation and maintenance expenses, solar irradiation, and capital interest rates. In summer 2011, the "Services Industriels de Genève (SIG)" started construction of a 4.2 MWp PV plant on the roof of Palexpo, an exposition hall in Geneva, Switzerland. The cost of this installation is 15 million SFr and will be amortized over 25 years. When taking into account a capital interest rate of 5%, annual maintenance costs of 1%, and a yearly drop of solar module power of 1%, the PV electricity from this installation will cost 0.32 SFr/kWh. In contrast, looking at more developed markets in Germany and Italy, Photon International Magazine writes, that the least expensive turn-key PV systems in Europe are currently installed at ~2 €/Wp. If installed in southern Europe, using the same amortization calculations as in the previous example, the lower PV system price and the higher solar yield result in a PV electricity cost of 0.13 €/kWh for such installations. As the costs to generate PV electricity are expected to further decrease significantly in the future, it seems probable that PV will soon become competitive with traditional energy sources, which will set an end to the feed-in tariffs put in place for the market introduction of PV.

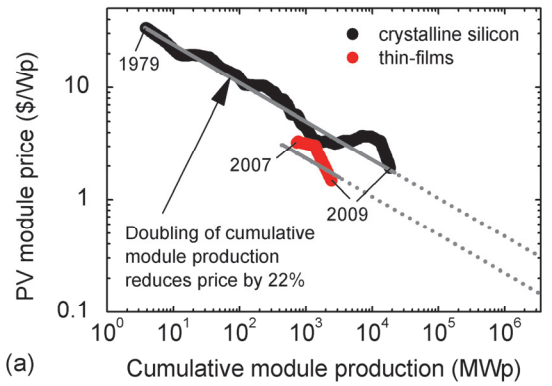

(a)

Solar yield and interest rates / PV system cost		SIG, Geneva (3.6 SFr/Wp)	best system prices (2.0 €/Wp)
Switzerland roof-mounted (1.0 kWh/Wp)	0%	0.19 SFr/kWh	0.11 €/kWh
	5%	0.32 SFr/kWh	0.18 €/kWh
South of Europe (1.5 kWh/Wp)	0%	0.13 SFr/kWh	0.07 €/kWh
	5%	0.22 SFr/kWh	0.12 €/kWh

(b)

Figure 1-2: (a) Learning curve of PV.[30] (b) PV electricity costs and their dependence on solar irradiation and capital interest rates.

In 2010, worldwide energy consumption was approximately 8'800 Mtoe (mega tons of oil equivalent), of which 17 % was consumed in the form of electricity. If 20% of the worldwide electricity consumption is to be covered by PV (3.4 % of the energy consumption), then we would need an installed PV capacity of ~3.5 TWp. From the learning curve of PV, shown in Figure 1-2 (a) it can be seen that PV module prices have decreased by a factor of 20 over the last 30 years, mostly due to the German feed-in tariffs and that module prices well below 1.0 $/Wp are likely to be reached when going towards a self-sustained worldwide deployment of PV for energy production.

Thin-film technologies entered the PV market a few years ago, and have demonstrated the capacity to achieve lower module prices than crystalline silicon technologies. Amongst the thin-film PV modules available in 2011, there are three main technologies, (the following numbers are from Photon International Magazine). First, cadmium telluride (CdTe) technology has the largest market share with 1.45 GWp of modules produced in 2010. The current industrial leader in this technology is First Solar with the highest full module efficiencies of 13.5% and currently the lowest, self-declared PV module production costs of 0.75 $/Wp. Second, thin-film silicon technologies produced 1.36 GWp of modules in 2010. This technology has the largest growth potential because it does not rely on rare earth materials such as tellurium, indium or gallium. There are several market leaders in Europe, USA and Asia including clients from Oerlikon Solar, a Swiss turn-key production line supplier. Amongst the different thin-film silicon configurations, the Micromorph cell on glass is currently the most successful. Sharp, a Japanese company inaugurated 160 MWp factory in July 2011 in Italy and Oerlikon Solar sold a 120 MWp production line to be ramped up in Asia in 2012; both claiming to produce Micromorph modules with 10% stabilized efficiency. Third, there are the rapidly emerging copper-indium-gallium-selenide (CIGS) technologies with 0.44 GWp of modules produced in 2010 but estimated cell production capacity of 2.17 GWp by the end of 2011. This sector is led by Solar Frontier, who is currently ramping up a 900 MWp factory and has highest module efficiencies of 12.2%.

1.2 Thin-film silicon solar cells

Thin-film silicon solar cells consist of a layer stack of p-type, intrinsic, and n-type silicon and silicon alloy materials. P- and n-type doping are achieved by incorporating boron or phosphorous atoms into the films. The doped layers are not photo-active due to their high electronic defect density, but they are necessary to create an electric field in the intrinsic absorber layer in order to collect the photo-generated electron-hole pairs. Transparent conducting oxide (TCO) layers are used to extract the charge carriers from the silicon p-i-n junction. Thin-film silicon solar cells are usually oriented such that light enters the absorber layer through the p-layer. When depositing on an opaque substrate, the n-layer is deposited first and the p-layer last. This structure is called n-i-p, indicating the order of deposition. In this report we focus on p-i-n structures, making use of a transparent glass substrate, where the p-type layer is the first silicon layer deposited. The two main absorber materials used to fabricate thin-film silicon solar cells are hydrogenated amorphous silicon (a-Si) and hydrogenated microcrystalline silicon (µc-Si) with respective band gaps of 1.7 and 1.1 eV. The combination of these two absorbers leads to an a-Si/µc-Si tandem cell, first presented by IMT,[31] called the Micromorph cell. The schematic in Figure 1-3 illustrates this configuration, which is currently the most promising thin-film silicon candidate to compete with traditional crystalline silicon technologies. More details about the fundamental material and device properties can be read in the recently published book "Thin-Film Silicon Solar Cells" edited by Arvind Shah.[32]

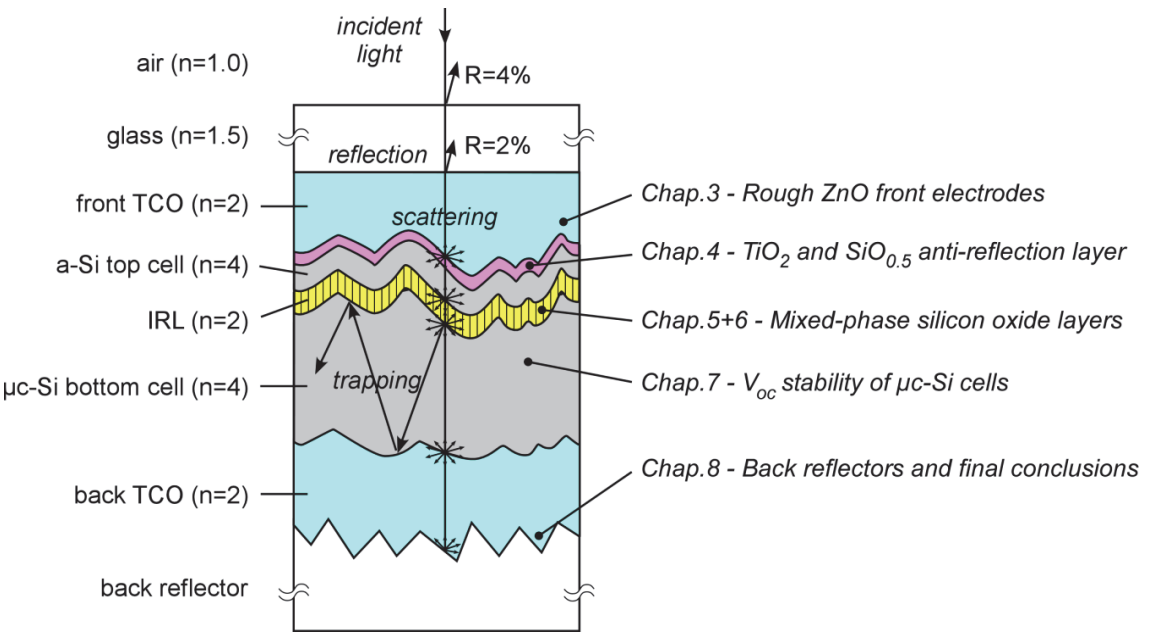

Figure 1-3: Schematic of a Micromorph tandem cell with the different cell parts presented on the left and the outline of this PhD thesis report shown on the right.

Traditional crystalline silicon solar cells are typically 200 µm thick, which is sufficient to absorb a large part of the solar spectrum with energy higher than the band gap of silicon at 1.12 eV. Contrary to this standard PV technology, the intrinsic absorber layers in thin-film silicon solar

cells are usually kept below 300 nm for a-Si and below 3 µm for µc-Si, because of the relatively high electronic defect density in thin-film silicon, which makes collection of photo-generated electron-hole pairs difficult in thicker layers. The problem with thin layers is that they do not absorb all the light due to the low absorption coefficient of silicon in the red and near infrared range (Figure 1-4 (a)). This means that energetic photons are easily absorbed by the thin silicon layers (over 95% for wavelengths < 500 nm in 200 nm a-Si and over 95% for wavelengths < 600 nm in 3 µm µc-Si), but photons with lower energies need much longer distances to be absorbed. Nevertheless, it is possible to achieve high currents in the thin-film silicon solar cells by increasing the optical path of the light within the thin absorber layer. This is generally realized by scattering the light at the rough interfaces between the TCO and the silicon absorber layers. Because the refractive index of silicon is higher than that of the front and back TCO layers, light can be trapped to some extent, traveling back and forth in the silicon layer until it is finally absorbed. Figure 1-4 (b) shows the number of photons in the solar spectrum and the dashed surfaces indicate the number of electrons that are converted into electrons in a Micromorph cell under short-circuit conditions. The a-Si cell used in this example is 240 nm thick but absorbs photons in the infrared part of the spectrum like a 720 nm thick a-Si layer, thanks to the light trapping induced by the rough interfaces and the intermediate reflecting layer. Similarly, the 2.8 µm thick µc-Si cell converts photons at around 900 nm as efficiently as a 28 µm thick µc-Si layer, due to the roughness and the back reflector.

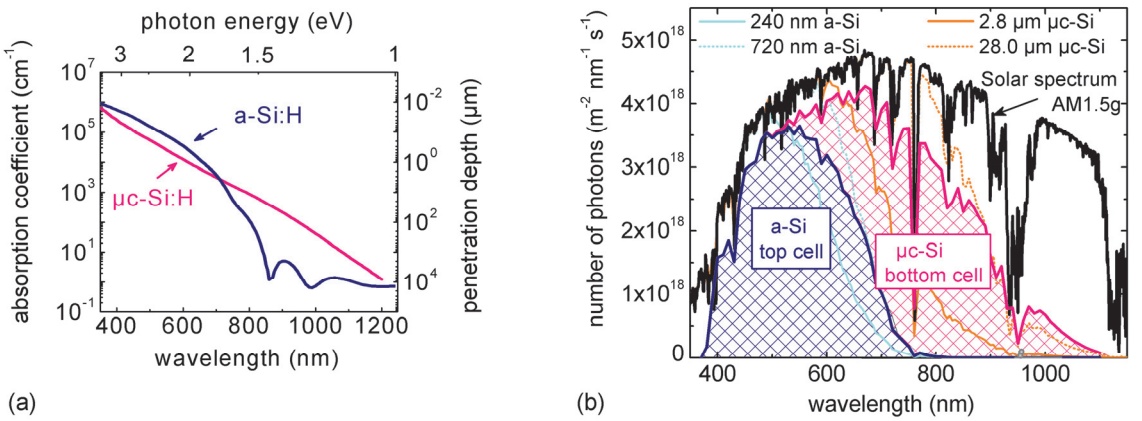

Figure 1-4: (a) Absorption coefficient of a-Si:H and µc-Si:H taken from SunShine software.[33] (b) Number of photons as a function of wavelength for the solar spectrum AM1.5g. The patterned surface represents the useful absorption in an optimized Micromorph solar cell with 240 nm thick a-Si and 2.8 µm thick µc-Si absorber layers and an 80 nm thick intermediate reflecting layer. The light blue and magenta lines present the calculated absorption by a single-pass in silicon layers with different thicknesses.

1.3 Status of the research on Micromorph solar cells

The Micromorph cell, also called a hybrid cell or a-Si/µc-Si tandem cell, is composed of a glass substrate, a front TCO electrode, an a-Si top cell, possibly an intermediate reflecting layer (IRL), a µc-Si bottom cell, a back TCO electrode, and a back reflector (see Figure 1-3). In order to enhance light coupling into and light trapping in the silicon layers, rough front electrodes such as tin oxide (SnO_2)[34] and zinc oxide (ZnO)[35-37] are commonly used. The silicon layer stack of a p-i-n/p-i-n Micromorph cell on a ZnO front electrode is typically fabricated as follows: First a few nanometers of p-µc-Si is deposited in order to make good electrical contact with the ZnO.[38] Second a ~15 nm thick p-type silicon carbide layer is used as a field-creating window layer,[39] which third, is usually followed by an intrinsic silicon carbide or wide-gap i-a-Si layer to create a graded interface and increase the carrier collection .[40,41] Fourth, a ~200 nm thick i-a-Si absorber layer is deposited. A low defect density and high stability to light exposure are important in this layer to achieve good cell results.[42,43] Fifth, an n-a-Si layer is grown onto the i-a-Si layer in order to create a charge-separating electrical field in the absorber layer, in combination with the p-SiC layer. Sixth, a short carbon dioxide plasma preceding the n-µc-Si layer allows for rapid nucleation, necessary to obtain a good tunneling recombination junction with the p-layer from the bottom cell.[44] Next, the µc-Si p-i-n layers are deposited to form the µc-Si bottom cell.[45] A low level of oxygen contamination in the i-µc-Si layer[46] and a Raman crystalline fraction of 30–60%[47,48] were shown to yield the best i-µc-Si cell results. In the doped µc-Si layers, a higher Raman crystalline fraction of ~80% is desirable and contamination is not a critical issue. Finally, a thin-ZnO/silver[49] or a thick-ZnO/white-paint[50] stack is used as a back electrode and reflector.

Light management that improves the current produced by solar cells has been an important topic in recent years. The two challenges here are to maximize the path of infrared light (wavelengths 600–1100 nm) in the cell and at the same time reduce parasitic absorption losses in the doped layers, which are not photo-active. Currently, best results on light-path enhancement are achieved using random textures.[36,37,51] Periodic structures were shown to achieve better absorption than random textures for some wavelengths,[52,53] but have not been able to demonstrate superiority for the full spectrum of interest for Micromorph cells. Novel approaches to enhance light absorption were recently proposed with diffuse back electrodes[54] and optically thick/electrically thin concepts.[55,56] When the light-path is elongated in the absorber layer, it is often also elongated in the doped silicon layers and the TCOs leading to additional parasitic absorption losses that offset the current gain expected from light-path enhancement. As-grown rough ZnO with low free carrier density was shown be highly transparent for the full range of interest[57] and has played an important role in recently achieved world-record efficiencies.[58,59] Alloying the silicon doped layers with oxygen or carbon was shown to be a possibility to reduce parasitic absorption losses in the doped silicon layers.[39,60]

With regard to optical performance, rough front electrodes are necessary, but a limitation of the roughness is set by growth of spatially inhomogeneous silicon layers with less dense

material growing in the valleys of the substrate. These less dense regions in the absorber layers, also called cracks, have higher electronic defect densities, lead to a spatially non-uniform distribution of reverse saturation currents, and reduce the performance of thin-film silicon solar cells.[61-66] To maximize solar cell efficiency, one has therefore to fine-tune the front electrode morphology taking into account the trade-off between the optical and electrical performance of the solar cell.[22,67]

Another very important research topic in recent years is related to the industrialization of thin-film silicon technologies. Presently, one of the strongest industrial limitations of µc-Si is the relatively long time needed for its deposition. Deposition time can be reduced either by increasing the deposition rate for µc-Si or by reducing the µc-Si layer thickness. Promising results with high deposition rates have been demonstrated with the use of high-pressure deposition regimes[68-70] in standard parallel plate reactors or novel multi-hole or pyramid-shaped cathodes.[71,72] With advanced light management, good results were recently achieved using thin (~1 µm thick) µc-Si absorber layers.[73,74]

1.4 Structure of thesis report

In this work we investigate standard and novel optical layers for Micromorph solar cells (excluding photo-active silicon absorbers). In chapter 2, we briefly summarize the experimental techniques used to fabricate and characterize the different layers and devices presented in this thesis report. Chapters 3 to 8 contain the scientific contribution of this work. They are organized as illustrated in Figure 1-3, following the light through a Micromorph device. The first optical interfaces that light encounters are the flat air/glass and glass/ZnO interfaces, which cause 4% and 2% Fresnel reflection losses, respectively. These reflection losses can be reduced by industrially available anti-reflection coatings applied to the glass, and are not addressed in this work. Chapter 3 describes the different rough ZnO morphologies used throughout this work and identifies the inclination angles of the rough surfaces as the most pertinent morphology parameter. The necessity for this chapter becomes clear in the other chapters, because almost all the subsequent results depend on the roughness that is chosen for the front electrode. In chapter 4 we present how reflection at the ZnO/Si interface relates to the ZnO surface morphology and demonstrate that titanium dioxide and silicon oxide can be used as anti-reflection layers. Chapter 5 gives new insight into the material properties and nanostructure of mixed-phase silicon oxide layers and chapter 6 elucidates four different functionalities of this material in Micromorph solar cells. In chapter 7 we examine how rough front electrodes or porous intermediate reflecting layers can promote the in-diffusion of water vapor into the µc-Si layer, causing a strong degradation of the cell's border regions, which leads to a loss of the device's open-circuit voltage. In chapter 8 we round up the work by presenting preliminary results on the back reflector before finishing with the final conclusions in chapter 9.

1.5 Contribution of this work to the research field

One of the main contributions of this work is the analysis and quantification of the influence of rough optical interfaces on solar cell performance. Whereas most of the previous research on thin-film silicon solar cells was based on experiments carried out on a single front electrode surface morphology, we analyze reflection and transmission as a function of roughness at the different optical interfaces formed by the ZnO, silicon, and back reflector layers. For as-grown rough ZnO with a thickness >1 µm we identify the inclination angles of the features as a more useful quantity than commonly used roughness parameters.

A second contribution is the development, characterization, and analysis of mixed phase-silicon oxide layers (SiO_x) as well as their implementation in thin-film silicon solar cells. We demonstrate that a SiO_x layer deposited with high hydrogen dilution contains a filamentous nanostructure which allows for transparent, but conducting, films. We show that p-$SiO_{x\sim0.5}$ layers can reduce parasitic absorption losses and that n-$SiO_{x\sim1}$ is a multifunctional material suitable for use as an intermediate reflection layers.

A third contribution is related to negative impacts encountered when using as-grown rough ZnO with excellent optical properties. For µc-Si cells, we show that a resistive p-layer can mitigate the negative influence of cracks on the cells' electrical parameters, and we identify water-vapor-induced degradation as a main stability problem for cells deposited on rough front electrodes.

All the layers and cells presented in this thesis report were fabricated and measured by Peter Cuony, unless stated otherwise. An exception to this is the glass cleaning and the deposition of ZnO electrodes for solar cells; two procedures that were usually executed in batches for the whole lab.

2 Thin-film deposition and characterization techniques

In this chapter we describe the techniques used to fabricate and characterize the layers and solar cells presented in this thesis report. Widely used techniques in our field of research are addressed briefly and more details are given for some newly developed techniques or rarely described details.

2.1 Layer deposition techniques

2.1.1 The glass substrate

The standard substrate used in this work for solar cell and layer developments is a 0.5 mm thick AF45, an aluminoborosilicate glass produced by Schott. This glass is fabricated with a down-draw method: the liquid glass is poured out of a container and solidifies during the vertical downward flow in a purified atmosphere. Thin (0.05–0.5 mm) glasses can be fabricated by this method and surface contaminations, common on float glasses that solidify on a bath of molten tin, are avoided. The standard substrate size used in our lab is 82 x 41 mm^2 or 41 x 41 mm^2. Before the deposition of thin films, the glass is cleaned with the following manual process: Detergent is applied with a brush to both sides of the glasses and then rinsed off with deionized water (DI). Then a rack containing ~20 glasses is cleaned in different baths in the following order: 3’ in a DI ultrasonic bath at 60 °C with 0.8% deconex; 5’ in a DI bath with air-bubbles; 3’ in a DI ultrasonic bath at 60 °C with 0.8% tartaric acid; and 5’ in a DI bath with air-bubbles. Finally, the glass is rinsed with DI, dried in a cleanroom atmosphere in the vertical position and then stocked in boxes until it is used for deposition.

2.1.2 ZnO deposited by LP-CVD

As-grown rough ZnO is deposited by low pressure chemical vapor deposition (LP-CVD) using a precursor gas mixture of diethylzinc ($(C_2H_5)_2Zn$), water vapor (H_2O), and diborane (B_2H_6). The substrates are placed on a plate heated to ~180 °C, and the source gases are thermally decomposed near the substrate and form a boron-doped zinc oxide (ZnO:B) film with pyramidal surface features. The deposition rate is ~150 nm/min, and the layer thickness is varied by adjusting the deposition time. The surface roughness of the ZnO films (~size of ZnO pyramids) is mostly determined by the ZnO layer thickness. The following nomenclature is chosen in this work: Z1, for a 1 µm thick ZnO film, Z2 for a 2 µm thick film, etc. (see Figure 3-1, Figure 3-6, and Figure 3-7 for examples). Low doping levels are desirable in order to reduce the free-carrier absorption in the infrared part of the spectrum and the necessary sheet resistance ($R_{\square}$) is achieved by making 2–6 µm thick films. Films produced without B_2H_6 gas are called “un-

doped" or "non-intentionally doped" ZnO films and are still strongly n-type. Films with a $R_{\square}$ of 10 Ω can be achieved with a non-intentionally doped 6 µm thick film with a Hall mobility of 42 $cm^2V^{-1}s^{-1}$ and a carrier density of $3 \cdot 10^{19}$ cm^{-3}.[75]

2.1.3 Argon plasma surface treatment of LP-CVD ZnO

The sharp pyramids of the as-grown rough LP-CVD ZnO can be smoothened with an argon plasma surface treatment (ArST) in a reactive ion etching system from Integrated Plasma Limited (IPL). The IPL system contains a capacitively coupled radio frequency (RF) electrode with a circular surface of 320 cm^2 and a much larger grounded electrode. Both electrodes are water cooled. The ArST treatments are typically performed with a RF power of 200 W, and an argon pressure of 30 mTorr. During this process a self-bias DC voltage of -600 V is built up on the RF electrode by the plasma due to the asymmetry of the reactor. To describe the surface roughness obtained with LP-CVD ZnO and subsequent ArST we use the following nomenclature: Z1-Ar20' for a 1 µm thick ZnO layer exposed to 20' ArST; Z5-Ar60' for a 5 µm thick ZnO layer exposed to 60' ArST etc. (See Figure 3-3, Figure 3-6, and Figure 3-7 for examples)

2.1.4 Silicon and silicon alloys deposited by PECVD

The silicon and silicon alloy films are deposited by plasma enhanced chemical vapor deposition (PECVD). For the deposition of the hydrogenated silicon layers, silane (SiH_4) and hydrogen (H_2) are used as source gases. These gases do not thermally dissociate at the deposition temperatures between 180 °C and 230 °C and a plasma is used to enable their dissociation. By adding methane (CH_4) or carbon dioxide (CO_2) to the precursor gas mixture, a silicon carbide (SiC_x) or silicon oxide (SiO_x) alloy can be grown. With trimethylboron ($B(CH_3)_3$), abbreviated as TMB, and phosphine (PH_3), the silicon and silicon alloys can be doped p- and n-type, respectively. The following nomenclature is used for the silicon-based films: p-a-Si stands for a p-type hydrogenated amorphous silicon film; i-µc-Si for an intrinsic hydrogenated microcrystalline silicon film; and n-SiO_x for an n-type hydrogenated silicon sub-oxide film where the subscript x describes the ratio of oxygen to silicon atoms in the film.

The silicon and silicon alloy films presented in this work are deposited in three different reactors, which are named "sysB", "KaiS" and "KaiM". All those systems have a parallel plate configuration with a showerhead gas injection and a lateral pumping. The substrates are loaded through a load-lock in order to reduce the contamination of the deposition chambers. The electrode size and the process pressure and power ranges for these three reactors are summarized in the table below:

	electrode size (cm^2)	electrode gap (mm)	excitation freq. (MHz)	pressure range (mbar)	power range (W/cm^2)
sysB	10 x 10	15	70–122	0.2–0.7	0.02–0.16
KaiS	40 x 50	25	40	0.2–4.0	0.01–0.45
KaiM	50 x 60	13–25	13.5–40	2.0–7.0	0.10–0.50

Most of the SiO_x layers and solar cells presented in this work were fabricated in sysB shown in Figure 2-1, which is a dual-chamber reactor with dedicated chambers for intrinsic and doped layers. One particularity of this system is that it has small, asymmetric electrodes (the RF electrode is significantly smaller than the ground), which leads to a strong border effect.[76] This border effect can cause spatially in-homogeneous deposition rates, but for a limited range of process pressures and power densities, films with fairly uniform thickness can be obtained. Due to this limitation, the pressure and power are usually kept constant and are not used as optimization parameters. In these process windows with uniform film thickness, small non-uniformities in crystallinity or electrical conductivity still occur. For all the experiments done in this system, special attention is therefore paid to compare layer characteristics measured only on spots that are deposited at more than 3 cm from the border of the electrode. With these restrictions on process conditions and deposition regions, reproducible and comparable results could be obtained in sysB.

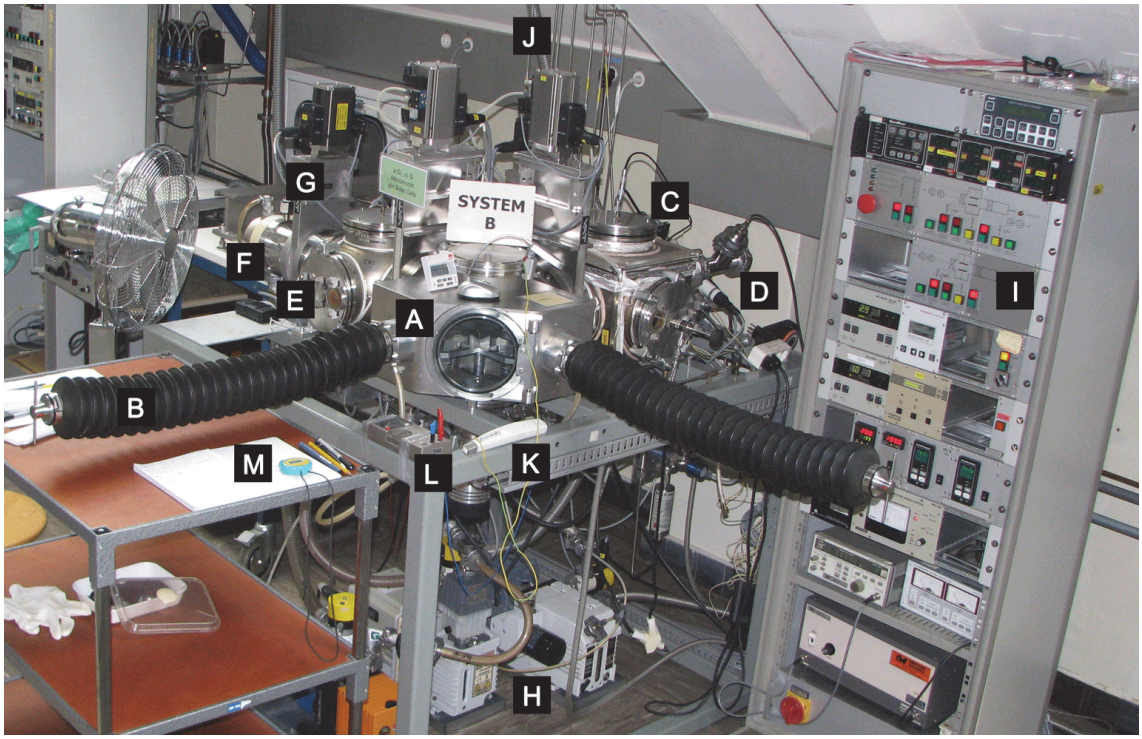

Figure 2-1: Photo of dual-chamber PECVD system "sysB". **A**: Load-lock chamber where the sample holder is placed by hand, **B**: Mechanical arm to move the sample holder to the PECVD chamber, **C**: PECVD chamber used to deposit doped layers, **D**: Gauges to measure chamber vacuum pressure, **E**: PECVD chamber used to deposit intrinsic layers, **F**: Turbo pumps connected directly to each of the three vacuum chambers, **G**: Valve, **H**: Three primary pumps, one after each turbo pump, **I**: Control tower to monitor and control chamber pressures, gas flows, electrode temperatures, and electrical power, **J**: Gas lines, **K**: Device to ignite the plasma with a spark, **L**: Voltmeter to measure the electrode DC-bias, **M**: Chronometer used to control layer deposition time.

2.1.6 TiO_2 deposited by reactive magnetron sputtering

Titanium dioxide (TiO_2) layers are produced in the "R2D2" reactor by reactive magnetron sputtering of a titanium target in 5 µbar argon + 0.2 µbar water vapor (controlled with needle valves), without external heating, and with a power density of 3 W/cm^2 and a growth rate of ~ 2 nm/min. The optical properties of the produced TiO_2 films are reproducible and do not vary significantly by changing the deposition conditions within a limited range. The required transverse conductivity is achieved in some runs, but with poor reproducibility. Small variations in the gas mixtures that change the degree of target oxidation in the sensitive metallic/oxide transition region[77] are believed to be the main causes for the poor reproducibility of the transverse conductivity. In the cell configuration, the ~60 nm thick TiO_2 layer is always covered by a 10 nm thick ZnO, produced in the same system, in order to protect the TiO_2 from H_2-induced reduction during the subsequent silicon cell deposition.[78]

2.2 Layer characterization techniques

2.2.1 Spectroscopic transmittance and reflectance

The transmission and reflection of a thin film on a substrate are measured with a dual-beam spectrometer, type Lambda900 from Perking Elmer, with a spectral range from 320 nm to 2000 nm. An integrating sphere allows for measuring the total transmission and reflection, including both the specular and diffuse contributions. By opening a small hole in the integrating sphere it is possible to measure only the light that is scattered with an angle greater than 5° from normal incidence. The light intensity measurements are then divided by the reference measurements (no sample in transmission and perfect reflector in reflection) to obtain the transmittance and reflectance, which give the fraction of light that is transmitted through or that is reflected by the sample. The light-scattering capability of a sample can be expressed by its haze in transmission, which is the ratio of diffuse to total transmittance.

2.2.2 Ellipsometry

Spectroscopic ellipsometry measurements are carried out with a UVISEL instrument form Horiba Jobin Yvon with an incidence angle of 70° and a spectral range from 0.6–6 eV. The refractive index and absorption coefficient are determined with the DeltaPsi2 software, making use of a Marquardt minimization algorithm to fit the measurements to a model. The samples are modeled by a void/glass/oxide-film/roughness four-layer stack. A Tauc-Lorentz dispersion model is used to describe the SiO_x and TiO_2 materials, and the few-nanometer-thick roughness layers are modeled with an effective medium approximation with 50% void and 50% oxide-film material.

2.2.3 Fourier transform infrared spectroscopy (FTIR)

Infrared (IR) absorption measurements of SiO_x layers are performed with a Nicolet 8700 system from Thermo with a XT-KBr beam-splitter and a DTGS detector. Undoped, float zone silicon wafers from Semiconductor Wafer Inc. are used as substrates for the SiO_x thin-films to be measured. The thickness of the wafers is chosen to be the same as for the glass substrates (0.5 mm) to ease the co-deposition on different substrates in the deposition system (sysB), where samples are placed up-side down and covered with a metal plate. Figure 2-2 (a) shows the light intensity of a halogen lamp after passing through a two-side polished 0.5 mm thick silicon wafer as measured by the detector. Absorption peaks due to the H_2O and CO_2 contained in the air in the system are indicated, as well as a small dip due to the Si-O stretching mode absorption from the native oxide on the wafer surface. In order to reduce the absorption of IR light by air in the setup, the system can be purged with nitrogen. The absorption measurements are acquired with a resolution of 2 cm^{-1}, which allows for the chosen wafer thickness to average the interference fringes that appear when measuring with higher resolutions, as shown in Figure 2-2 (b). Figure 2-2 (c) shows the transmittance (ratio of intensity with wafer to intensity without wafer) of one- and two-side polished wafers. For two-side polished wafers the transmittance is ~60 % due to the reflection of light by the flat wafer interfaces. For the one-side polished wafer, the transmittance drops with increasing

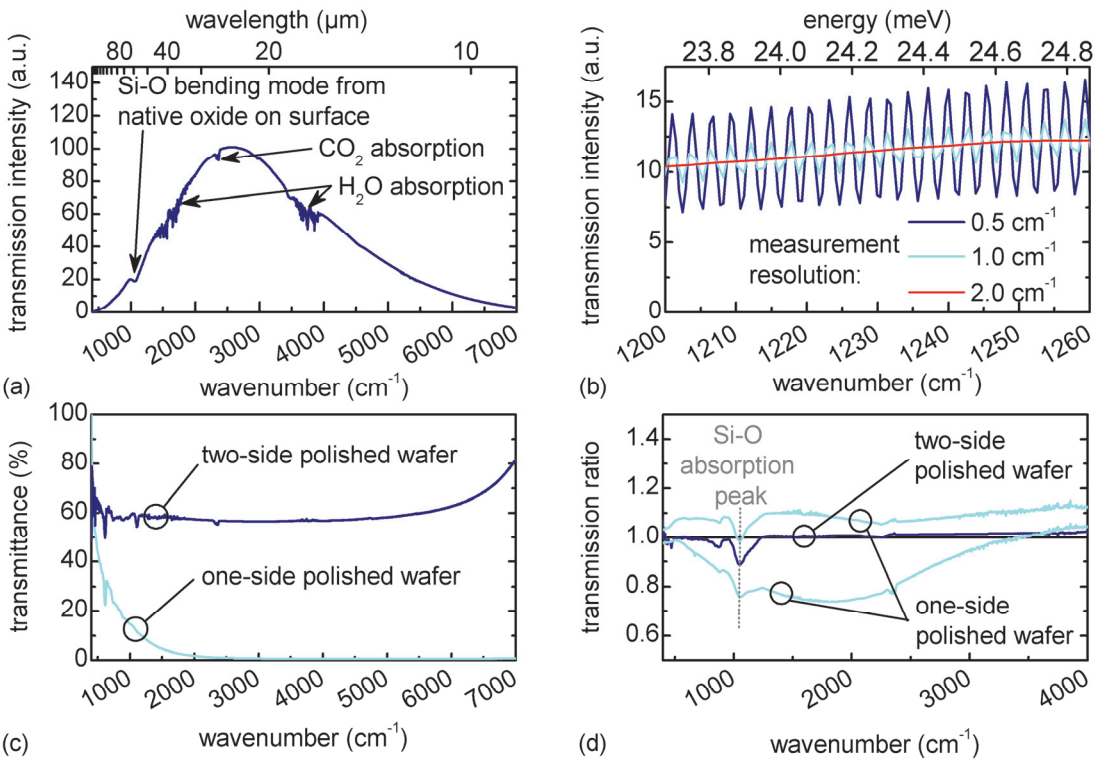

Figure 2-2: (a) Measured light beam intensity as a function of wavenumber (energy unit) of halogen lamp after transmission through a silicon wafer. On the top-axis, the inverse proportionality of wavenumbers to wavelengths is illustrated. (b) A zoom on transmission intensity measurements acquired with different resolutions. On the top-axis the proportionality of wavenumbers to conventional energy units is illustrated. (c) Transmittance of wafer samples. (d) Transmission ratio of wafer/SiO_x to reference wafer samples showing the absorption peak of the Si-O stretching mode at 1050 cm^{-1}.

wavenumber (decreasing wavelength) due to increasing scattering of light at the rough silicon/air interface. In order to quantify the Si-O stretching mode absorption at 1050 cm^{-1}, the transmission of SiO_x/wafer stacks are measured and normalized to that of a reference wafer piece, cut from the same wafer. The absorption peak is shown for three different SiO_x layers in Figure 2-2 (d), one on a two-side polished wafer and two on one-side polished wafers. The height of the absorption peak depends on the oxygen content in the SiO_x layer and the thickness of the layer. For the transmission ratio, unity should be obtained for wavenumbers where no absorption takes place, as shown by the sample on a two-side polished wafer. We think that the non-flat ("wavy") background of the transmission ratio of one-side polished wafers stems from non-uniform roughness on the unpolished side of the one-side polished wafers. Such non-uniformity is also suggested by the non-uniform reflection of light at the unpolished side visible by eye. This non-uniformity can change the wavelength dependent transmission of light as illustrated in (c), from one piece to the next, and is responsible for a large variety of background-curvatures observed on such wafers. As the wavy background contribution has a much larger scale than the absorption peak for Si-O stretching modes, it is still possible to extract useful information about absorption intensity by a careful manual correction of the wavy background.

2.2.4 Angular resolved scattering (ARS)

ARS in transmission is measured with a setup built at IMT. A green laser beam (543 nm) with normal incidence on the glass/ZnO samples is scattered at the rough ZnO/air interface and the transmitted light intensity is measured by a photodetector mounted on a 115 mm long, motorized, goniometric arm. The photodetector is moved in a plane comprising the incident beam in a circular manner around the point where the laser beam is scattered. The detector scans the light intensity for polar angles (θ) from 0° (direct transmission of laser beam without scattering) to 90° with an angular resolution of 1.44°. The light intensity is measured with a lock-in detection technique. The random textures used in this work are much smaller than the diameter of the laser beam and we therefore assume isotropic scattering for all azimuthal angles. The total light intensity scattered with an angle θ is obtained by multiplying the ARS(θ) measurements by sin(θ). In order to compare intensity measurements performed on different days, with possibly different laser intensities, we normalize ARS(θ)·sin(θ), so that its integral from 0° to 90° equals the haze measured for the same wavelength (see Figure 3-2 for examples).

2.2.5 Conductivity

To measure in-plane conductivity of SiO_x thin films, two 8 mm wide aluminum contacts separated by 1 mm are evaporated onto the samples. The contacts are annealed for 90' at 180 °C in vacuum, and the current between the two contacts is measured with an electrometer at a constant voltage of 7 V as a function of temperature from 180 °C to 25 °C. The good sensitivity of this setup allows one to measure conductivities between 100 and 10^{-10} S/cm. For samples with anisotropic conductivity, the in-plane conductivity has to be distinguished from the transverse (out-of-plane) conductivity. The transverse conductivity of SiO_x layers is extracted from current-voltage (*I-V*) characteristics measured with the *I-V* setup (section

2.5.1). To measure the transverse conductivity of SiO_x films, the following layer-stack with a surface area of 0.25 cm^2, similar to solar cells, is fabricated: ZnO, n-type µc-Si (20 nm), n-type SiO_x (100 nm), n-type µc-Si (20 nm), and ZnO. On the one hand, the resistivity of the ZnO layers in this configuration gives an upper limit for the measureable transverse conductivities of 10^{-5} S/cm and on the other hand, transverse conductivities below 10^{-7} S/cm cannot be measured due to the limited sensitivity of the *I-V* setup. With this narrow range, it is not possible to quantify the transverse conductivity for a large variety of SiO_x layers, but this method can be used as indicator to test if the transverse conductivity of the SiO_x layer is above 10^{-5} S/cm or not. This is sufficient to determine if a 100 nm thick layer is suitable for use in thin-film silicon solar cells because it corresponds to an increase in series resistance of 1 Ω·cm^2, above which the fill factor of the solar cell is negatively affected.

2.2.6 Raman crystalline fraction

For a Raman crystalline fraction measurement, the sample is illuminated with an argon laser beam (514 nm). The light interacts with phonons (molecular vibrations) leading to a small frequency shift (Raman effect) for scattered light, which is slightly larger for µc-Si than for a-Si. The spectral distribution of the backscattered light is analyzed with a monochromator and then fitted with three Gaussian distributions centered at 480 cm^{-1} for a-Si, at 510 cm^{-1} for nanocrystalline silicon, and at 520 cm^{-1} for crystalline silicon (c-Si). The Raman crystalline fraction of the silicon phase is calculated as $R_c = (I_{510}+I_{520})/(I_{480}+I_{510}+I_{520})$, where *I* represents the area under the respective Gaussian distributions.[79] In mixed-phase SiO_x layers, there is a phase separation into silicon-rich and oxygen-rich material. The Raman measurement as described above takes into account only the silicon-rich phase and there is no response from the silicon oxide phase for these wavenumbers. Therefore for oxygen-rich SiO_x layers, the Raman signal becomes small since the oxygen-rich phase makes up the majority of the volume. The Raman crystalline fraction for such samples does not represent a crystalline volume fraction, but quantifies the crystallinity of the silicon-rich phase only.

2.2.7 Atomic force microscopy (AFM)

AFM is performed with a Digital Instrument type DI 3100, at CSEM, Neuchâtel, by P. Cuony or M. Leboeuf, from CSEM. Silicon tips, type Tap 150G from Budget Sensors, are used to scan 10 µm x 10 µm images with 512 x 512 data points, acquired at scanning speeds of 5–10 µm/s. The images are flattened with WSxM[80] and the root-mean-square (RMS) roughness, peak-to-peak (p-p) value, and the ironed surface (also called developed area) are calculated with the same free software. The inclination angle for each data point in the AFM-matrix is calculated by the following MATLAB code written by Julien Bailat, making use of the "gradient()" function:

```
[fx,fy]=gradient(AFM-matrix,Δx,Δy);

Angle-matrix=180/pi*acos(1./(1+fx.^2+fy.^2).^.5);
```

2.2.9 Energy filtered transmission electron microscopy (EFTEM)

Electron energy loss spectroscopy (EELS) analysis and energy-filtered imaging are performed using a JEOL 2200FS microscope equipped with an Ω-filter. Energy-loss spectra are all taken in image mode from regions 275 nm in diameter chosen with a selected area aperture. Energy-filtered images are taken using an objective aperture to limit the collection semi-angle to 11 mrad. By taking images with a 4 eV wide slit centered on 10, 17.5, and 23 eV energy losses, the intensity contribution underlying the sharp silicon plasmon peak from the broad SiO_2-type peak can be subtracted effectively, in the manner suggested for scanning TEM-EELS experiments by Schamm *et al.*[81] Statistically determined spatial drift correction is used to align each set of three images.[82] The EELS-EFTEM analyses are performed by D. Alexander at CIME, EPFL. Plan-view samples are prepared by P. Cuony using an acid-etch to dissolve ZnO layers underlying the SiO_x thin films, and catching the floating pieces on standard TEM grids (see Figure 2-3). Cross-section specimens are prepared by Danièle Laub and Colette Vallotton at CIME, EPFL, with tripod-polishing and ion beam milling of thin-film sandwiches of c-Si/μc-Si/SiO_x stacks.

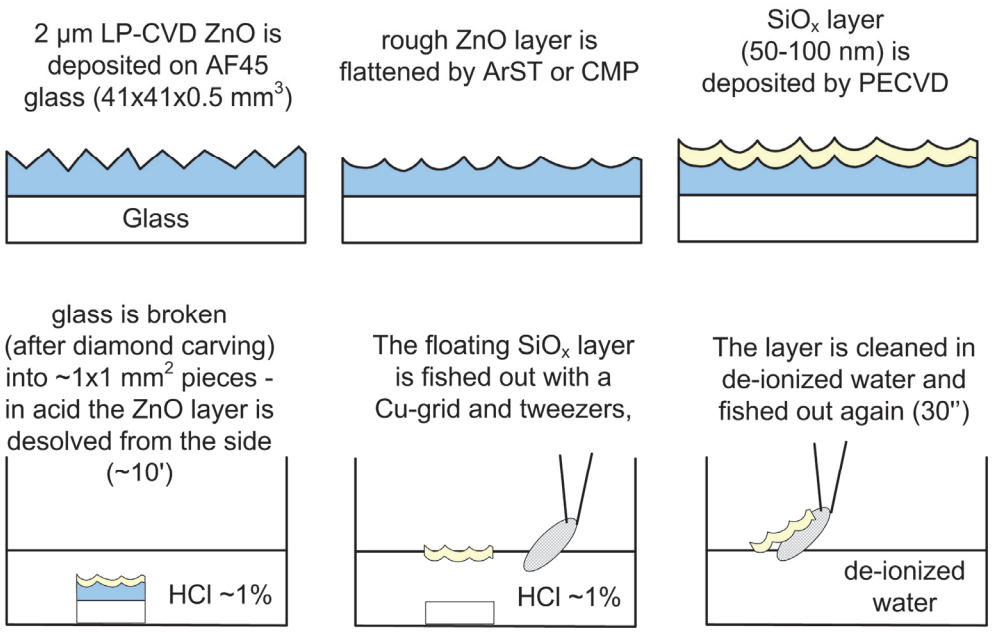

Figure 2-3: Illustration of preparation method for freestanding SiO_x layers on TEM grids for plan-view EFTEM analysis.

2.4 Cell fabrication process

The cells presented in this work are fabricated by the following steps: glass cleaning, ZnO deposition, argon surface treatment of front ZnO, silicon layer deposition, drawing of negative cell pattern with permanent marker, back ZnO deposition, dissolving of permanent marker in acetone (lifting off the back ZnO on the marked regions), and sulfur hexafluoride (SF_6) plasma etching of the exposed silicon (the ZnO and the silicon layers below the remaining back ZnO are not attacked by the SF_6). This gives the final structure of the device with a continuous ZnO front electrode on the glass substrate and isolated cells defined by the silicon and back ZnO layers. The Micromorph cells presented in this thesis are all patterned to 1.2 cm^2 and a-Si and µc-Si single junction cells are patterned to 0.25 cm^2. At this moment, the *I-V* curves of the cells are measured a first time (initial state). Then the cells are annealed in a nitrogen (N_2) purged oven at 180°C for 90 minutes and the *I-V* curves are measured a second time (annealed state) followed by external quantum efficiency (EQE) measurements. Afterwards the cells are either light soaked (LS) for 1000 h with 1000 W/m^2 irradiation at 50 °C, or kept in plastic boxes stored on a bookshelf in the office.

2.5 Cell characterization

2.5.1 Current-voltage (*I-V*) characteristics

For the *I-V* measurement, the cells are illuminated with a steady-state dual-beam solar simulator from Wacom with a light intensity of ~1000 W/cm^2 and a spectrum similar to AM1.5g. The room temperature during the measurement is kept between 20 °C and 26 °C and a small ventilator reduces the heating of the cell during the short light exposure. The *I-V* curves are acquired by a Keithley 2700 source-meter that performs a four-probe voltage sweep with a 10 mV interval on each cell, and the open-circuit voltage (V_{oc}), short-circuit current (I_{sc}), and fill factor (*FF*) are extracted. To improve the correctness of the *FF* of Micromorph cells, a white dielectric reflector is applied to the back of the cell to ensure correct current matching and a steel mask with openings of 1.06 cm^2 is put on the front of the glass to avoid lateral collection of light. The short-circuit current density (J_{sc}) is calculated from the EQE measurement and not extracted from the *I-V* curves.

2.5.2 External quantum efficiency (EQE)

The EQE gives the probability that a photon generates an electron-hole pair that contributes to the solar cell current in short-circuit conditions. In the setup built at IMT, light from a xenon lamp is chopped at 230 Hz, and the wavelengths are scanned with a monochromator. After a beam splitter, one part of the monochromatic light illuminates 1 mm^2 of the solar cell and another part illuminates a reference detector. The currents of the reference detector and the solar cell are measured with a lock-in technique and by comparing the measurements with a certified reference cell, the EQE is calculated. The J_{sc} of the solar cells is determined by integrating the product of the EQE and the incoming photon flux of the AM1.5g spectrum. For Micromorph cells, the cell current is given by the limiting sub-cell and the EQE has to be measured in two steps. First, the bottom cell is illuminated with continuous infrared light (halogen lamp with KG830 filter), and the measured EQE is the response from the current-limiting top cell only. Second, the bottom cell EQE is measured, by saturating the top cell with blue light (halogen lamp with KG1+BG23 filters). By adding the EQE of the two sub-cells, a summed EQE can be calculated, which represents the useful absorption in a Micromorph cell.

2.6 Chemical mechanical polishing (CMP) system

We designed and built a CMP system capable of homogenously flattening rough morphologies on 40 x 80 mm^2 substrates. This was motivated by the following three different uses of the CMP system: First, to flatten the surface of the intermediate reflecting layer (section 0) in order to separate the growth morphologies of the a-Si and the µc-Si cells in the Micromorph configuration. Second, to decouple the conductivity and pyramid size of the front electrode by making bi-layers with a polished bulk ZnO layer for electrical conduction and a resistive rough layer with varying pyramid size.[17] And third, for testing flat back reflectors in rough cell configurations (section 8.1).

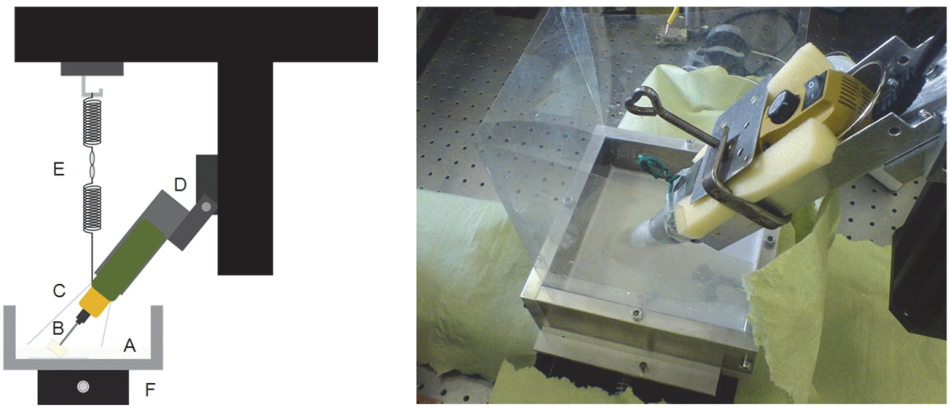

Figure 2-4: Schematic and photograph of the CMP system designed and built by P. Cuony and S. Hänni.

With a budget of 1000 SFr and the help of Simon Hänni during his civil service, we built the system illustrated in Figure 2-4. The substrate is fixed in an aluminum container (A), which is filled with 5 mm of colloidal silica, a suspension of 40 nm spherical silica particles in aqueous solution (Struers, OP-S). A circular felt disc (B) 1.8 cm in diameter (Bergeon no. 2686-161) is rotated by a micro-drill (Proxxon) at 5000 rpm and polishes the substrate with the silica particles. A plastic cylinder, taped onto the micro-drill, prevents sprinkling of the colloidal silica out of the container. The micro-drill is fixed on a rotating arm (D) and presses the felt with its weight onto the substrate. This force can be lowered with springs (E) or increased by adding weight to the drill. The container with the substrate is mounted on an x-y table, moving the substrate under the polishing head in order to scan the desired surface homogenously. The stepper motors on both axes are controlled with a Labview program developed for this application with the help of A. Lo.

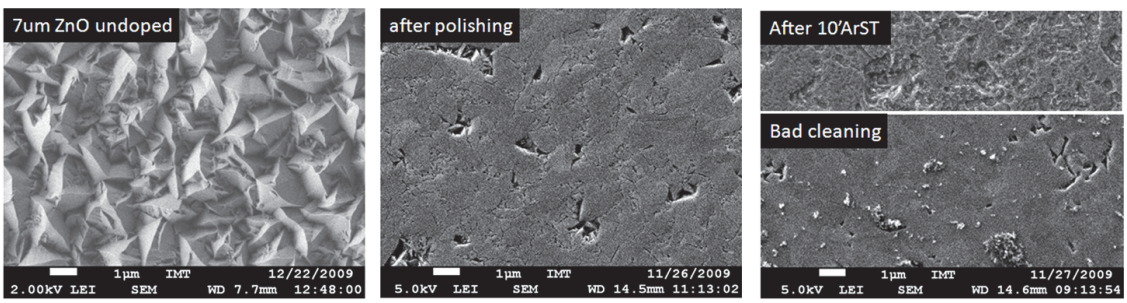

Figure 2-5: SEM images of as-grown rough Z7 (left), and Z7 after CMP polishing (middle) with the lowest valleys still visible. If not cleaned properly, silica particles can be left on the surface (right-bottom). The grain boundaries and remaining valleys can be smoothened by an ArST (right-top).

Figure 2-5 shows scanning electron microscope (SEM) images of Z7 (the roughest ZnO layers used in this work) before and after CMP polishing. The deepest valleys are still visible after this polishing step, but can be removed by making slower CMP scans or by polishing the sample a second time. The remaining holes and visible ZnO grain boundaries can be smoothened out with an ArST. After the CMP process, the sample is cleaned with a paper towel under flowing water to remove remaining silica particles on the surface.

3 Rough ZnO front electrodes

Boron-doped ZnO, deposited by low pressure chemical vapor deposition (LP-CVD) from diethylzinc ($(C_2H_5)_2Zn$), water vapor (H_2O), and diborane (B_2H_6) precursors, has excellent opto-electrical properties for use as front electrodes and has led to record thin-film silicon solar cell currents and efficiencies.[10,19,22,57] The goal of this chapter is to give an overview of the ZnO morphologies used in our research lab. In section 3.1 we present the pyramidal morphology and optical properties of as-grown rough ZnO and in section 3.2 and 3.3 we show how a post-deposition argon plasma treatment or subsequent a-Si layer deposition can alter this surface morphology. In section 3.4 we quantify the undesired reflection at the ZnO/a-Si interface, and in section 3.5 we point out the important morphology parameters that determine the optical suitability of a front electrode for use in thin-film silicon solar cells. The overview of the large variety of surface morphologies in this chapter is necessary to understand the substrate dependency of nearly all the results presented in subsequent chapters.

The results shown in this chapter are not published elsewhere.

3.1 As-grown rough ZnO

Figure 3-1 shows the surface morphology of LP-CVD ZnO without boron doping and the evolution of the ZnO pyramid sizes with increasing layer thicknesses from 1 µm to 7 µm. The capability of rough surfaces to scatter light can be expressed by their haze, the ratio of diffuse to total transmitted light intensity. The measured haze of the air/glass/ZnO/air system is shown in Figure 3-2. The spectral range of interest for silicon solar cells is 400–1000 nm in air, corresponding approximately to effective wavelengths of 200–500 nm in ZnO and 100–250 nm in silicon. As the typical feature sizes of Z1 are smaller than 100 nm, the light wave at the

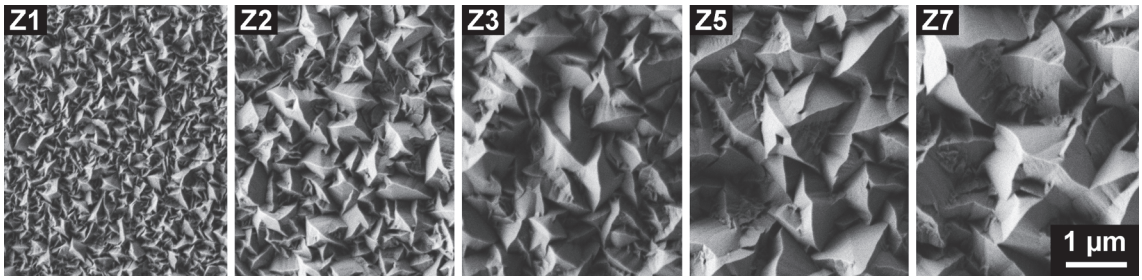

Figure 3-1: SEM images showing the as-grown rough surface morphology of 1 µm (Z1) to 7 µm (Z7) thick ZnO layers. (SEM by M. Boccard)

ZnO/Si interface sees an average of several pyramids ("does not clearly see the roughness of the interface" due to the effective medium approximation effect leading to an index grading)[83] and passes straight into the silicon layer without being scattered. Larger faces on bigger pyramids are more likely to scatter light, leading to increasing haze until it saturates at 100%. Scattering at the ZnO/Si interface cannot be measured directly due to the absorption in silicon, but from the measurements of air/glass/ZnO/air systems, one can approximate scattering into silicon by multiplying the wavelength by two, as proposed by Dominé et al.[17,84] due to a refractive index contrast which is twice as big. This means that the haze measured at 400-nm-wavelength-in-air corresponds approximately to the haze that light with 800-nm-wavelength-in-air will experience in silicon. For large wavelengths, the haze continuously increases with increasing pyramid size, but for the spectral range of interest with wavelengths <1100 nm in air, the haze in silicon saturates at 100% for all layers from Z3 to Z7. With respect to haze, no optical advantages of feature sizes above those of Z3 should thus be expected.

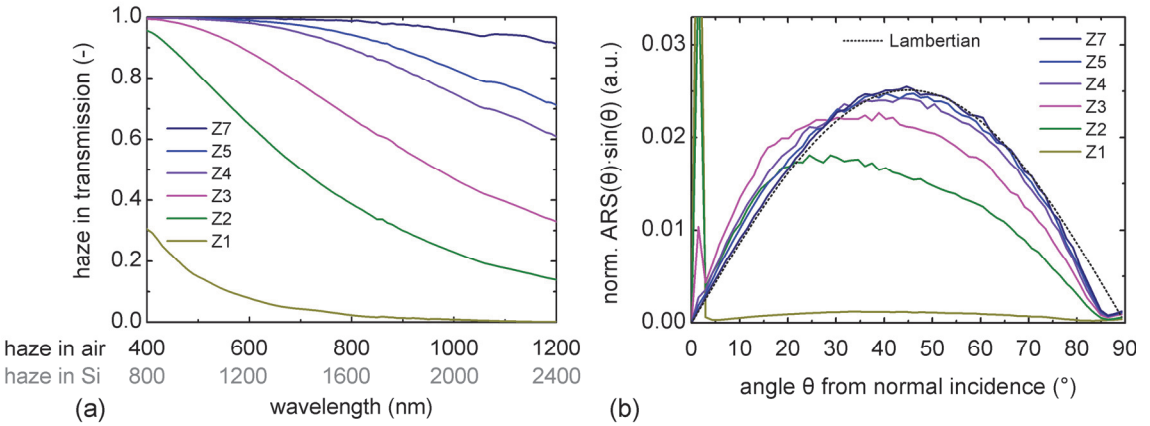

Figure 3-2: (a) Haze in transmission as a function of wavelength of glass/ZnO stacks with 1–7 µm thick non-intentionally doped ZnO layers. (b) Total transmitted light intensity as a function of scattering angle. The dotted line shows the Lambertian scattering: $ARS_{Lamb} = \cos(\theta)$.

Another important factor for thin-film silicon solar cells is the angular distribution of the scattered light intensity, here represented by the product of the measured angular resolved scattering (ARS) with sin(θ). For better comparability, the area under the light intensity curve is normalized with the measured haze for the same wavelength. The higher the scattering angle θ, the longer the light path in the silicon layer, and since the silicon absorber layers are sandwiched between two ZnO layers with lower refractive indices, there is a higher probability for light trapping. The as-grown rough ZnO layers with thicknesses >3 µm show almost Lambertian scattering in air, but the angular scattering into silicon will be narrower because in the case of the ZnO/Si interface, the light passes into a material with a higher refractive index, whereas at the measured ZnO/air interface, the light is transmitted into air, which has a refractive index lower than ZnO.[84]

3.2 Argon surface treatment of rough ZnO

In this section we first present the effects of a post-deposition argon plasma surface treatment (ArST) on the morphology and optical properties of ZnO layers and then identify the roughness values that best describe these morphology changes.

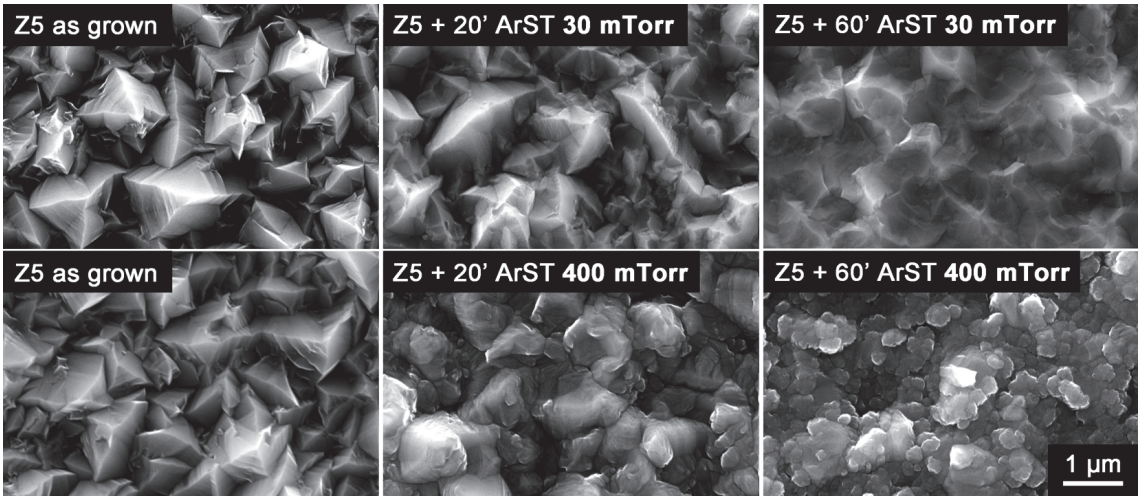

Figure 3-3: SEM images of 5 µm thick ZnO as grown and after argon surface treatments (ArST) at process pressures of 30 and 400 mTorr, producing U-shaped and cauliflower-like morphologies, respectively. (SEM by S. Faÿ)

Figure 3-3 illustrates the smoothening effect of Ar^+ ions hitting the surface of the ZnO film with two different process pressures. In the reactive ion etching system used for these experiments, the RF electrode builds up a DC self-bias of -600 V at 30 mTorr, meaning that Ar^+ ions from the plasma hit the ZnO sample, placed on the RF electrode, with 600 eV if they do not collide with other particles on their way to the ZnO sample. At 400 mTorr, the DC bias of the RF electrode is reduced to -300 V, meaning that for the same applied RF power (~1 W/cm^2), more Ar^+ ions bombard the ZnO layer, but with lower energy. As the typical binding energy of the Zn-O bond is ~0.5 eV,[85] it can be speculated that for both pressures similar etching processes are taking place, sputtering off several Zn, O, or Zn_xO_y particles for each Ar^+ ion hitting the ZnO surface. At 400 mTorr, the residence time of all species in the chamber is longer, increasing the chance for Zn_xO_y to re-deposit on the film surface before being pumped out of the chamber. A competition between Zn_xO_y etching and re-deposition thus influences the resulting surface morphology, and it is speculated that the cauliflower-like morphology at high pressure stems from increased Zn_xO_y re-deposition compared to the low-pressure process where etching dominates.

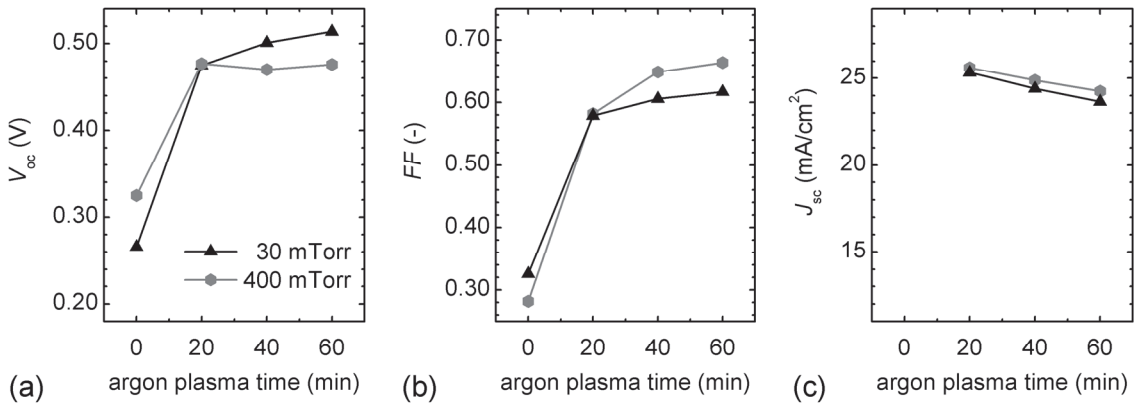

Figure 3-4: µc-Si cell parameters as a function of ArST time of the Z5 front electrode.

µc-Si cells are strongly shunted if deposited on as-grown rough Z5 and no reasonable short-circuit current densities (J_{sc}) can be measured with the external quantum efficiency setup working at low device illumination. Bailat et al.[67] found that µc-Si cell parameters can be significantly improved when the morphology of as-grown rough ZnO is smoothened by a plasma surface treatment. Python et al. [64-66] identified that the improved open-circuit voltage (V_{oc}) and fill factor (*FF*) of µc-Si cells are caused by a reduction of the number of cracks in the µc-Si absorber layers due to less constraint during layer growth. Figure 3-4 confirms this trend for low-pressure ArST with the morphologies changing from V- to U-shaped, but it also shows the same trend for the high-pressure ArST when morphologies change from V-shaped to cauliflower-like. The exact requirements for front electrode morphologies to avoid the formation of cracks in µc-Si are not yet known and are a subject for further studies. In order to better understand the front electrode morphology and its influence on thin-film silicon solar cells, we quantify here the optical properties and morphological parameters of the Z1–Z7 series after different ArST times. Nevertheless, these investigations, as well as all the other ArST in this thesis report, are performed at low argon pressures only and different plasma surface treatments may lead to different results.

The ArST leads to a smoothening of the as-grown rough ZnO layers and Figure 3-5 (a) and (b) show how the haze is affected by this change in surface morphology. Figure 3-5 (c) and (d) show that the scattering changes from initially almost Lambertian scattering with maximum light intensity scattered at 45° to less favorable scattering into lower angles. To quantify the morphology changes of the ZnO surface with ArST, we performed AFM measurements on the Z1–Z7 series as-grown and after 5', 20', and 60' ArST. Figure 3-6 shows the surface morphologies of as-grown Z1–Z7 and the same layers after 60' ArST. On Z1 the 60' ArST etched the ZnO almost completely away, and the underlying glass substrate appears as flat circles. From this observation, we can calculate an etching rate of ~ 15 nm/min at 30 mTorr, 1 W/cm^2 input power density, and -600 V electrode bias.

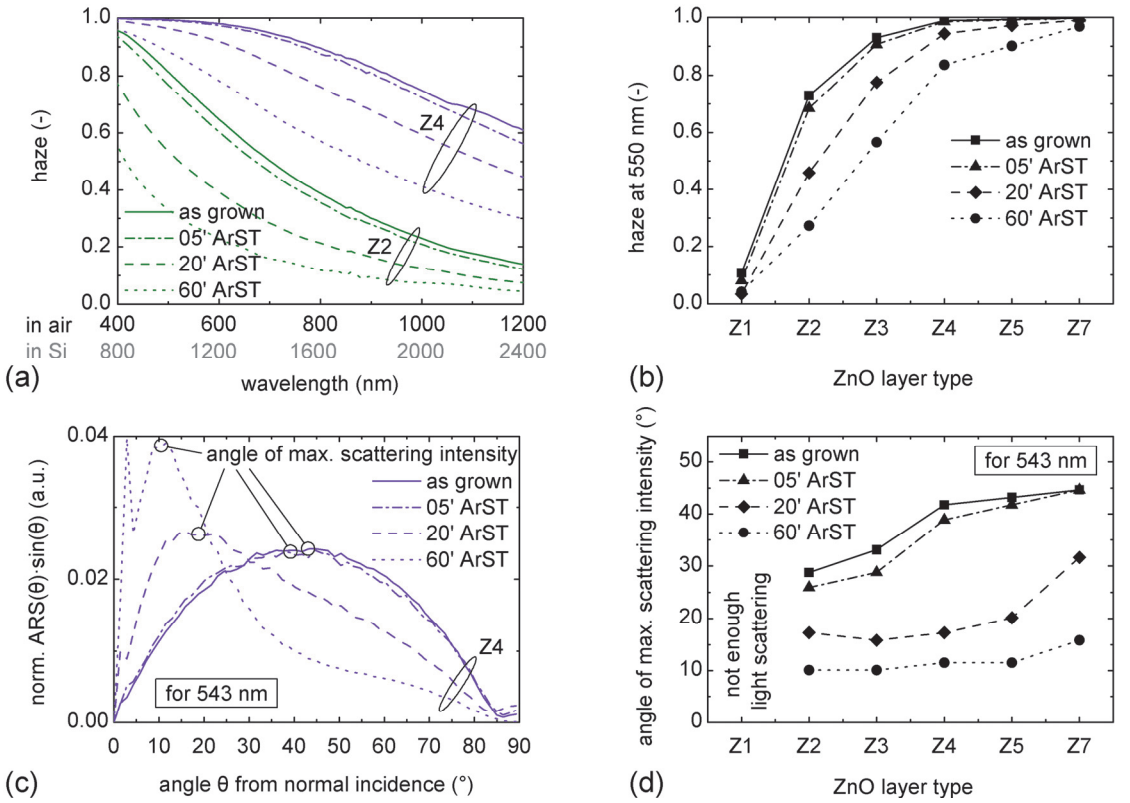

Figure 3-5: (a)-(b) Haze for different ZnO layers and ArST times at 30 mTorr. (c)-(d) Angular dependence of scattered light intensity for different ZnO morphologies and ArST times.

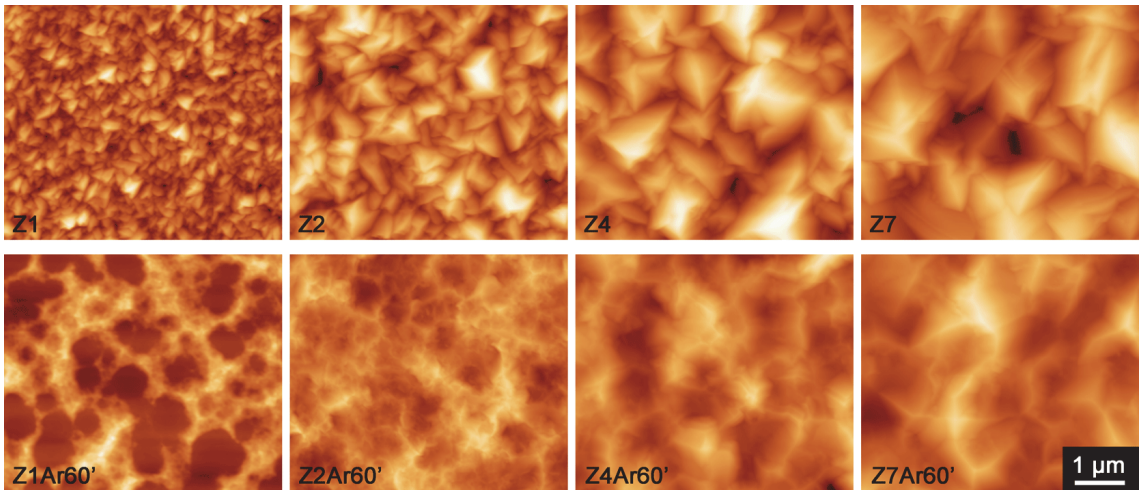

Figure 3-6: AFM images of Z1, Z2, Z4, and Z7, as grown and after 60' ArST.

The RMS roughness or p-p values are quantities that are commonly used to compare surface morphologies with randomly distributed features. Both quantities are shown in Figure 3-7 for the Z1–Z7 series and show the same continuous increase with ZnO layer thickness, but these values are only slightly lowered by the ArST. The problem with both quantities is that they are based on the height of the measured features but not on their form. Therefore, they indicate, for example, a greater roughness for the Z7-Ar60' compared to the Z2. This is in contradiction with ARS measurements shown in Figure 3-5 (d) indicating a lower "optical roughness" for Z7-Ar60'. Similarly, the electrical properties of µc-Si cells are better on Z7-Ar60' than on Z2 indicating a lower "silicon layer roughness" of Z7-Ar60'. To compare our different ZnO layers, the common roughness quantities are therefore not appropriate.

For thin-film silicon solar cells, a more pertinent description of the surface morphology is given by the histogram of inclination angles of the surface (section 2.2.7) or its integral, both shown in Figure 3-9 for the Z1–Z7 series after 20' ArST. From the integral of the angle histogram, one can extract a median inclination angle of the surface (α_{50}) or a 90th percentile (α_{90}). These values are given for all the samples of this series in Figure 3-8.

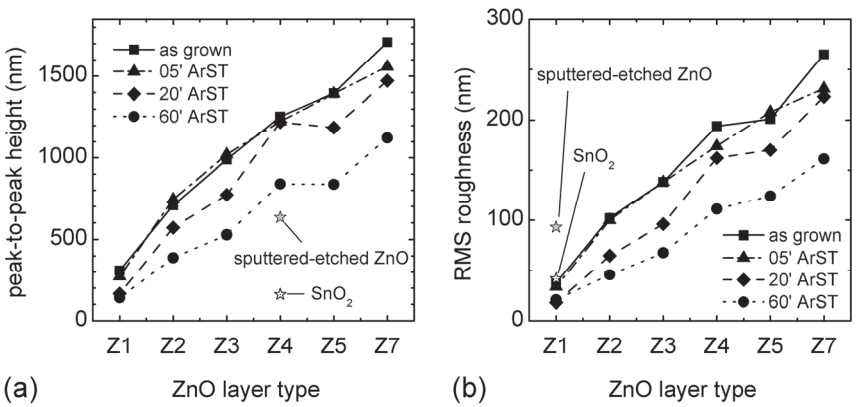

Figure 3-7: (a) p-p values and (b) RMS roughness values for different ZnO layers. Typical values for as-grown rough SnO_2 and sputtered-etched ZnO are shown are shown for comparison.

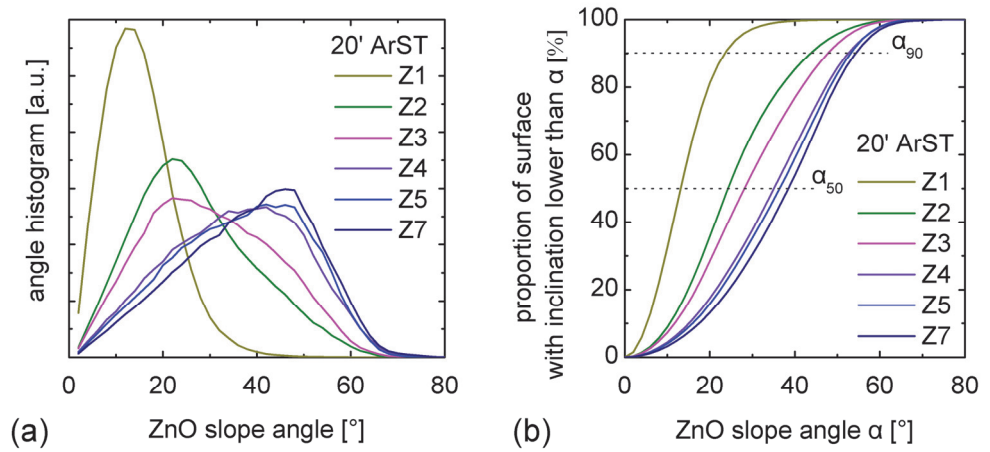

Figure 3-9: (a) Angle histogram of ZnO layers after 20' ArST. (b) Integrated and normalized angle histogram giving the proportion of surfaces with inclination lower to a given angle α. The crossing of the curves with the dotted lines indicates the median angles (α_{50}) and the 90th percentiles of inclination angles (α_{90}) for the different ZnO types.

The α_{50} value gives a description of the surface roughness that seems more pertinent than the commonly used roughness quantities for thin-film silicon solar cells. For example, it shows a big difference between as-grown Z1 and Z2, but saturates for thicker ZnO layers as observed in optical measurements (haze and ARS). It also shows a significant impact of the ArST as can be observed by the ARS measurements. The largest cracks in thin-film silicon solar cells occur in the valleys with the steepest slopes, and it can therefore be speculated that α_{90}, which describes the 10% steepest slopes, is especially adapted to quantify the suitability of a substrate with respect to the electrical properties of µc-Si cells deposited on such substrates. Different experimental unpublished observations seem to confirm the trends predicted by the α_{90} value: µc-Si cells are shunted on as-grown rough Z2–Z7; increasing surface treatment improves µc-Si cell properties; and Z1-Ar5', Z2-Ar20', and Z7-Ar60' will lead to similar µc-Si cell electrical characteristics.

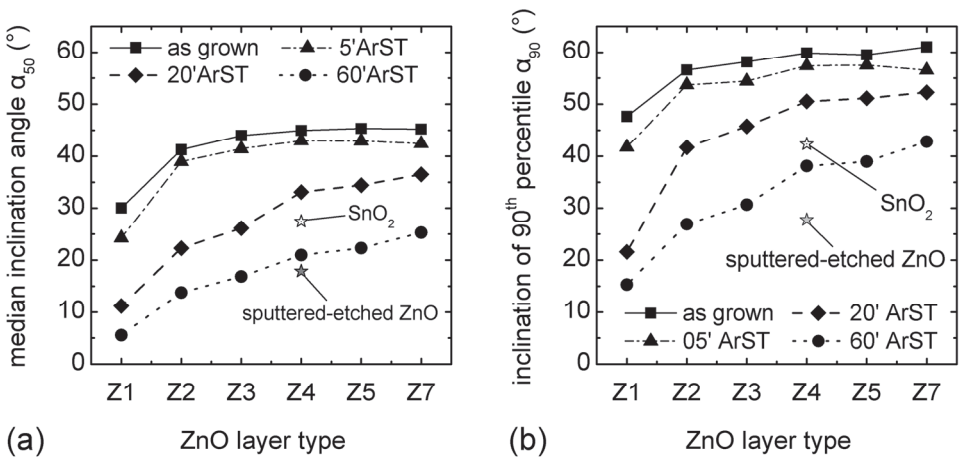

Figure 3-8: Median inclination angle (α_{50}) and 90th percentile of inclination angles (α_{90}) for different ZnO layer types and their evolution with ArST.

In summary, we showed in this section that ArST can smoothen the ZnO surface, and that the resulting morphology depends strongly on the process pressure and time used for the plasma surface treatment. We quantified the influence of ArST on the light-scattering capability of the ZnO films, and we identified the inclination of the surface features as a more pertinent roughness quantity compared to the standard roughness quantities.

3.3 Morphology evolution after silicon deposition

In the Micromorph configuration, the µc-Si cell, which is sensitive to substrate morphology, does not directly grow on the ZnO front electrode, but grows on the a-Si cell or the intermediate reflecting layer, if present. We therefore examine here how the substrate morphology of the front electrode is altered by the deposition of a 300 nm thick a-Si layer. Figure 3-10 shows the surface morphologies of ZnO layers that were subject to 20' ArST, before and after the deposition of 300 nm a-Si.

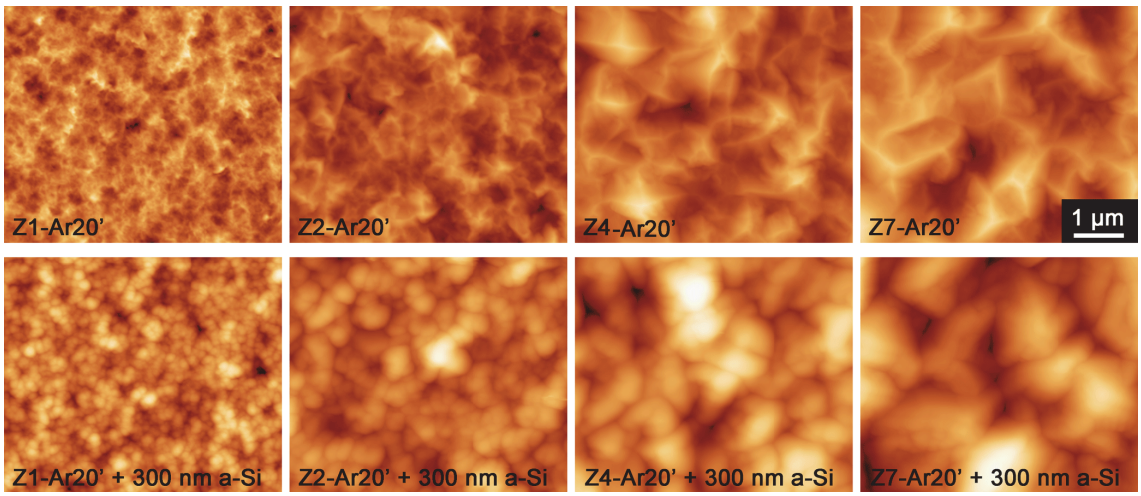

Figure 3-10: AFM images of Z1, Z2, Z4, and Z7, after 20' ArST and 300 nm a-Si deposition.

The morphology changes can be clearly identified by eye: the deposition of the a-Si layer leads to a rounding of the pyramidal peaks and ridges and a sharpening of the valleys. These morphology changes are illustrated in Figure 3-11 and can be described as U-shaped and ∩-(inverse-U)-shaped, before and after the deposition of the a-Si layer, respectively. These surface morphology changes lead to significantly sharper valleys which can cause the formation of cracks during the deposition of the µc-Si cells, as illustrated in Figure 3-11.

To quantify these observations about morphology changes, we can look at roughness parameters extracted from AFM measurements. Here again, the p-p and RMS roughness shown in Figure 3-12 (a) do not give the pertinent information and show no difference for these samples before and after a-Si deposition. Using the angular approach, it is possible to statistically distinguish the morphology changes by comparing the median inclination angles of

the lower half of the surface (valleys) with the ones from the upper half of the surface (pyramid ridges and peaks). For the Z1–Z7 after 20' ArST Figure 3-12 (b) shows higher angles around the peaks than in the valleys, confirming the U-shaped morphology of these surfaces. After the a-Si deposition the peak regions are significantly flattened, whereas the valleys show slightly higher inclination angles, indicating a V-shaped or inverse-U-shaped morphology.

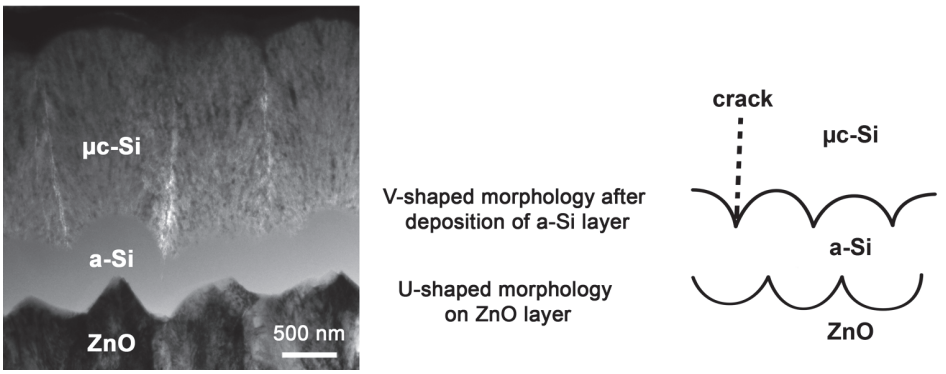

Figure 3-11: TEM cross section of a Micromorph cell showing the change in surface morphology from U-shaped on the ZnO to ∩-shaped after the deposition of the a-Si layer and a schematic illustrating these morphology changes (TEM by M. Python).

In summary, the deposition of an a-Si layer with a thickness similar to the feature size of the ZnO substrate is not completely conformal but changes the surface morphology. Special care has therefore to be taken when working with Micromorph cells, where initially "good" U-shaped morphologies can be converted into "bad" ∩-shaped morphologies after the deposition of the a-Si top cell and possibly the intermediate reflecting layer. The acute valleys of the ∩-shaped morphology lead to an increased numbers of cracks in the i-µc-Si layer which deteriorate the electrical properties of the µc-Si cell and so lower the performance of the Micromorph cell. By comparing the inclination angles of the features in the lower half with the ones on the upper half, we showed for the first time a way to quantitatively distinguish U-shaped from ∩-shaped morphologies.

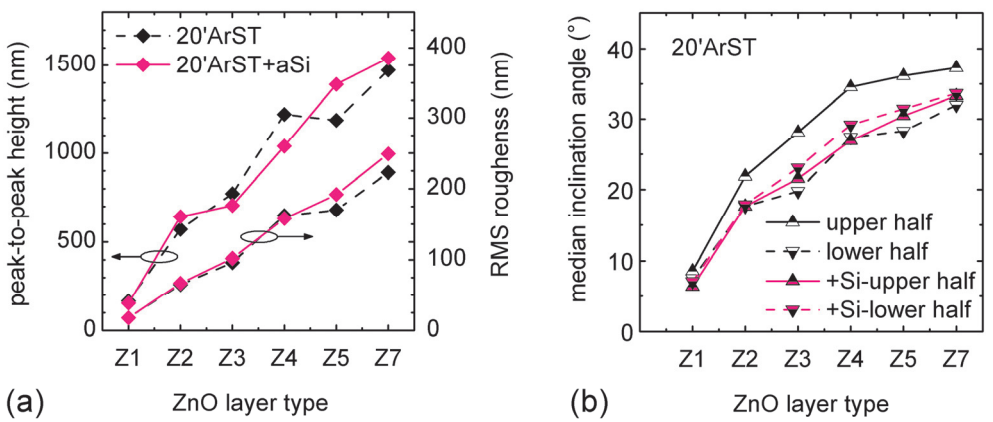

Figure 3-12: Roughness quantities characterizing the morphology difference before and after deposition of 300 nm a-Si layer on Z1-Ar20' through Z7-Ar20'.

3.4 Reflection at the ZnO/a-Si interface

In the previous sections we focused on ZnO morphologies and on transmission and scattering of light from ZnO into silicon. In this section we will show how reflection at the ZnO/Si interface correlates with the ZnO morphology. Taking the refractive index of ZnO (n_{ZnO} at 450 nm = 2.0)[75] and the refractive index of a-Si ($n_{a\text{-}Si}$ at 450 nm = 4.8)[33] a specular reflection of 16% can be calculated from the Fresnel equations for light normally incident on a flat interface.

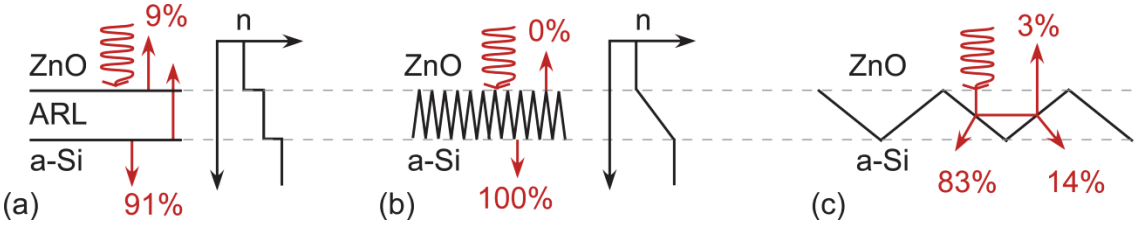

Figure 3-13: Reduction of 16% Fresnel reflection on the ZnO(n=2.0)/a-Si(n=4.8) interface: (a) to 9% with ARL(n=3.1), (b) to 0% with roughness-induced index grading and (c) to 3% with two reflections on 45° inclined interface slopes.

The reflection at the ZnO/a-Si interface can be reduced in three different ways, as illustrated in Figure 3-13: First, the abruptness in the change of refractive index can be reduced by inserting one or several anti-reflection layers (ARL). For a single ARL with an intermediate refractive index of 3.1, the Fresnel reflection can be reduced to 9% from the initial 16% (index matching). This effect will be discussed in the next chapter. Second, the interface can be roughened with surface structures having sizes significantly smaller than the wavelengths of interest. The incident light then "averages" the refractive index over several features and sees an index of refraction that gradually increases over the depth of the roughness (index grading, simulated by effective media approximation).[83] Third, if the interface roughness has features much larger than the wavelengths and if the light after a first reflection encounters the ZnO/a-Si interface a second time (either directly or via reflection at the flat glass/ZnO or air/glass interfaces), then the reflection can be strongly reduced depending on the inclination angles of the features (multiple reflections).[86]

Figure 3-14 (a) shows the reflectance of air/glass/ZnO/a-Si(300nm)/air/reflector systems. A white dielectric sheet is here pressed against the a-Si layer and serves as a back reflector to simulate the conditions in a solar cell. Wavelengths below 450 nm are entirely absorbed in the ZnO and a-Si layers and do not reach the back reflector, and the reflection measurement at 450 nm is thus used to quantify the contribution of the air/glass/ZnO/Si interfaces only. For the flat air/glass and glass/ZnO interfaces, one can calculate the reflectance with the Fresnel equations for normal incidence to be 4% and 2%, respectively. For the as-grown rough Z2–Z7, the measured reflectance curves overlap this calculated minimum reflectance from the flat interfaces. Thus it can be concluded that there is no reflectance at the rough ZnO/Si interface. The reflectance increases at wavelengths above 600 nm because of an increasing contribution of the light reflected at the Si/air/reflector interfaces and starts to decrease after 900 nm due

to increasing free-carrier absorption in the ZnO layers. The reflectance waves on Z1 are due to the interference of specular reflectance at the glass/ZnO and ZnO/Si interfaces.

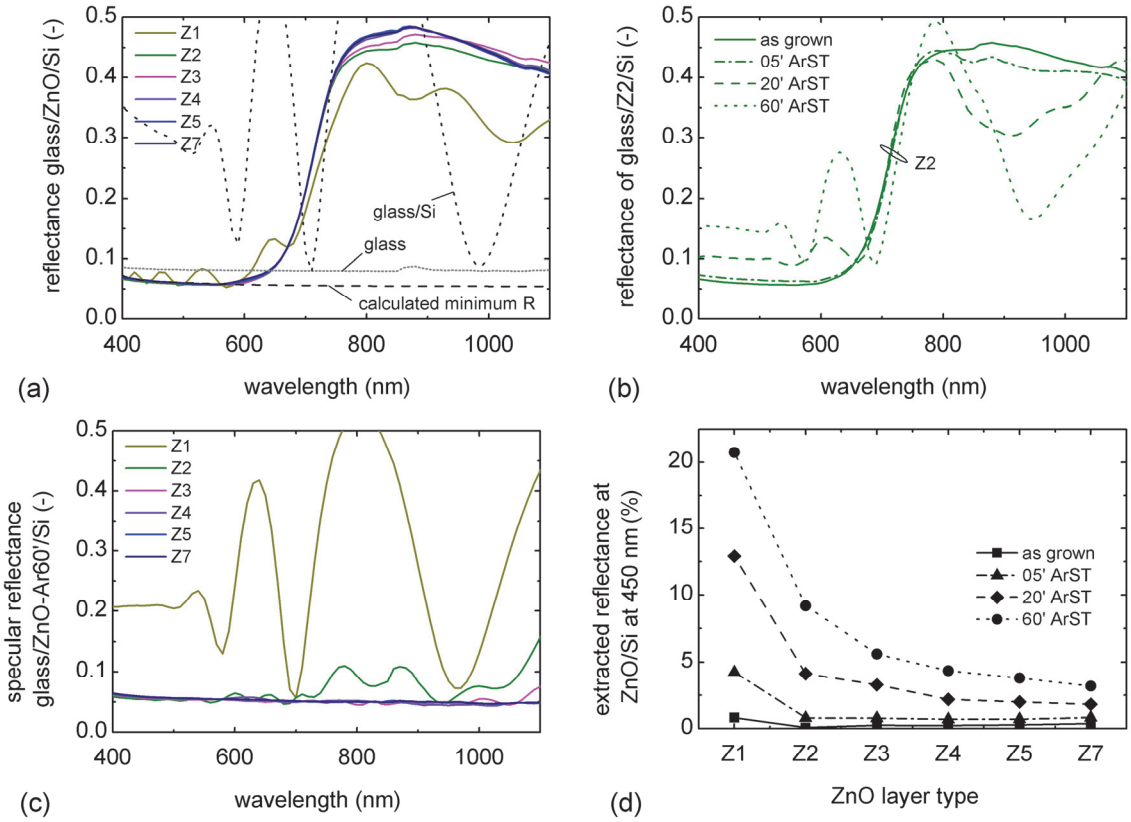

Figure 3-14 (a) Reflectance measurements on glass/ZnO/a-Si stacks. (b) Evolution of reflectance due to ArST of Z2. (c) Specular reflectance of same stacks after 60' ArST of ZnO layer. (d) Extracted reflectance at the ZnO/Si interface. Note that the reflection of the strongly treated Z1 goes beyond 11% because the ZnO layer is partially etched away resulting in a contribution from the glass/Si interface with 21% reflectance.

Figure 3-14 (b) shows how the reflectance increases with ArST on Z2 due to the smoothening of the optical interface. Figure 3-14 (c) shows only the specular part of the reflectance for the Z1–Z7 series after 60' ArST, revealing a completely diffuse reflection for all observed ZnO/Si interfaces, except for Z1. Figure 3-14 (d) summarizes the reflection at the ZnO/Si interface at 450 nm for the entire Z1–Z7 ArST series, obtained by subtracting the ~6% Fresnel reflections of the flat air/glass/ZnO interfaces from the measured values for the entire systems.

As the feature sizes in our case have similar dimensions to the wavelengths of interest, it is not clear how much the canceled reflection at the ZnO/a-Si interface for as-grown rough Z2–Z7 is due to roughness-induced index grading or multiple reflections. The appearance of a completely diffuse reflectance after ArST must be due to a reduction of the "multiple reflections" effect, whereas a reduction of the "roughness-induced index grading" effect would result in specular reflection. As shown in section 3.2, the prime influence of the ArST is to flatten the inclination angles of the surface, which on large features changes the geometric angle of reflection for incident light and so reduces the chance of reflected light to encounter

the ZnO/Si interface a second time. The reduced reflection at the ZnO/Si interface is commonly attributed to index grading, but our observations, in agreement with previous conclusions by D. Dominé in his thesis,[87] strongly suggest that multiple reflections play an important role in reducing the reflection.

In summary, the surface treatment of LP-CVD ZnO front electrodes has undisputed beneficial effects on the electrical performance of µc-Si cells, but the smoothening of the ZnO/Si interface leads not only to reduced light-trapping capability as shown in section 3.2 but also increases reflection losses.

3.5 Optical figure of merit (OFM) and roughness values

In this section we will identify the key roughness values that determine the optical suitability of an electrode for µc-Si solar cells. To do so, we first define an optical figure of merit (OFM), calculated from optical measurements only (see equations 1 and 2) and then look at which roughness values extracted from AFM measurements best describe the trends given by the OFM.

$$OFM = \frac{1}{OFM_{Lambertian}} \cdot \int_3^{90} norm.ARS(\theta) \cdot \sin(\theta) \cdot \theta \cdot \delta\theta \quad (1)$$

$$OFM_{Lambertian} = \int_3^{90} cos(\theta) \cdot \sin(\theta) \cdot \theta \cdot \delta\theta \quad (2)$$

The two measurements that indicate the optical suitability of an electrode for µc-Si solar cells are the haze at ~540 nm and the ARS(θ) as shown in the previous sections. If the ARS measurements are multiplied by sin(θ) and normalized with the haze measured for the same wavelength, one has a good picture of the light-scattering capability of a given morphology. To extract from this function a single value and to include the notion of "the higher the scattering angles the better," we propose to weight the ARS measurement with the scattering angle and then integrate this θ-weighted light intensity over the angles 3°–90°. Lambertian scattering is believed to lead to the maximum light trapping achievable with random textures,[88,89] and if we make the same OFM for Lambertian scattering and use this to normalize the OFM of a given texture, we get a figure of merit for the light absorption enhancement (0 = no light absorption enhancement; 1 = light absorption enhancement by Lambertian scattering) that is similar, but in our opinion simpler, than the merit criterion recently proposed by Rockstuhl et al.[90] The goal of such a figure of merit is to reflect the general tendencies of 540 nm light in air, approximately corresponding to what 1080 nm light experiences in silicon.[17,84] It is clear, however, that no figure of merit, calculated from the front electrode only, can precisely forecast the photo-generated current in a thin-film silicon solar cell, which depends on many other parameters such as back reflector, cell thickness, and material quality.

$$Light\ scattering\ roughness = \alpha_{50} \cdot \min(1, \frac{\sigma}{135}) \quad (3)$$

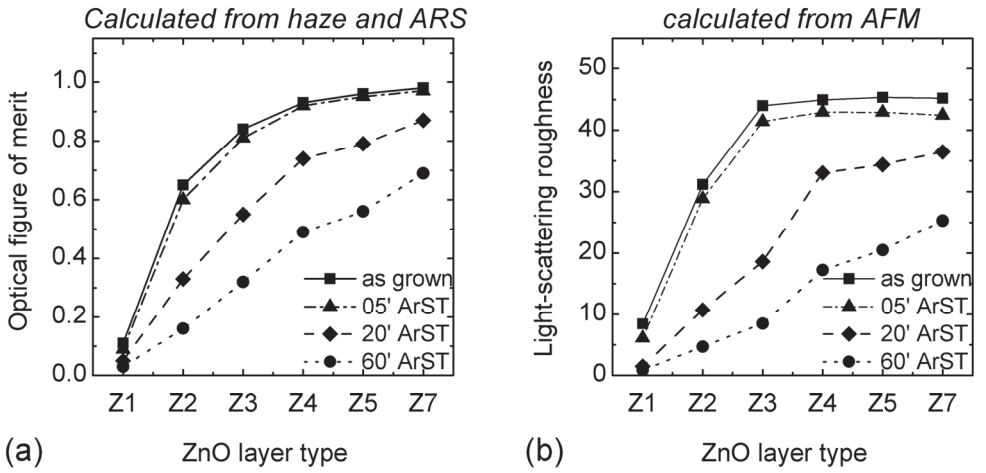

Figure 3-15: (a) Figure of merit for light absorption enhancement calculated from optical measurements. (b) Light scattering roughness calculated from AFM measurements.

Looking at the AFM measurements it is now possible to figure out which roughness values correlate with this OFM. As shown in the previous sections, the median inclination angle of the surface (α_{50}) seems to be a quantity that correlates better with optical measurements than the typical roughness quantities. From haze measurements in Figure 3-2 we conclude that light scattering in silicon increases with increasing pyramid size, but saturates for pyramids that are larger than the wavelengths being measured. We propose to use the RMS roughness value in nm (σ) to statistically quantify the pyramid size, and since we are looking in this section at wavelength of 540 nm in air, we will compare σ to 135 nm, the corresponding wavelength in silicon. To take into account the saturation effect, we will multiply the α_{50} with min(1, σ/135) to get a value for the "light-trapping roughness" entirely deduced from AFM measurements (equation 3). Figure 3-15 compares the OFM with this light-scattering roughness and shows a good correlation between the two parameters for the large variety of surface morphologies used in this chapter.

It is impossible to find a figure of merit with general validity for all thin-film silicon solar cell configurations, but we showed in this section a method to condense the haze and ARS measurements into one OFM value. From AFM measurements we conclude that the median inclination angle of the surface (α_{50}) is nicely correlated with the OFM, but has to be corrected with a feature-size parameter if the ZnO pyramids are too small to completely scatter the incident light.

3.6 Conclusion

With high haze values and quasi-Lambertian scattering, as-grown rough ZnO has excellent optical properties for use as front electrodes in thin-film silicon solar cells. The surface morphology can be smoothened by post-deposition surface treatments to improve the quality of the silicon layers deposited by PECVD and so increase the cell electrical characteristics. Thin-film silicon solar cell development in recent years has mostly turned around this trade-off between electrical and optical characteristics of solar cells, the first ones being favored by smooth and the second one by rough front electrodes. The optimum front electrode morphology is different for a-Si, µc-Si, and Micromorph cells and depends on the quality of the intrinsic silicon layers,[70,91] the characteristics of the doped layers,[4,20] and the type of back reflector used. The goal of this chapter is thus not to point out *the* optimal morphology, but to demonstrate the flexibility of rough LP-CVD ZnO and to discuss different methods and aspects that have to be taken into account when using different front electrode morphologies.

In summary, we showed that as-grown rough LP-CVD ZnO together with argon plasma treatments allows for the fabrication of a large variety of surface morphologies. We showed that the smoothening of the ZnO/Si interface reduces its light-trapping capability and increases reflection losses. Furthermore we demonstrated that the common roughness parameters (RMS and p-p) alone do not give a pertinent description of our morphologies for the use in thin-film silicon solar cells, but that the inclination angles of the pyramids are important. A more detailed picture of the surface morphology can be given by the angle histogram or its integral. By comparing the median angle of the lower parts of a morphology (valleys) with the upper parts (peaks and ridges), we showed for the first time a way to statistically differentiate between U-shaped and V-shaped morphologies of front ZnO electrodes.

4 TiO_2 and $SiO_{0.5}$ anti-reflection layer (ARL)

The light shining onto a solar cell is partially reflected at the interfaces between different materials before reaching the photo-active layers. This effect reduces the current generated by the solar cell and therefore has to be minimized. In section 3.4 we showed that there are no reflection losses at the ZnO/Si interface if as-grown rough ZnO is used, but that reflection becomes important if the ZnO surface is smoothened by an argon surface treatment (ArST). Although ArST reduces the light-trapping capability of as-grown rough ZnO and leads to reflection losses, smoothening of the surface is in many cases necessary to produce thin-film silicon solar cells with good electrical performance.[22,67] We therefore analyze in this chapter how the reflection losses can be minimized by index matching. Titanium dioxide (TiO_2) is a transparent oxide with a high refractive index (n), suitable for reducing reflection at the ZnO/Si interface, as previously reported by different Japanese groups.[78,92,93]

In this chapter we will first present TiO_2, produced by reactive sputtering of a pure Ti target with an Ar/H_2O gas mixture, and $SiO_{x\sim0.5}$, produced by PECVD, as two materials that can be used as anti-reflection layers. In section 4.2 we then quantify how much the reflection at the ZnO/Si interface can be reduced with a TiO_2 ARL depending on the chosen front electrode morphology, and we demonstrate that the increased transmission of light into the cell can be directly converted into a gain in cell current. In section 4.3 we show that p-type $SiO_{x\sim0.5}$ can be used simultaneously as an ARL and a field-creating p-layer with enhanced transparency for p-i-n µc-Si cells. With this approach, the refractive index (for reduced reflection losses), electrical properties (for high V_{oc} and low series resistance) and absorption (for reduced absorption losses) are the key parameters and have to be optimized in a single layer.

The main results presented in this chapter were published in two articles.[1,4]

4.1 Optical and electrical properties of TiO_2 and $SiO_{x\sim0.5}$

Figure 4-1 shows the refractive index (n) of TiO_2 and $SiO_{x\sim0.5}$ and compares the values to the refractive index of an optimal ARL for the ZnO/µc-Si interface. Taking refractive indices at 550 nm of 2.0 (see [75]) and 3.9 (see [33]) for LPCVD-ZnO and µc-Si, respectively, one can calculate a required refractive index of 2.8 for an optimum ARL, reducing the Fresnel reflection by index matching to 5.8% from 11.0% without the ARL. Taking the refractive indices of the available materials, we calculate an expected reduction of the Fresnel reflection to 6.3% with TiO_2 and 5.9% with the $SiO_{x\sim0.5}$.

Figure 4-1 also shows the extinction coefficient for the two anti-reflection materials. TiO_2 is completely transparent for the spectrum of interest for solar cells (>380 nm). $SiO_{x\sim0.5}$ shows significant absorption up to 500 nm, and absorption losses can therefore be expected, but since this layer can act at the same time as p-layer for the cell, its absorption has to be compared with other p-layers that can be used instead. Compared to p-µc-Si, which is typically used in thin-film silicon solar cells deposited on ZnO, p-type $SiO_{x\sim0.5}$ causes significantly lower absorption losses and can therefore be used as anti-reflection and window p-layer at the same time.

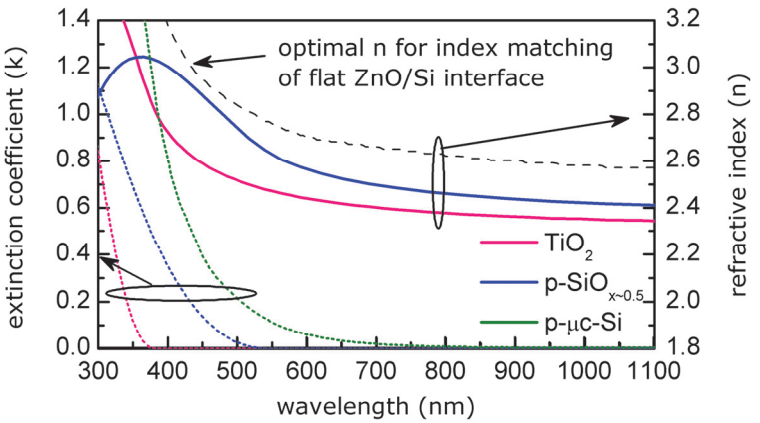

Figure 4-1: Refractive index and extinction coefficient of TiO_2 and $SiO_{x\sim0.5}$ used as ARLs. The dashed layer shows the optimal refractive index, calculated from Fresnel equations for reducing reflection at the ZnO/Si interface.

In its pure stoichiometric form, TiO_2 is an insulator, but when used in thin-film silicon solar cells, a minimum transverse conductivity of ~10^{-5} S/cm is required to avoid blocking the device current. In order to achieve this minimum conductivity, previous studies proposed two solutions for films fabricated with RF magnetron sputtering from TiO_2 targets: First, by adjusting the deposition conditions, slightly sub-stoichiometric TiO_2 can be produced due to preferential pumping of O in the deposition system. The conductivity is in this case increased due to oxygen vacancies in TiO_2.[78,93] Second, sputtering from a niobium- (Nb-) doped TiO_2 target allows Nb-doping of the growing TiO_2 films with conductivities as high as 10^{+3} S/cm.[92,94] In contrast to these previous studies, we produce TiO_2 layers by reactive magnetron sputtering from a pure Ti target (see section 2.1.5), and try to achieve the sufficient transverse conductivity by adjusting the TiO_2 stoichiometry. Avoiding rare Nb and expensive ceramic targets should be an interesting approach from the industrial point of view. In the cell configuration the ~60 nm thick TiO_2 layer is always covered by a ~10 nm thick ZnO layer, produced in the same system, to avoid H_2 induced reduction of TiO_2 during the subsequent silicon cell deposition.[78]

The p-type $SiO_{x\sim0.5}$ layers are produced by PECVD with $H_2/SiH_4/CO_2$/TMB source gas ratios of 120/1/0.7/0.005, an electrode temperature of 200 °C and a power density of 0.1 W/cm^2 in the PECVD reactor sysB (section 2.1.4). These layers were developed with the help of Michael Marending in the framework of his Master Thesis[95].

4.2 TiO_2 ARL in µc-Si solar cells

To evaluate the potential of TiO_2 as an ARL for thin-film silicon solar cells, we deposited µc-Si cells on a variety of different ZnO layers with different surface roughness and morphologies with and without TiO_2 ARLs. Figure 4-2 shows the reflectance at 550 nm of these cells versus the RMS roughness of the ZnO surface. 550 nm light shows only little absorption in the front ZnO, but is fully absorbed in the 1.5 µm thick µc-Si layer and is thus used hereafter to study the reflection originating from the ZnO/µc-Si interface. For this wavelength, a lower limit for the reflectance of µc-Si cells deposited on a glass with ZnO front electrodes can be fixed at 5.9%, which is the calculated Fresnel reflection for the flat air/glass/ZnO interfaces (dashed line). For both Z2 and Z5 there is no reflection, in agreement with results of a different series used in Figure 3-14, and obviously nothing can be gained when adding a TiO_2 ARL. For increasing ArST times, the reflectance increases but can be completely canceled by adding a TiO_2 ARL. For a nearly flat, sputtered ZnO film, a TiO_2 ARL reduced the reflection from 13.3% to 6.4% for the glass/ZnO/Si stack, corresponding to a reduction from 7.4% to 0.5% for the ZnO/Si interface. Index matching at a flat interface with one layer can only reduce the reflection from 11% to 5.9%, and the additional gain here is from interference effects in the ~60 nm thick TiO_2 ARL, which completely cancels the reflection at 550 nm.

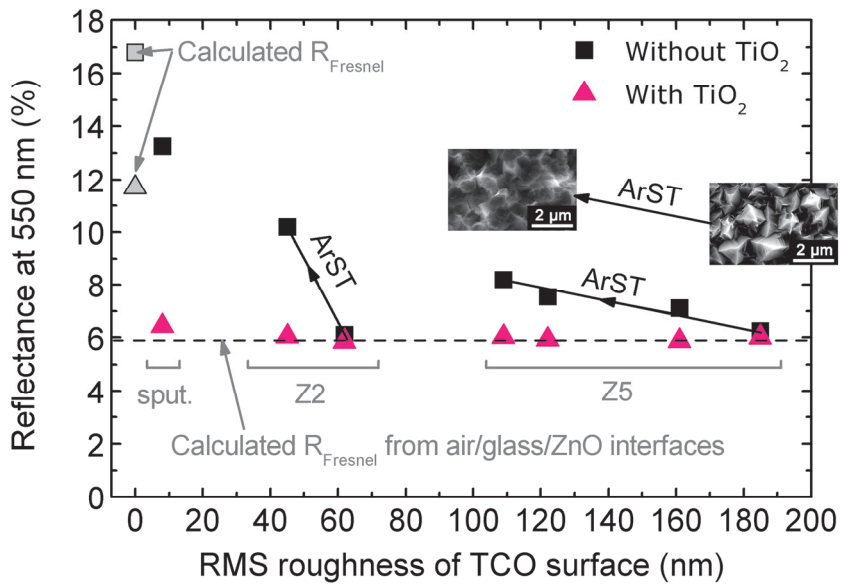

Figure 4-2: Reflectance at 550 nm of a glass/ZnO/µc-Si stack with different ZnO/µc-Si interface morphologies without and with a ~60 nm TiO_2 ARL between the ZnO and the µc-Si layers.

Figure 4-3 (a) shows the reflectance of four cells fabricated in one deposition run. Two standard cells without ARLs (black lines) are deposited on LP-CVD ZnO with different surface morphologies, obtained after short and long surface treatments (dashed and solid lines, respectively). The long surface treatment decreases the RMS roughness of the ZnO from 180 to 91 nm with respect to the short ArST, leading to an increase in reflectance at the ZnO/Si interface from 1.1 to 4.3% at 550 nm. The pink lines show the reflectance of the same cells

deposited on the same ZnO front electrodes, but with a TiO_2 ARL added between the ZnO and the silicon layer. The ~60 nm thick TiO_2 layer reduces the reflectance at the ZnO/Si interface for 550 nm light from 1.1% to 0.1% and from 4.3% to 0.5% for the ZnO prepared with short and long surface treatments, respectively. The reflectance of the cell increases strongly from 600 to 1100 nm because an increasing portion of light reflected at the opaque back reflector. For wavelengths above 1100 nm, the reflectance decreases again due to increasing free carrier absorption in the ZnO layers. The small increase of reflectance with TiO_2 at 400 nm is due to constructive interference of light reflected at the ZnO/TiO_2 and the TiO_2/Si interfaces. This interference effect is also present at longer wavelengths (>600nm), but negligible compared to the much stronger contribution of light leaving the solar cell after reflection at the back reflector. Figure 4-3 (b) shows the external quantum efficiency (EQE) and the internal quantum efficiency (IQE=EQE/(1–reflectance)) of the cells with the long ArST from (a). The EQE increases from 82% to 86% corresponding to the expected gain from the reduced reflection. Integrated over the whole solar spectrum, this leads in this case to an increase in J_{sc} from 23.4 to 24.3 mA/cm^2. The superposition of the two IQE curves for these cells confirms that the gain in EQE is entirely due to optical ARL effects and that the µc-Si cells are identical.

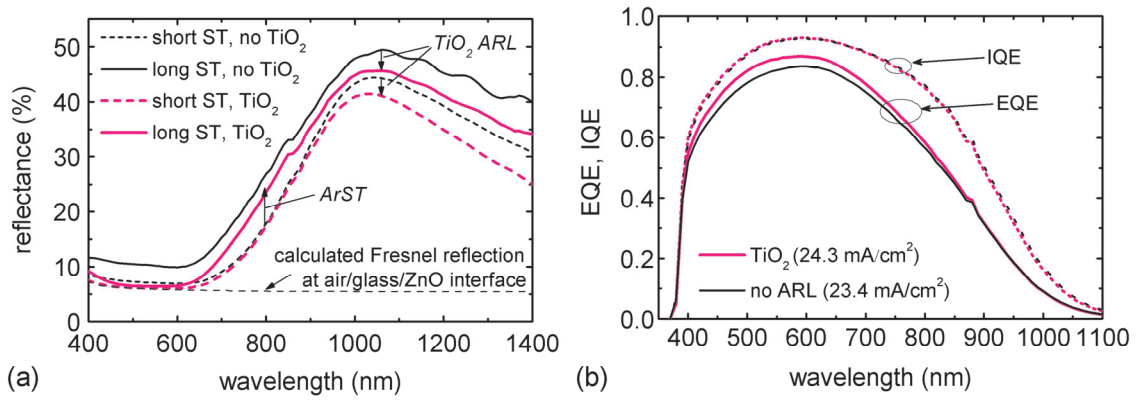

Figure 4-3: (a) Reflectance of four cells (Z5-ArX',1.8) fabricated in one run deposited on ZnO prepared with a short (20') and a long (80') ArST, with and without TiO_2 ARLs. (B) EQE (acquired at –2V) and IQE of the two cells deposited on the ZnO with long ArST, with and without TiO_2 ARLs.

As mentioned in the previous section, sufficient transverse conductivity is difficult to achieve in TiO_2 layers in a reproducible way due to the sensitive reactive sputtering process and the limited controls available on our deposition system. In most of the cells, an additional series resistance is therefore measured with TiO_2 ARLs. Nevertheless, we produced cells with ~60 nm TiO_2 ARLs with a relative increase in J_{sc} of 2%, with an increase in series resistance of only 0.2 Ω cm^2 leading to a gain in efficiency. With this proof of concept, we conclude that it is possible to use reactive sputtering to produce efficient TiO_2 ARLs in thin-film silicon solar cells.

4.3 p-nc-$SiO_{0.5}$ anti-reflection layer in µc-Si solar cells

Instead of inserting an additional layer between the front electrode and the silicon, index matching can be achieved by adjusting the refractive index of the p-layer used in the p-i-n configuration of the thin-film silicon solar cell. Figure 4-4 (a) shows the EQE of two µc-Si cells deposited on a rough, but U-shaped front electrode (Z5-Ar20'), one with standard p-µc-Si and the other with p-type $SiO_{x\sim0.5}$ comprising a nanocrystalline silicon phase (p-nc-$SiO_{0.5}$). The significant increase in the EQE between 400 and 550 nm shows that the p-nc-$SiO_{0.5}$ is an excellent window layer. The identical absorptance (1–reflectance) of the cells confirms that the entire current gain of 1.5 mA/cm^2 can be attributed to reduced parasitic absorption in the p-layer. Since the electrical characteristics of both cells are similar (V_{oc} = 0.50 V, *FF* = 70%), the efficiency is in this case increased from 8.2% to 8.8%. In this configuration, the anti-reflection effect cannot be observed, because the roughness at the ZnO/Si interface already cancels almost all reflection. To observe the anti-reflection effect with the p-nc-$SiO_{0.5}$ layer, we deposited the µc-Si cell on a polished ZnO front electrode (Z5-p). In this case, the reflection at the flat ZnO/Si interface causes significant current losses, as shown by the absorptance curves in Figure 4-4 (b). Due to the lower refractive index of the p-nc-$SiO_{0.5}$ ($n_{@400nm}$ = 2.97) when compared to p-µc-Si ($n_{@400nm}$ = 4.62), the reflection at this interface is decreased by index matching. In this case, the increased absorptance of the cell, in combination with the reduced parasitic absorption in the p-layer, increases the current density by 2.1 mA/cm^2 for unchanged electrical characteristics (V_{oc} = 0.50 V, *FF* = 70%). The thickness of the p-nc-$SiO_{0.5}$ layer is in this case 20 nm which gives good anti-reflection conditions for the short wavelengths, but not for 550 nm. Thicker p-nc-$SiO_{0.5}$ layers can shift the reflection minimum to longer wavelengths, but the gain in current is in this case limited due to increasing absorption in the thicker p-nc-$SiO_{0.5}$ layer.

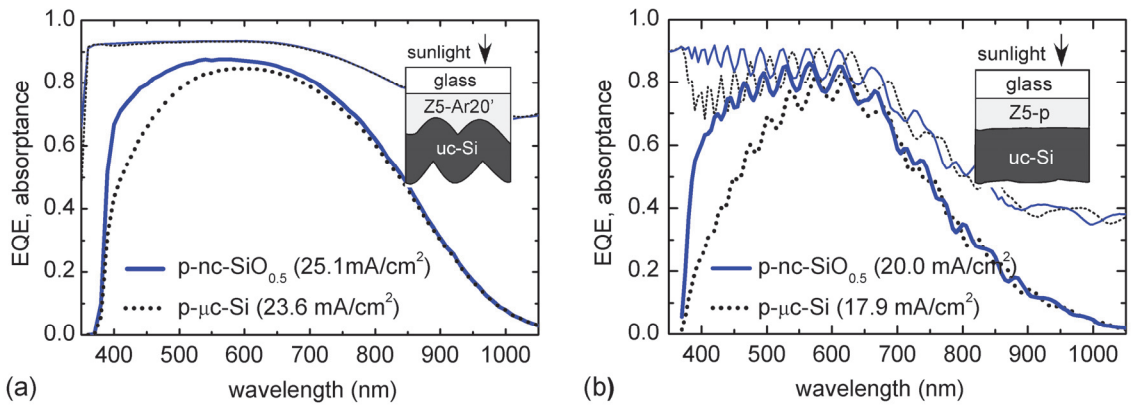

Figure 4-4: EQE of four 1.5 µm thick µc-Si cells deposited on (a) rough (Z5-Ar20') and (b) flat (Z5-p) front electrode with p-µc-Si (dotted black) and p-nc-$SiO_{0.5}$ (solid blue) layers. The absorptance (1–reflectance) of the cells are shown as thinner lines.

4.4 Conclusion

In summary, we presented TiO_2 deposited by reactive sputtering of a Ti target and p-nc-$SiO_{0.5}$ deposited by PECVD as two materials with appropriate refractive indices to produce an anti-reflection effect at the ZnO/Si interface. We measured reflectance values at the ZnO/Si interface ranging from 0% to 7.4% and successfully canceled the reflectance for a given wavelength resulting in important current gains on flat and strongly smoothened front electrodes. In parallel to this work, we developed novel materials and processes that allow for relatively good electrical properties of solar cells deposited on rough front electrodes leading to record cell efficiencies.[4,20,70,91] Thanks to these advances, the rough front electrodes with their high light-trapping potential are believed to be the key to high solar cell currents. As the reflection on the ZnO/Si interface is canceled by the roughness of these substrates, there is no gain when using an ARL. It was therefore decided not to continue investigations of ARLs, and no work was done to improve the reproducibility of TiO_2 produced by reactive magnetron sputtering. Nevertheless, it is an important step to quantify the reflection losses for different front electrode morphologies as well as to show that ARLs can be used to reduce those reflection losses. It is also possible that in the future photonic structures at the back of the cell[54,96] or triple or quadruple junction configurations may emerge as alternatives to the Micromorph tandem cell deposited on rough front electrodes. For such cases a smoother ZnO/Si interface will probably be used, and the work on ARLs could then be continued and multi-layer stacks could be developed to achieve broad-band ARL coatings.

5 Mixed-phase silicon oxide layers

The first developments of silicon oxide (SiO_x) films were directed towards their application as intermediate reflecting layers (IRL) in Micromorph cells. The goal was to lower the refractive index and thereby increase reflectivity, while keeping the minimum required conductivity to avoid additional series resistance in the solar cell. Later, we started investigating a larger variety of p- and n-type SiO_x layers for different functionalities in thin-film silicon solar cells. In this chapter we focus on the material properties of SiO_x and discuss the influence of SiO_x layers in the cells in chapter 6. In section 5.1, we show the opto-electronic properties and Raman crystallinity measurements of developed SiO_x layers. Section 5.2 gives a more precise picture of the elemental composition of these films and section 5.3 reveals that SiO_x is not a homogenous material on the nanometer scale, but that there is $Si/SiO_{y\sim2}$ phase separation as evidenced by state-of-the art microscopy techniques. We show that for certain deposition conditions it is possible to grow silicon filaments tens of nanometers long, but only a few nanometers wide, embedded in a $SiO_{y\sim2}$ matrix. In section 5.4, we discuss the current understanding of the main growth mechanisms and we show in section 5.5 that our SiO_x films exhibit photoluminescence due to quantum confinement in the nanometer-sized silicon grains embedded in amorphous $SiO_{y\sim2}$.

The layers presented in this chapter are deposited with PECVD using a gas mixture of hydrogen (H_2), silane (SiH_4), carbon dioxide (CO_2), phosphine (PH_3) and trimethylboron ($B(CH_3)_3$). They are deposited in the small-scale reactor sysB, and the process power is kept at 0.1 W/cm^2, the pressure at 0.7 mbar and the frequency at 110 MHz for all layers.

Most of the results shown in this chapter were published in articles.[2-6]

5.1 Opto-electronic properties and Raman crystallinity

Figure 5-1 (a) shows the dark conductivity (σ), the Raman crystalline fraction of the silicon-rich phase (*Si Rc*), and the absorption coefficient (α) of p- and n-type SiO_x layers as a function of CO_2/SiH_4 gas flow ratio (see section 2.2 for measurement details). The layers without oxygen are typical p- and n-type µc-Si layers used in µc-Si cells. The H_2 dilution is kept at 100 for p-type layers and 50 for n-type layers, because in the p-i-n configuration it is common to use a higher H_2 dilution for p-layers grown on ZnO substrates due to their longer microcrystalline incubation phase compared to n-layers which are grown on i-µc-Si layers. For both p- and n-type layers, the dark in-plane conductivity is around 10 S/cm for oxygen-free samples, and decreases rapidly with higher CO_2/SiH_4 gas ratios, due to an increasing amount of oxygen incorporated in the SiO_x films. Furthermore, increasing the CO_2/SiH_4 gas ratio reduces the Raman crystalline fraction of the silicon-rich phase in the SiO_x layers (not taking into account the oxygen-rich phase), and decreases the optical absorption coefficient α.

Figure 5-1 (b) shows the results obtained for different doping gas concentrations, ranging from 0‰ to 50‰, with a constant CO_2/SiH_4 gas ratio of 0.5. P-type doping with trimethylboron (TMB) rapidly reduces the crystalline fraction of the silicon phase, and a maximum dark conductivity is obtained due to the counteracting influences of doping and amorphization at TMB/SiH_4 = 8‰. The same optimum for boron doping gas ratio was found in previous studies for µc-Si films doped with B_2H_6.[97,98] The amorphizing effect of TMB limits the oxygen content in SiO_x films to x~0.5 (CO_2/SiH_4 = 0.7) before the films become too resistive to be used in thin-film

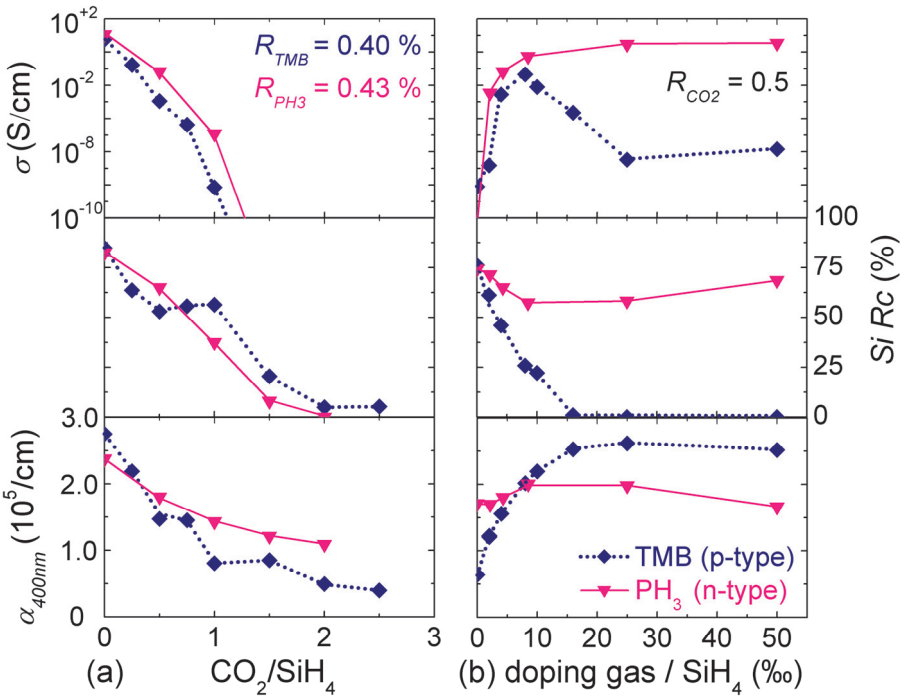

Figure 5-1: In-plane dark conductivity (σ), silicon Raman crystalline fraction (*Si Rc*), and absorption coefficient (α) of p- and n-type SiO_x layers (H_2/SiH_4 = 100 and 50, respectively) versus (a) CO_2/SiH_4 and (b) doping gas/SiH_4 ratio. (p-SiO_x layers were deposited and measured by M. Marending in his master thesis.)

silicon solar cells.

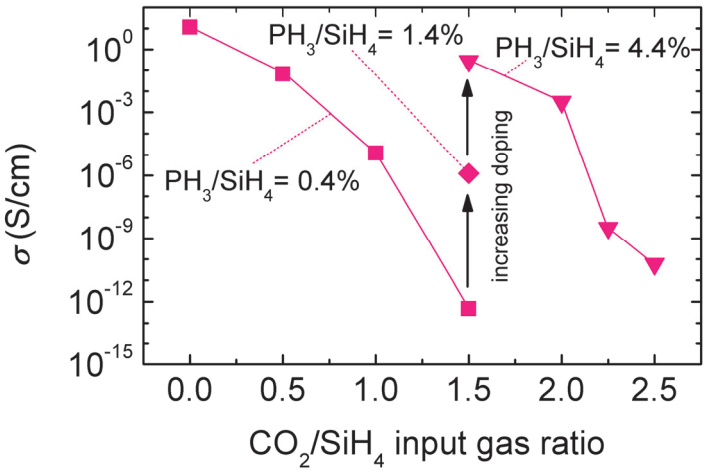

Figure 5-2: In-plane dark conductivity (σ) of ~100 nm thick SiO_x (H_2/SiH_4 = 50) layers versus CO_2/SiH_4 and PH_3/SiH_4 input gas ratios.

For n-type doping with PH_3, however, dark conductivity continuously increases with increasing doping gas concentration as phosphorous does not reduce the crystalline fraction of the silicon phase. Therefore, high phosphorous doping concentrations in n-SiO_x can partially make up for lower conductivity due to oxygen incorporation, allowing sufficient conductivity to be maintained in SiO_x layers produced with much higher CO_2/SiH_4 gas flow ratios, as shown in Figure 5-2.

The properties presented above give a good description of what is happening in the SiO_x material when varying the different input gas ratios. However for use as an IRL, there are two other properties which are of interest: the refractive index, which has to be minimized to increase the refractive index contrast to the silicon layer and so increase the reflectivity of the IRL; and the transverse conductivity, which has to be kept above a minimum value to avoid additional series resistance in the solar cell. The transverse conductivity limit depends on the thickness of the SiO_x layer in the cell and the cell's operation point. For the use as an IRL in a Micromorph cell, the limit is approximately 10^{-5} S/cm, which corresponds to an increase in series resistance of 1 $\Omega \cdot cm^2$ for a 100 nm thick layer. In a Micromorph cell, operated at V/J ~ 100 $\Omega \cdot cm^2$ this corresponds to a maximal power loss of 1%.

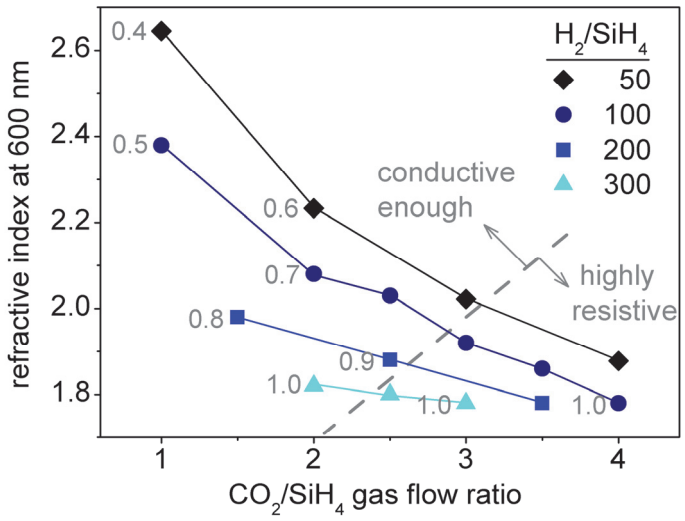

Figure 5-3: Refractive index for n-SiO_x layers produced with different CO_2/SiH_4 and H_2/SiH_4 precursor gas ratios (constant PH_3/SiH_4 ~0.1). The O:Si ratio is given by the grey numbers left of the symbols for some layers to illustrate its inverse correlation to the refractive index. The dashed line segregates the n-SiO_x layers with respect to the minimal transverse conductivity of 10^{-5} S/cm required for use in thin-film silicon solar cells.

Figure 5-3 shows the refractive index of ~80 nm thick layers produced with different CO_2/SiH_4 and H_2/SiH_4 gas ratios and constant PH_3/SiH_4 ~ 0.1. N-type SiO_x is preferred for use as an IRL because we achieved sufficiently conductive films with lower refractive indices than for p-type SiO_x. First, it can be seen that increasing the CO_2/SiH_4 input gas ratio reduces the refractive index of the layer, due to increasing oxygen content in the films. Then, it can be noted that increasing H_2/SiH_4 also leads to lower refractive indices, which is also due to increased oxygen content in the films as demonstrated by the O:Si ratios (measured by Rutherford Backscattering Spectroscopy (RBS)), given by the grey numbers for some points. By adjusting these two gas flow ratios, the refractive index at 600 nm can be tuned to any value between 4.3 for a-Si and 1.5 for SiO_2. Figure 5-3 shows the layers of interest for use as IRLs. The transverse conductivity for these layers is deduced from *I-V* curves of full Micromorph cells with SiO_x IRLs or by measuring a simpler ZnO/n-µc-Si/SiO_x/n-µc-Si/ZnO stack deposited for this purpose only (section 2.2.5). Although this measurement technique does not allow us to precisely quantify the transverse conductivity for all of these layers, it allows us to determine whether the transverse conductivity of the SiO_x layer is below or above 10^{-5} S/cm by showing additional series resistance or not, when compared to stacks or cells without SiO_x layers. The dashed line in Figure 5-3 shows how in the experimental measurements the SiO_x layers are segregated with respect to this transverse conductivity criterion. As this border line does not lie horizontally but diagonally in the graph, we can conclude that highly H_2 diluted process conditions allow us to reach lower refractive indices than the process condition with less H_2 dilution for the same transverse conductivity. It is interesting to note here that we found that there is strong anisotropy in the conductivity of oxygen-rich films produced with high H_2 dilution. Typically, we measured transverse conductivities for ~100 nm thick $SiO_{x\sim1}$ films > 10^{-5} S/cm, but measured in-plane conductivities in such films of 10^{-10} S/cm or below, indicating an anisotropy of at least 5 orders of magnitude.

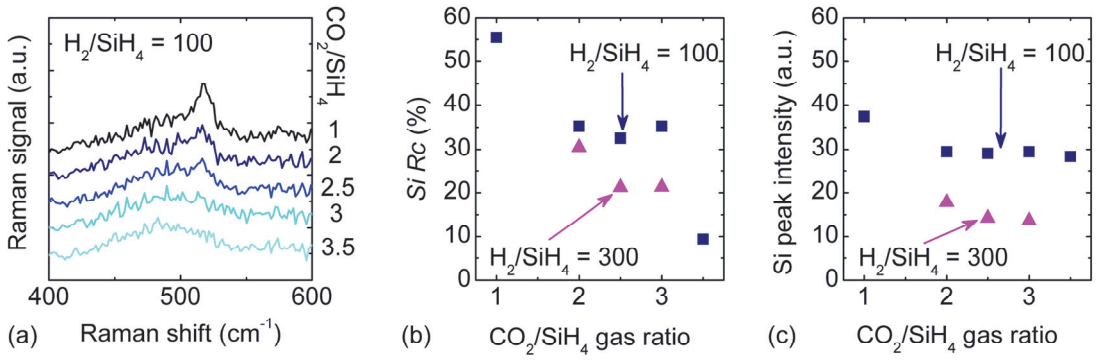

Figure 5-4: (a) Raman spectra of the SiO_x layers on glass deposited with H_2/SiH_4 = 100 and different CO_2/SiH_4 gas ratios. (b) Raman crystalline fraction in the silicon phase and (c) total Raman silicon peak intensity for SiO_x films produced with H_2/SiH_4 = 100 and 300.

To gain further insight into the structural properties of these oxygen-rich SiO_x layers we performed Raman scattering measurements and calculated the Raman crystalline fraction of the silicon-rich phase as for µc-Si layers.[79] The Raman signal of these layers, which stems from the silicon-rich phase only, becomes noisy because the oxygen-rich phase, which does not contribute to the signal, makes up the majority of the film volume. Figure 5-4 (a) shows the Raman spectra of SiO_x layers produced with H_2/SiH_4 = 100, and (b) and (c) compare the calculated Raman crystalline fraction in the silicon phase and the total Raman silicon peak signal intensity as a function of CO_2/SiH_4 gas ratio for SiO_x layers produced with H_2/SiH_4 = 100 and 300. The crystalline fraction decreases with increasing CO_2/SiH_4 gas ratio (b) whereas the total silicon Raman signal intensity remains nearly constant (c). The total Raman peak intensity for the SiO_x layers produced with H_2/SiH_4 = 100 is significantly higher than for layers produced with H_2/SiH_4 = 300 due to the higher silicon content of these layers, which is in agreement with the difference in refractive indices (Figure 5-3). Based on these observations we conclude that, high H_2/SiH_4 gas ratios are necessary to obtain oxygen-rich films (low Raman silicon peak intensity) with good crystallinity of the remaining silicon-rich phase.

5.2 Elemental composition of the SiO_x films

The n-type SiO_x layers shown in this thesis report are deposited by PECVD from a gas mixture of SiH_4, H_2, CO_2 and PH_3 (section 2.1.2). To precisely describe the material composition we could therefore use the notation $Si_vO_wC_xH_yP_z$, but as silicon and oxygen are the two main components in all the layers presented here and largely determine the optical and electrical properties, we use SiO_x as our abbreviation for the more complex chemical composition.

With secondary ion mass spectroscopy (SIMS) performed on our samples by the "Evans Analytical Group" in California, USA, we measured the carbon content of the films to be ~$4 \cdot 10^{20}$ atoms/cm^3 (~2 atomic percent). The carbon content stems from the CO_2 used as a source gas for oxygen, but the value did not change by varying CO_2/SiH_4 from 2.5 to 5, nor by varying H_2/SiH_4 from 100 to 200. We do not expect such low values of carbon to play a major role in the film properties, and we made no further investigation.

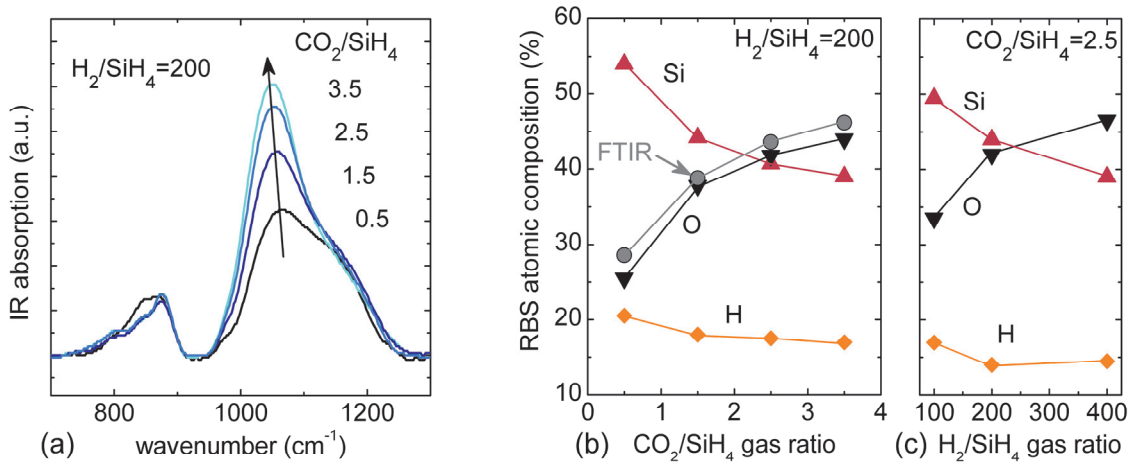

Figure 5-5: (a) Infrared absorption peak of the Si-O-Si stretching mode at 1050 cm^{-1} of 100 nm thick SiO_x layers. (b)-(c) Silicon, oxygen, and hydrogen content measured by RBS and Hydrogen Forward Scattering for different source gas ratios, and oxygen content as calculated from FTIR measurements for comparison.

As shown in the previous section, the easiest way to increase the oxygen content in SiO_x films is by increasing the CO_2/SiH_4 gas flow ratio during deposition. RBS was performed on our samples by the Evans Analytical Group to quantify the O:Si and H:Si ratios in the deposited SiO_x films. Because this is an expensive method, we usually deposited stacks with 3–5 different SiO_x layers (each 100 nm thick) on one wafer substrate in order to get several data points in one run. An inexpensive way to quantify the oxygen content in SiO_x films is by Fourier Transform Infrared spectroscopy (FTIR, section 2.2.3). Figure 5-5 (a) shows the FTIR absorption peak of the Si-O-Si stretching mode around 1050 cm^{-1}.[99] By integrating the area under this absorption peak and multiplying it with a proportionality constant it is possible to estimate the oxygen content in the film, but a broad range of proportionality constants are proposed in the literature.[99-101] In our case we found the best correlation to RBS measurements when using the proportionality constant $A_{SiO} = 1.48 \cdot 10^{19}$ cm^{-2} proposed by He et al.[101]

From Figure 5-5 (c) it becomes clear that the oxygen content in the films is not only determined by the CO_2/SiH_4, but that increasing the H_2/SiH_4 gas ratio also enhances oxygen incorporation into the film. This phenomena was also observed by other groups and Iftiquar et al.[100] proposed the following explanation: In an RF plasma, CO_2 is split into CO + O, but because O and CO are highly reactive, they mostly recombine to form CO_2. If H ions are present, the formation of OH hinders this backward reaction. Because the reaction between OH and silicon is strong, OH can easily dissociate Si–Si bonds on the growing surface and become incorporated into the network.[102] In this model, OH species are thought to be mainly responsible for incorporation of oxygen into the film. When the deposition pressure is lowered or the RF power increased, the electron temperature becomes higher. As a result, there is more splitting of hydrogen molecules, which increases the concentration of OH complexes and the incorporation of oxygen into the growing SiO_x film, which also fits with our experience with varying power and pressure, not shown in this report.

The hydrogen content in SiO_x films can also be measured by FTIR, but the absorption peak is lower than the Si-O-Si peak and much thicker films are thus necessary.[99,100] As we suspected our films to be inhomogeneous in depth we did not try this, but sent some samples to the Evans Analytical Group to quantify the hydrogen content by Hydrogen Forward Scattering (HFS). Interestingly the hydrogen content in our films is ~15 atomic percent for all the analyzed films deposited with H_2/SiH_4 of 100 and 300 and does not correlate with H_2 dilution in the plasma, but shows a slight correlation to the silicon content of the SiO_x films. This tendency could be a result of hydrogen atoms mainly being bound to silicon atoms and not to oxygen atoms, as predicted by Smith et al.[102] with free energy models of a-Si alloys.

For different SiO_x layers deposited with PH_3/SiH_4 ratios of 0.1 (highest PH_3 gas flows used in these studies), the Evans Analytical Group measured the phosphorus concentration with SIMS to be $4 \cdot 10^{20}$–$2 \cdot 10^{21}$ atoms/cm^3, corresponding to 2–6 atomic percent in a $SiO_{x=1}$ film with $2.9 \cdot 10^{22}$ atoms/cm^3. These concentrations are far higher than what is regularly used for n-type doping of silicon and it is not clear why such high phosphorus contents are necessary to maintain sufficient transverse conductivity. It can be speculated that phosphorus segregates at the Si-grain boundaries, but further studies have to be made to clarify the different roles of phosphorus in the different phases. To motivate such studies, we mention that the phosphorus content showed a correlation to the silicon content of the films, similar to the hydrogen content.

5.3 Si/$SiO_{y\sim2}$ phase-separation visualized by EELS-EFTEM

The experimentally observed electrical anisotropy and the Raman measurements presented in section 5.1 already give good evidence of a mixed-phase structure in the SiO_x films produced with high H_2 dilution. To get a better understanding of these particular properties we kept trying different microscopy techniques over the course of almost two years until we found a method that combines electron energy loss spectroscopy (EELS) and energy filtered transmission electron microscopy (EFTEM). The results shown here were only made possible due to the important contribution of Duncan Alexander and his co-workers at CIME, EPFL. (All the EELS-EFTEM analyses were carried out by D. Alexander.)

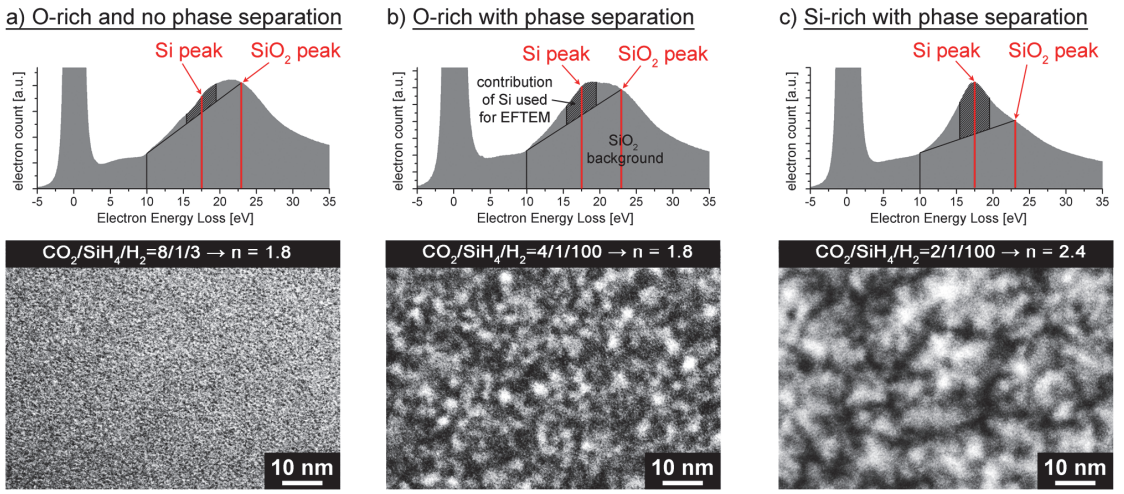

Figure 5-6: EELS spectra of 50 nm thick SiO_x plan-view samples showing the SiO_2-type plasmon peaks at 23 eV and the Si-type plasmon peak fixed to its average position at 17.5 eV for EFTEM analysis. The corresponding silicon map (white = silicon-rich, black = oxygen-rich) is obtained from EFTEM using a 4 eV window around the silicon plasmon peak and subtracting the background contribution of the neighboring SiO_2 peak contribution (dark grey region in EELS spectra).[81]

In this EELS-EFTEM technique we take advantage of the slightly different bulk plasmon energies of Si (~17.5 eV) and SiO_2 (~23 eV), illustrated with three different EELS spectra in Figure 5-6. By selecting with EFTEM only electrons from a 4 eV window around the silicon plasmon peak and subtracting the background contribution of the neighboring SiO_2 peak, it is possible to make a nanometer-scale silicon map of the layers as proposed in previous studies.[81,103,104] The white regions in these EFTEM silicon maps represent silicon-rich material and the dark regions oxygen-rich material. The oxygen-rich layer (Figure 5-6 (a)) is produced with low hydrogen dilution and shows no phase-separation. The silicon plasmon peak cannot be distinguished clearly in the EELS spectra and the resulting EFTEM image is noisy. The second oxygen-rich layer (Figure 5-6 (b)) is produced with a higher hydrogen dilution and the appearance of a distinct silicon plasmon absorption peak in the EELS spectrum is evidence of a silicon phase. The EFTEM image reveals nanometer-scale phase-separation into a silicon/silicon oxide (Si/$SiO_{y\sim2}$) mixed-phase material with silicon nanograins 2–5 nm in diameter. The layer shown in Figure 5-6 (c) is produced with a lower CO_2/SiH_4 gas ratio

compared to layer (b), resulting in a film with lower oxygen content and with larger silicon grains (3–8 nm).

Figure 5-7 shows cross-section EFTEM images of three SiO_x layers (encircled in the insert) with the same refractive index, but produced with different source gas ratios. The SiO_x films are grown on a µc-Si nucleation layer to reproduce the same growth conditions as are used for IRLs in the Micromorph cell. The film produced with low hydrogen dilution (a) results in a homogenous SiO_x film without phase separation. A H_2 dilution of 100 (b) results in a $Si/SiO_{y\sim2}$ mixed-phase material with nanometer-sized silicon grains that grow in clusters or "silicon trees." The highest H_2 dilution of 300 (c) gives rise to silicon filaments, tens of nanometers long, but only a few nanometers wide, embedded in an amorphous oxygen-rich matrix.

If heavily doped with phosphorus, the filamentous nanostructure of film (c) produces a strong electrical anisotropy: while the three layers in Figure 5-7 with refractive index of 1.8 all have in-plane conductivities below 10^{-10} S/cm, the layer with the long silicon filaments has a transverse conductivity above 10^{-5} S/cm. This transverse conductivity is sufficient to avoid blocking the solar cell current, and so renders the film suitable for the use as a doped layer in solar cells.

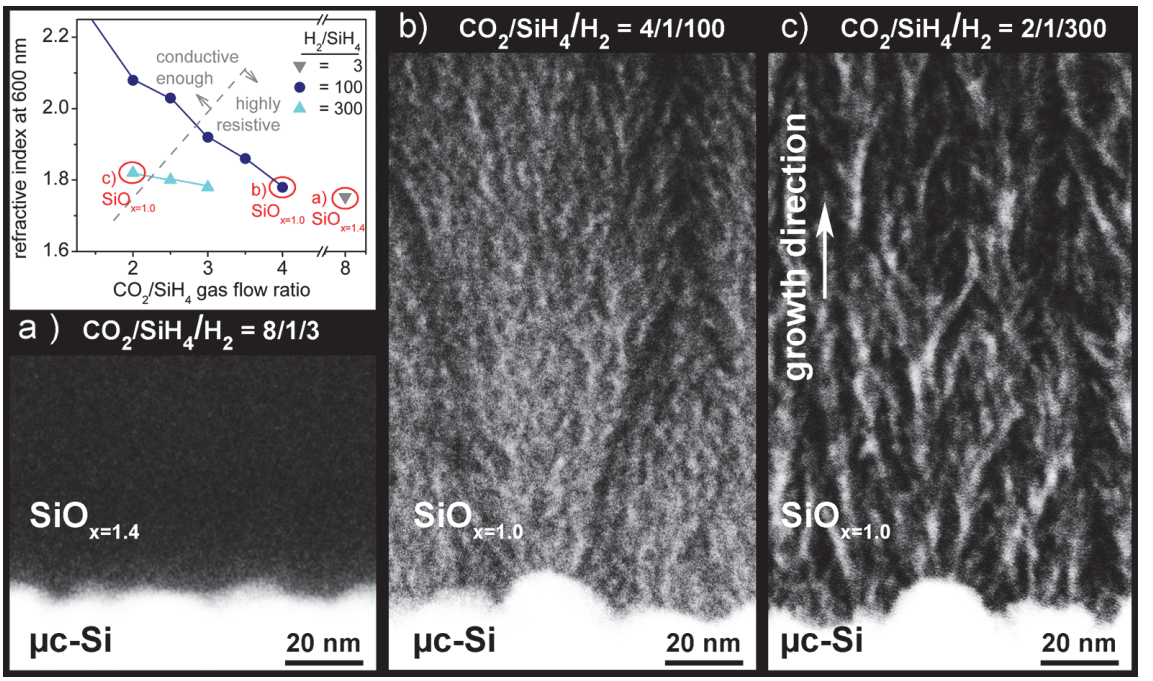

Figure 5-7: Cross-section EFTEM images (white = silicon) of the three SiO_x films encircled in inset, with the same refractive index of 1.8, but different nanostructure due to different input gas ratios used for the deposition. The layers are grown onto a µc-Si seed layer to ensure a good electrical contact for transverse conductivity measurements.

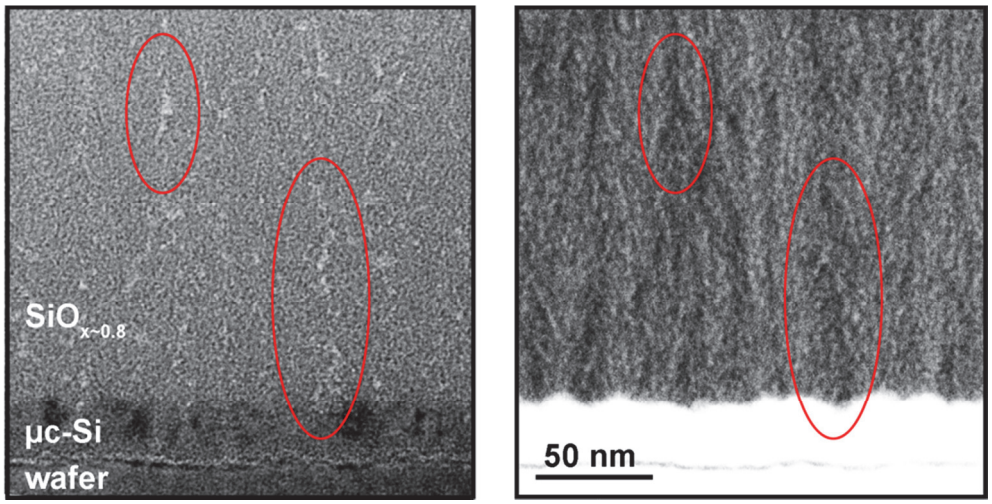

Figure 5-8: Cross-section bright-field (left) and EFTEM silicon map (right) of a $SiO_{x\sim0.8}$ layer ($CO_2/SiH_4/H_2$ = 2.5/1/100) deposited on silicon wafer covered with a 30 nm µc-Si incubation layer. The brighter parts in the SiO_x material in the bright-field image are due to nano-porosities. The red ovals are guides to the eye to indicate the same spots in the EFTEM map of the silicon phase.

Figure 5-8 compares a standard-bright field TEM image with an EFTEM silicon map for a cross-section of a $SiO_{x=0.8}$ layer deposited with a H_2 dilution of 100. A polished wafer covered with 30nm µc-Si as a nucleation layer was used as a substrate. This comparison shows that EFTEM analysis really gives additional information for the SiO_x layer that cannot be seen in regular bright-field TEM techniques. The “silicon trees” can again clearly be seen and they always start on top of the bumps that stem from the deposition of the µc-Si nucleation layer. This is caused by the isotropic incidence of adatoms in PECVD, leading to a reduced growth in valleys due to

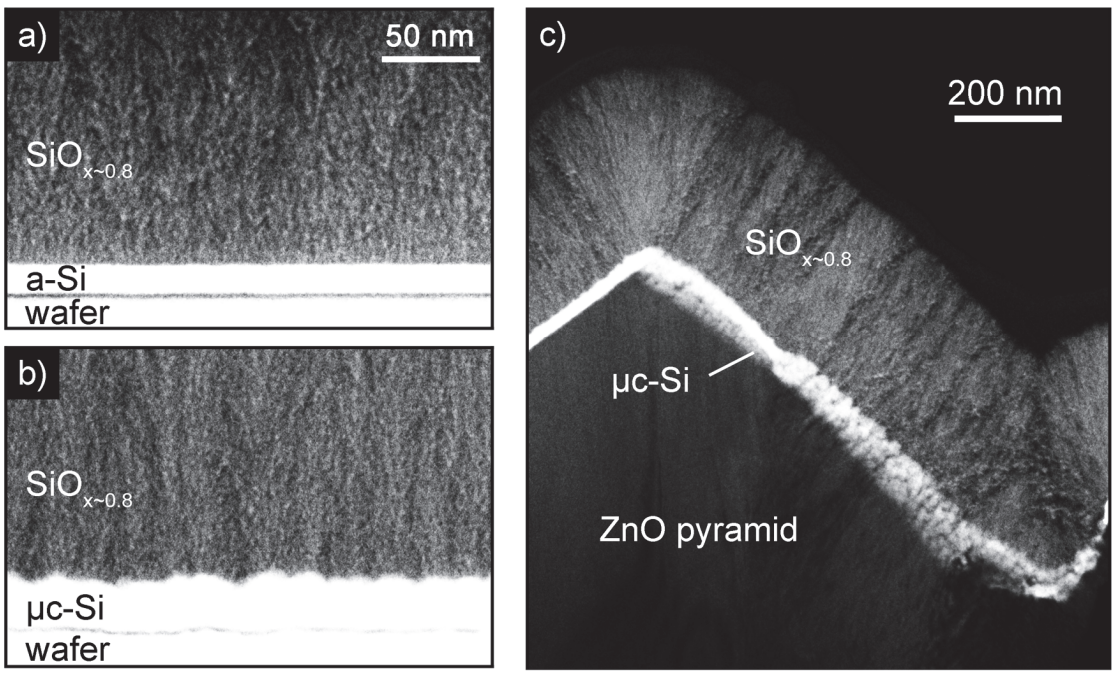

Figure 5-9: Cross-section EFTEM images of $SiO_{x\sim0.8}$ deposited on a polished silicon wafer with a-Si (a) and µc-Si (b) nucleation layers and deposited on rough LPCVD ZnO substrate (c).

shadowing by the bumps or peaks.[105] The features that start to grow on the higher points of the substrate therefore rapidly outgrow the valley regions and grow larger until they collide with other growth zones from neighboring bumps. The regions where different growth zones collide have been intensely studied in µc-Si and are known to form regions of less dense material (called cracks).[64-66] Similarly, for the SiO_x layers shown here, less dense regions can be seen in the bright-field image (lighter spots), which coincide with the regions between neighboring "silicon trees."

Figure 5-9 shows cross-section EFTEM images of a $SiO_{x\sim0.8}$ layer on three different substrates: wafer/a-Si, wafer/µc-Si, and wafer/ZnO/µc-Si. The phase separation of the SiO_x layers grown on a-Si and µc-Si incubation layers looks similar, but the tree-like growth is completely absent in the first ~20 nm for the SiO_x layer deposited on the flat a-Si layer. Afterwards similar but less organized tree-like structures appear, probably due to increasing roughness created by the growth of the SiO_x layer itself. Of special interest for the use as an IRL in a Micromorph cell is the layer in Figure 5-9 (c), which shows how the SiO_x grows on a rough LP-CVD ZnO substrate. On top of the pyramid, the "silicon trees" fan out, whereas in the valleys they collide and form a region with less dense and less organized material, similar to crack-formation in µc-Si silicon.

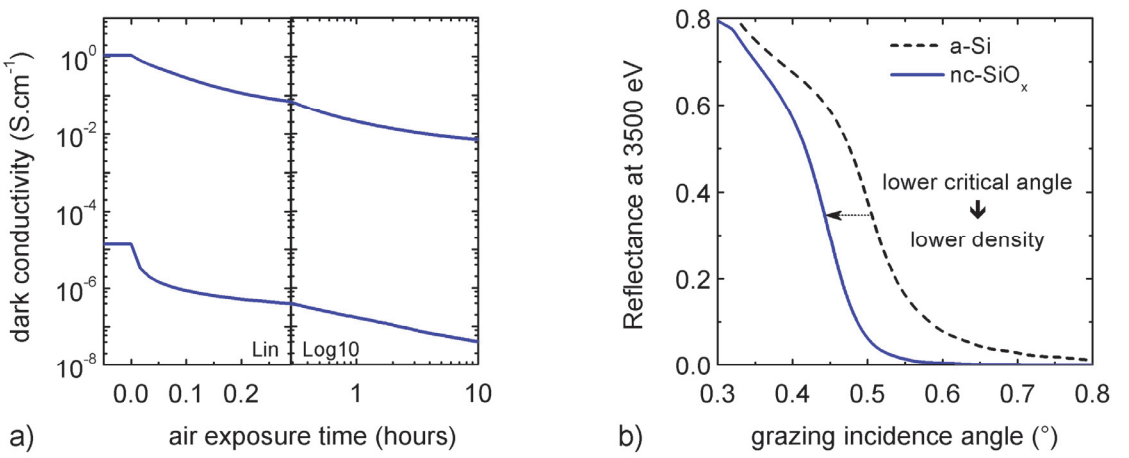

Figure 5-10: (a) Decreasing dark conductivity due to air exposure of two different 100 nm thick SiO_x layers. (b) X-ray reflectometry measurements at 3500 eV (far away from the Si absorption edge) indicating that SiO_x is significantly less dense than a-Si. (These layers were deposited in KaiS, at different process conditions than the other layers presented in this chapter. Layers in (b) were fabricated by Linus Löfgren and measured by Michael Krumrey.)

The nano-porosity between individual "silicon trees" shown in Figure 5-8 can also explain the decreasing dark conductivity of SiO_x layers when exposed to air, illustrated by two different SiO_x layers in Figure 5-10 (a). The initial conductivity of these layers can be recovered by annealing the samples for 90' at 180 °C in vacuum. Water vapor penetrating into nano-pores of SiO_x films is believed to be the reason for this reversible in-plane conductivity degradation. The existence of nano-porosity is also evidenced by X-ray reflectometry measurements shown in Figure 5-10 (b) revealing a lower critical angle for SiO_x than for device-quality a-Si, suggesting lower material density.[106] These X-ray reflectometry measurements are performed with

synchrotron radiation at the PTB four-crystal monochromator beamline at BESSY II.[107] Such a significant amount of nano-porosity, as shown here by three different techniques, probably also reduces the refractive index of the material. If this nano-porosity is larger in mixed-phase films compared to homogenous SiO_x layers this can also at least partially explain why the homogenous $SiO_{x=1.4}$ shown in Figure 5-7, needs higher oxygen content to reach the same refractive index than the phase-separated and nano-porous $SiO_{x=1}$ shown in the same Figure.

5.4 Growth model for phase separation

Previous studies have shown that it is possible to obtain silicon dots embedded in SiO_2 from homogenously grown SiO_x films by post-deposition high-temperature annealing at ~1000 °C.[81,108,109] From these studies we can conclude that phase separation in SiO_x films into Si and SiO_2 regions is energetically favorable but limited by atom diffusion. As our films are produced at substrate temperatures of 200 °C, there has to be additional energy input to allow for phase separation in our films. From studies on pure, plasma-deposited silicon, it is known that atomic hydrogen from the plasma increases the structural order of the growing film via relaxation of strained bonds and an increase of adatom diffusion length through surface heating and passivation of surface dangling bonds[110-112]. We propose to use an adapted version of these growth models used for a-Si/µc-Si mixed phase materials to explain the phase separation in our SiO_x layers.

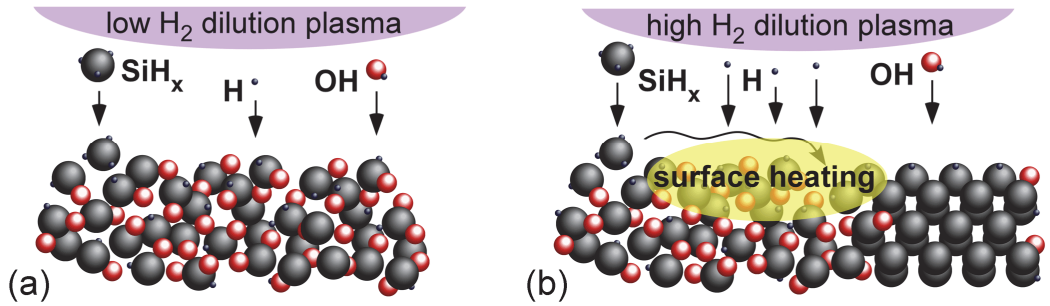

Figure 5-11: Surface diffusion model[110] with low adatom mobility in the case of low H_2 dilution leading to homogenous SiO_x material (a) and high adatom mobility due to surface heating and hydrogen passivation of surface dangling bonds in the case of high H_2 dilution leading to a Si/SiO_2 mixed-phase structure (b).

Figure 5-11 (a) illustrates the growth of a SiO_x layer deposited at low H_2 dilution, where all the silicon and oxygen species arriving from the plasma stick to the growing film and form a homogenous SiO_x material. The large amount of atomic hydrogen reaching the surface from the highly H_2 diluted plasma (illustrated in (b)) leads to an increase in adatom diffusion length through surface heating and passivation of surface dangling bonds. Furthermore atomic hydrogen can relax strained bonds and etch off loosely bound atoms. All of these reactions increase the chance that silicon atoms will find other coordinated silicon atoms resulting in the formation of silicon grains in SiO_x, a structure that was shown to be energetically favorable.[108]

It has to be noted here that in all of the SiO_x layers presented in this thesis report, increasing H_2 dilution always results in a lower deposition rate (by doubling the H_2 dilution, the deposition rate is roughly divided by two). This effect may also favor phase-separation, because it gives adatoms more time to reach energetically favorable places before being covered by other adatoms.

As the film thickens, it is energetically favorable for the silicon phase to occur by continued growth of the initially nucleated grains, rather than re-nucleation of new silicon grains. This produces the elongated silicon nanostructures which can only be formed during growth, unlike the previously observed isotropic silicon nanostructures produced by post-deposition high-temperature annealing.

5.5 Photoluminescence

The nanometer-sized dimensions of the silicon grains embedded in an oxygen-rich matrix, as observed by EFTEM in section5.3, lead to spatial confinement of excitons (electrons and holes in bound states). In our Si/$SiO_{y\sim2}$ mixed-phase layers, such quantum confinement is revealed by an upward shift of the silicon plasmon peak energy in EELS with decreasing silicon particle size. In crystalline silicon, the plasmon peak energy is 16.7 eV, and shifts to 17.2 and 17.8 eV for 5–8 nm and 3–4 nm wide silicon grains, respectively (see Figure 5-12). The silicon peak signal vanishes for the samples with silicon grains <2 nm, but a peak position at ~18.5 can still be guessed. A study of freestanding silicon nanoparticles quantified this effect and showed that a silicon plasmon peak position of 17.8 eV corresponds to silicon nanoparticles ~3 nm in diameter,[113] in good agreement with our film shown in (b).

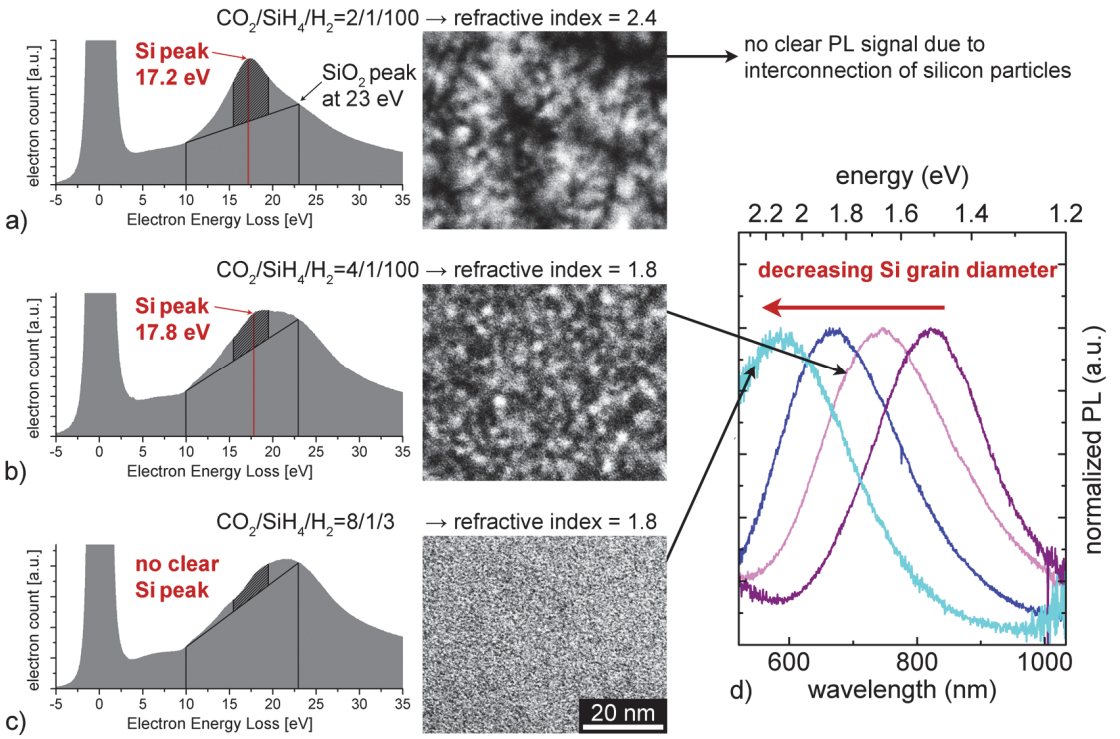

Figure 5-12: (a)-(c) Same EELS spectra and corresponding silicon maps as in Figure 5-6 from SiO_x plan-view samples showing the SiO_2-type plasmon peaks at ~23 eV and the fitted silicon plasmon peak, which shifts to higher energies with decreasing silicon particle sizes. (d) Normalized PL spectra of SiO_x samples with different silicon particle sizes. (PL measurements by Ivan Perez-Wurfl)

The presence of quantum confinement is further confirmed by the photoluminescence (PL) of the mixed-phase SiO_x films, with the PL peak position shifting to lower wavelengths for decreasing diameters of the silicon filaments (Figure 5-12 (d)). Different studies on silicon quantum dots embedded in SiO_2 showed that 2–3 nm silicon quantum dots give a PL peak position at ~750 nm and that 1 nm silicon quantum dots give a PL peak position at ~600 nm.[114] This is in agreement with the PL measurements for film (b) and gives evidence that there is also phase separation in film (c) which cannot be visualized with EFTEM because the grain size

is below the resolution limit of EFTEM making use of bulk plasmon absorption peaks. We observed the highest PL signal (visible with the naked eye on 300 nm thick layers) with un-doped SiO_x layers with interrupted or width-modulated silicon filaments as shown in Figure 5-7 (b). The PL peak position of this nanostructured layer is close to the one with long silicon filaments in Figure 5-7 (c), but the peak intensity is lower for the silicon filaments. This could be because quantum confinement in silicon dots is higher than in silicon filaments where at least in one dimension the confinement is relieved. Furthermore we observed that strong phosphorus doping is detrimental to the PL intensity, which is contrary to previous studies that report an increase in PL with phosphorus doping Si/SiO_2 mixed-phase films produced by high temperature annealing.[115,116]

The quantum confinement effects shown in this section are likely of no interest for Micromorph solar cells, but indicate the potential for mixed-phase SiO_x produced by PECVD to find application in third-generation photovoltaics[117], where silicon quantum dots are used to engineer the band gaps for all-silicon multi-junction devices with possibly higher conversion efficiencies. The spherical silicon quantum dots embedded in SiO_2 can provide the required band gap engineering, but current crowding due to difficult interconnection of spherical silicon particles, and material restrictions due to the high-temperature processes used to fabricate the quantum dots, have limited their success so far.[114,118] In contrast, the possibility of using PECVD to control the filament shape and size in combination with the ease of doping, may allow for quantum effect tuning and realization of electrical contacts with the same low-temperature process and could lead to a break-through for these novel approaches.

5.6 Conclusion

The large variety of analysis on the mixed-phase SiO_x layers presented in this chapter is definitely our most important contribution to materials science. With respect to applied research in thin-film silicon solar cells, it opens a new way to engineer material properties. Until now, we optimized only “homogeneous” layers with respect to the different requirements of the layer stacks forming the device. In the mixed-phase $Si/SiO_{y\sim2}$ structure we are now able to meet different requirements for a layer by using different phases of the material: We can maximize the oxygen content in the amorphous $SiO_{y\sim2}$ matrix to enhance transparency or lower the refractive index of the film, while we engineer the silicon filaments to be long, narrow, and highly doped, so as to keep sufficiently good transverse conductivity.

This new class of nanomaterials is fabricated by an inexpensive method, at low substrate temperatures and with a scalable process, which will ease the industrial implementation of these findings. We already completed a first step of up-scaling in our lab by transferring the results described here to a semi-industrial reactor, where we found similar results.

6 Different functionalities of SiO_x layers in thin-film silicon solar cells and high-efficiency Micromorph cells

In this chapter, we present different functionalities of p- and n-type SiO_x layers in µc-Si and Micromorph cells. As mentioned in the introduction to chapter 5, the first developments during my PhD thesis were aimed at optimizing SiO_x layers for use as intermediate reflecting layers in Micromorph cells, leading to the results summarized in section 6.1. In section 0 we present preliminary results on producing asymmetric intermediate reflecting layers with a smoothened morphology for better growth of the µc-Si bottom cell. Sections 6.3 and 0 show how optical and electrical cell parameters can be improved when using p-SiO_x layers instead of p-µc-Si in µc-Si cells and in section 0 we present results on electrical contacts and tunneling recombination junctions with p- and n-type SiO_x layers. Finally, in section 6.6 we show how the different functionalities have helped to improve Micromorph cell efficiencies over the last years.

Some of the results shown in this chapter were published in articles and patents. [2-6,8-11]

6.1 SiO_x intermediate reflecting layer (SOIR)

The individual cells composing a multi-junction cell are electrically connected in series and special care has therefore to be taken to match their currents. More precisely, the highest cell efficiencies are usually obtained when the short-circuit current density (J_{sc}) of the bottom cell is 0–1 mA/cm^2 lower than that of the top cell (see Appendix A for more details).[87] Current densities in the top and bottom cells can be influenced by adjusting the thickness of the thin absorber layers and through the insertion of an intermediate reflecting layer (IRL). The second solution is especially interesting for the Micromorph configuration where the top cell has to be kept reasonably thin (<250 nm) to mitigate the effects of light-induced Staebler-Wronski degradation of a-Si.[42] There are four main requirements for the IRL: First, the IRL should have a refractive index (n) as low as possible in order to maximize the reflection of light. Second, light that reaches the end of the a-Si top cell (wavelengths >500 nm) should not be absorbed by the IRL, and light that cannot be absorbed in the top cell (wavelengths >800 nm) should be transmitted to the bottom cell. Third, the IRL must have a transverse conductivity of at least 10^{-5} S/cm, in order to avoid blocking the device current. This conductivity limit corresponds to an increase in series resistance of 1 Ω·cm^2 for a 100 nm thick layer, which in a Micromorph cell operated at voltage over current density (V/J) ~ 100 Ω·cm^2 would cause a relative power loss

of 1%. And fourth, low in-plane conductivity is desired to avoid interconnection of spatially separated shunts in the sub-cells.

The first Micromorph cells with an IRL were presented in 1996 by Fischer et al.[119] using ZnO as a low-*n* material. In 2003, a different approach was introduced by Yamamoto et al.[120,121] without specifying the material used. But in a patent, the same authors from Kaneka Corporation demonstrated that it is possible to use a "composite" layer, "including silicon-rich phase parts in an amorphous alloy phase of silicon and oxygen," as an IRL in the Micromorph configuration.[122] The main advantage of SiO_x is that it can be deposited in the same deposition chambers with the same source gases as thin-film silicon solar cells. In industry this could mean higher through-put and lower equipment cost, both leading to a reduction of module production cost. We deposited the first phosphorous-doped n-type SiO_x layers in October 2006, and we published our first results of SOIRs in 2007 at almost the same time as the Jülich group.[2,123] Since then, several other groups have started developing SOIRs.[124-126] As an alternative to the SOIR, Delli Veneri et al.[127] showed that mixed-phase silicon nitride (SiN_x) deposited in similar regimes as our SiO_x can also be used as an IRL in Micromorph cells. However, a limit for the refractive index of mixed-phase SiN_x is given by the refractive index of stoichiometric, insulating Si_3N_4 which is 2. From this point, mixed-phase SiO_x seems more promising due to its lower limit at 1.5, given by stoichiometric SiO_2. Attempting to fabricate an IRL with spectral selectivity, Bielawny et al.[128] presented preliminary results on a more advanced 3D photonic crystal intermediate reflector, making use of an inverted-opal ZnO layer. However, growth of a µc-Si cell on such a layer has been challenging and the rather complicated fabrication process makes such approaches less relevant for industrial applications.

Figure 6-1 (a) shows EQE curves of Micromorph cells deposited on a rough front ZnO electrode (Z5-Ar20'). By increasing the SOIR thickness, the absorption of light is partially shifted from the bottom cell to the top cell for wavelengths between 500 nm and 800 nm. Light with wavelengths up to 500 nm does not reach the SOIR because it is completely absorbed in the front electrode and a-Si cell. The superposition of the EQE curves is therefore as expected and demonstrates that the top cell is not negatively affected by the deposition of the SOIR. Light with wavelengths above 500 nm is partially reflected due to refractive index changes at the a-Si/SOIR/µc-Si interfaces, increasing its chances of being absorbed in the a-Si cell. The increased absorption of light in the top cell reduces the intensity of light reaching the bottom cell. The smaller graph quantifies these optical effects with respect to their influence on the J_{sc} of the top and bottom cells. Also shown are the J_{sc} losses calculated from the increased reflectance measured on the cells and the total current loss, which is the sum of the J_{sc} changes in the top and bottom cells. The difference between the reflection losses and the total current losses is attributed to parasitic absorption losses which can be due to absorption of light in the SOIR as well as to increased parasitic absorption losses in other layers caused by an increased number of reflections of infrared light in the top cell before reaching the bottom cell.

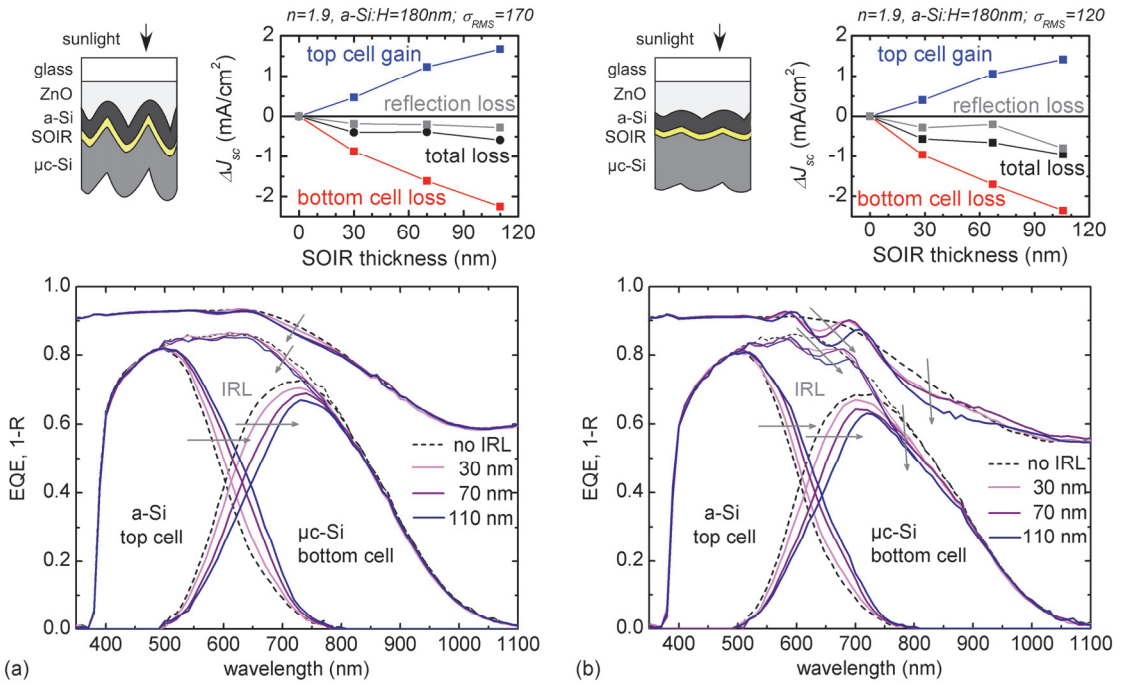

Figure 6-1: External quantum efficiency (EQE) and 1–reflectance (absorptance) of Micromorph cells (ZnO,180,SOIR,1.8) with 0, 30, 70, and 110 nm thick SOIRs deposited on (a) Z5-Ar20' and (b) Z5-Ar60'. The thinner lines connecting the a-Si top cell and µc-Si bottom cell EQE are the sum of the two sub-cells. The schematics illustrate the different front electrodes and cell roughnesses. The smaller graphs show the current variation in the top and bottom cell as a function of SOIR thickness. (Cells fabricated with D. Dominé)

Light that is reflected at the rough a-Si/SOIR/µc-Si interfaces is assumed to be highly diffuse (~Lambertian distribution of the scattering angles) which leads to strong light trapping in the silicon layers and keeps reflection losses small. At 650 nm, for example, the response of the a-Si cell nearly doubles from 21% to 41% when inserting a 110 nm thick SOIR, and the response of the µc-Si cell drops from 64% to 44%, indicating high reflectivity of the SOIR. The summed EQE for this wavelength is reduced by only 1% absolute indicating that the reflected light is mostly absorbed by the top cell and does not leave the cell by the front. At 850 nm, a similar reflectivity of the SOIR can be expected which should reduce the proportion of light that reaches the bottom cell directly. Nevertheless, it can be seen that the EQE curves are again superimposed from this wavelength on. This experimentally observed selectivity can be explained by strong light trapping of infrared light reflected at the SOIR, which can travel back and forth in the a-Si cell without being absorbed and finally still reach the bottom cell. An additional contribution to this light-trapping-induced selectivity of the SOIR could be that the longer wavelengths are reflected less by the thin IRL because they see the refractive index changes as less abrupt than smaller wavelengths (effective medium approximation over larger areas).[83]

Figure 6-1 (b) shows the same Micromorph cells deposited on a smoother front electrode (Z5-Ar60). On this substrate, light is not completely diffused at the ZnO/Si interface (see section 3.2), and part of the specular light in the top cell is again specularly reflected by the SOIR, creating interference fringes in the EQE and absorptance. The part of the light that is

specularly reflected at the SOIR is less likely to be trapped in the silicon layers and leaves the solar cell more easily, leading to increased reflection losses. The peaks of the interference fringes are slightly shifted to longer wavelengths with increasing SOIR thickness. This is because the location and amplitude of these fringes are determined at the ZnO/a-Si interface by the interference of incident light with light that is reflected at the a-Si/SOIR/µc-Si interfaces. In such an interferential IRL, a-Si and SOIR thicknesses should be optimized simultaneously in order to reduce reflection losses and to position the reflection peaks such as to minimize the current loss with the AM1.5 spectrum. We did not further investigate the potential of such interferential structures, because our goal here was to optimize Micromorph cells on rough front electrodes with high light-trapping capabilities, where no interference effects can be observed.

Figure 6-2 (a) shows *J-V* curves of top-limited Micromorph cells with 90 nm thick SOIR layers with different refractive indices. Three of those cells show a significantly increased series resistance (R_s), which is attributed to transverse conductivity of the corresponding SOIR of less than 10^{-5} S/cm. More precisely, from the *J-V* curves it can be calculated that the slope around the V_{oc} is 10 Ω·cm^2 for the Micromorph cell without a SOIR or with SOIRs that are sufficiently conductive. For the SOIRs produced with $CO_2/SiH_4/H_2$ of 3.5/1/100, 2.5/1/300, and 3.0/1/300, an additional R_s of 20, 30, and 550 Ω·cm^2 can be calculated which corresponds in these 90 nm thick layers to transverse conductivities of $5{\cdot}10^{-7}$, $3{\cdot}10^{-7}$, and $2{\cdot}10^{-8}$, respectively. The refractive indices of the different SOIRs used in this example are shown in (b) and the ones that resulted in an increase in R_s are marked with a black x. Figure 6-2 (c) shows the current gain in these top-limited Micromorph cells as a function of the refractive index of the SOIR.

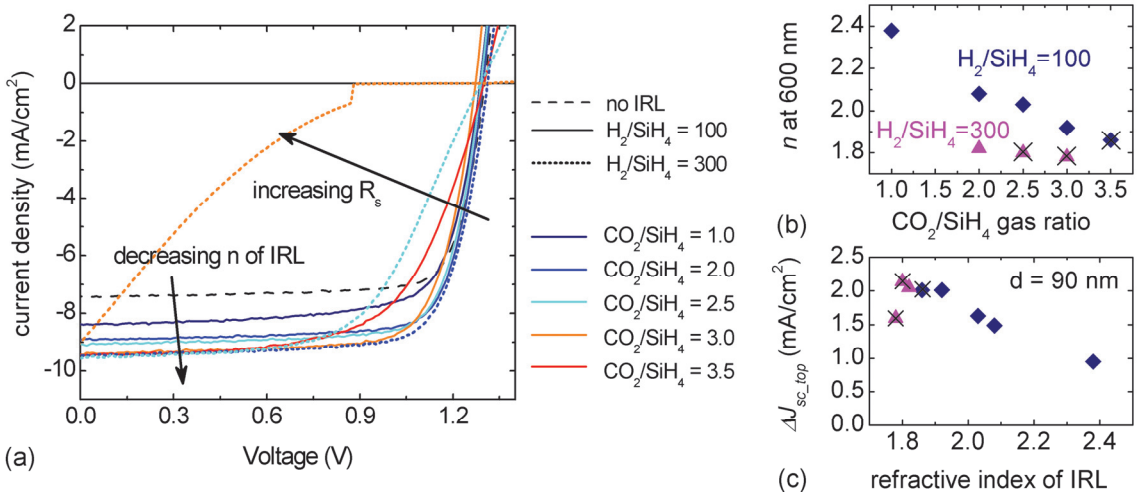

Figure 6-2: (a) *J-V* curves of top-limited Micromorph cells with a 90 nm thick SOIR, produced with different CO_2/SiH_4 and H_2/SiH_4 input gas ratios. (b) Refractive index of the SOIR layers used. The layers that show additional series resistance in the *J-V* curves are indicated by a black x. (c) Top cell current gain as a function of refractive index.

The lowest *n* achieved in this work for a 90 nm thick SOIR, without additional R_s in the Micromorph cell, was 1.8. As the R_s of the SOIR depends on the conductivity of the material and the thickness of the layer, it seems probable that for the same deposition parameters,

slightly lower *n* values could be achieved if thinner layers were used. Another point to mention with respect to the exact value of *n* is that the layer thickness that resulted from fitting ellipsometry data to a simple model with a Tauc-Lorentz dispersion relation, used to determine *n* (see section 2.2.2), was 5–20% below the thickness measured with the height profiler for the same layers. The origin of this difference was not clearly identified, but we speculate that the *n* values shown here are slightly overestimated, because in a more complete model, the fitted layer thickness should be closer to the thickness measured with the height profiler, thus resulting in a lower *n* for a constant product *n* x thickness. Similar to the work of Losurdo et al.[129] on a-Si/µc-Si mixed-phase materials, we developed a more advanced model making use of a three-phase material (SiO_x/nanocrystalline-Si/void) that gave encouraging results, but more work is needed in order to validate this approach.

6.2 Asymmetric SOIR

a-Si and µc-Si cells do not have the same requirements with respect to the surface morphology on which they grow. For a-Si cells the best efficiencies are achieved when deposited on sharp substrates with feature sizes similar to the a-Si film thickness, such as Z2. µc-Si cells are more sensitive and easily form zones of less ordered and porous material (also called cracks) when deposited on rough substrates.[62,63] These cracks show a bad-diode behavior and reduce the electrical performance of the solar cells.[64,65,67] Smoothening of as-grown rough ZnO is therefore necessary to obtain µc-Si cells with reasonable electrical parameters (V_{oc} x *FF* > 0.35 V) and best cell results are achieved on substrates such as Z5-Ar20' and Z5-Ar60'. In a Micromorph cell, the a-Si and µc-Si cells are stacked on top of each other and therefore a compromise has to be made when choosing the front ZnO morphology. From this point of view, it is desirable to match the front ZnO morphology to the requirements of the a-Si cell and then adapt the IRL so as to provide a surface morphology suited for the growth of high-quality µc-Si cells.

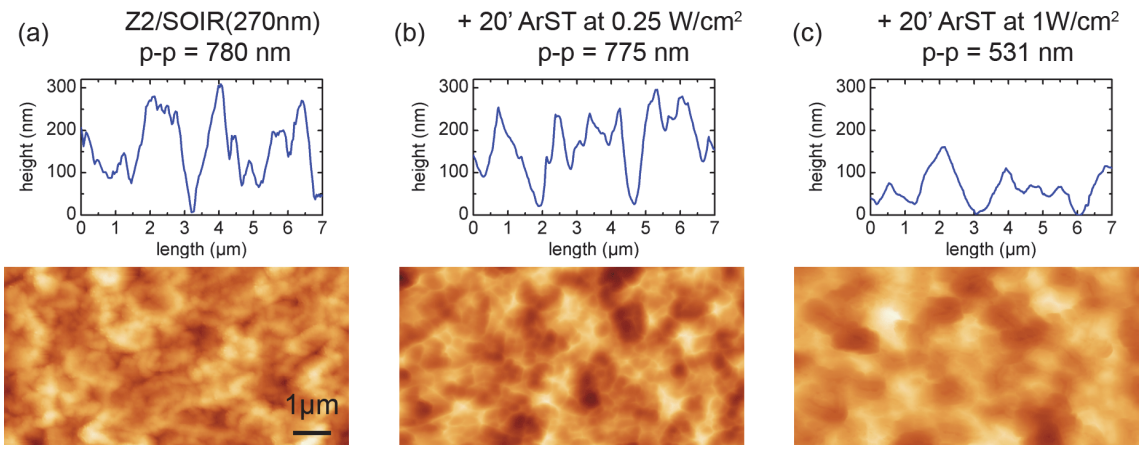

Figure 6-3: AFM images and representative profiles from three different surfaces: (a) Z2 covered with 270 nm thick SOIR; (b) same Z2/SOIR sample after 20' ArST in a reactive ion etching system at 50 W; and (c) the same Z2/SOIR sample after 20' ArST at 200 W. The peak-to-peak values from the 10 µm x 10 µm surfaces are also given.

Figure 6-3 (a) shows the surface of a Z2 electrode covered with a 270 nm SOIR and (b) and (c) show the same surface after 20' argon surface treatment (ArST) in a reactive ion etching system with an argon pressure of 100 mTorr and power density of 0.25 and 1 W/cm^2, respectively. The surfaces could clearly be smoothened with these ArSTs and U-shaped morphologies were observed after treatment, making these modified SOIRs promising for the growth of high-quality µc-Si with a reduced number of cracks. We tested various ArSTs on SOIRs in Micromorph cells, but unfortunately all the *J-V* curves of Micromorph cells with SOIRs with ArST showed high series resistance. These observations were confirmed by simpler ZnO/n-µc-Si/SOIR/n-µc-Si/ZnO stacks with sufficient transverse conductivity, but which turned blocking when an ArST was applied to the SOIR before deposition of the n-µc-Si layer. Although this can be surprising at first, it seems probable that the highly energetic Ar^+ ions hitting the surface destroy the fine nano-structure in the SOIR (see section 5.3), which is necessary to

provide the required transverse conductivity in such films. Even though this argon plasma treatment is demonstrated to efficiently smoothen the IRL surface, we concluded that it cannot be used in Micromorph cells as it completely blocks the current in the device.

A different way to flatten the SOIR surface morphology is by chemical mechanical polishing (CMP, see section 2.6). Figure 6-4 shows the *J-V* and EQE curves of two Micromorph cells, one with standard configuration and one with a CMP step after deposition of the SOIR. Micromorph cells are designed to be strongly bottom limited so as to make the *FF* of the bottom cell dominate the Micromorphs' *J-V* curves (see Appendix A). The slight change in current mismatch here does not significantly influence the *FF* of the Micromorph cell and the strong increase in *FF* in combination with a slight V_{oc} increase is therefore attributed to an improvement of the µc-Si cell parameters because of the flat substrate used for its growth. Electrically this configuration seems promising, but looking at the EQE, a significant current loss can be observed for the µc-Si bottom cell deposited on a polished SOIR. This loss is attributed to significantly lower light trapping in the µc-Si cell with flat SOIR/µc-Si/ZnO interfaces.

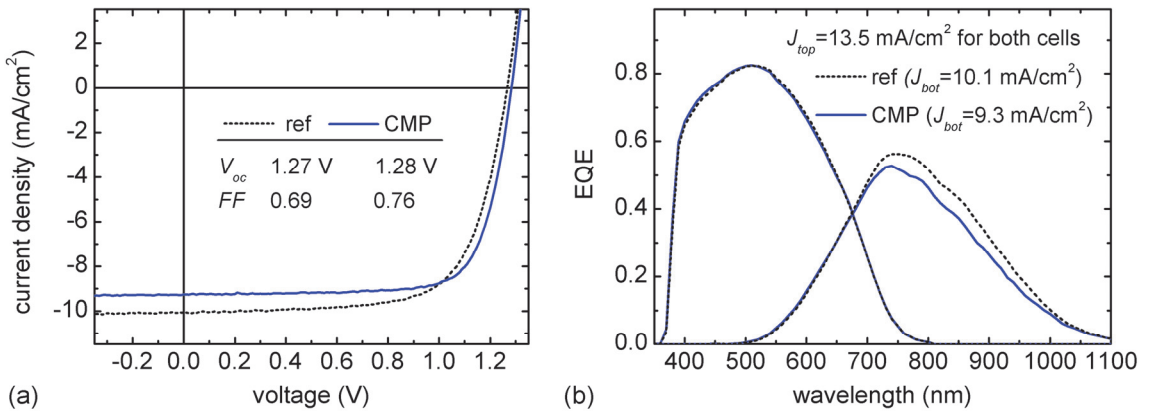

Figure 6-4: *J-V* and EQE curves of two Micromorph cells (Z2-Ar1'/180/220/2.8) with and without CMP of the SOIR.

On the one hand, physical plasma etching provides the smooth U-shaped morphologies on which µc-Si cells perform best, but it leads to resistive SOIR layers, probably due to damage of the fragile nanostructure of the SiO_x layers. On the other hand, with CMP no additional series resistance is created and a gain in the cells' electrical performance is clearly demonstrated. However, the flat interfaces of the µc-Si cell significantly reduce J_{sc} due to less light trapping. Unfortunately, the expected breakthrough with asymmetric SOIRs was not achieved in this work, but the preliminary results show that it is possible to smoothen the SOIR and thereby improve the electrical performance of the µc-Si cell. After these experiments, we imagine an ideal device structure with an as-grown rough LP-CVD ZnO (Z2–Z5) as the substrate for deposition of the a-Si cell, and a smooth but not flat SOIR surface that reduces the formation of cracks in the µc-Si cell but still allows for light scattering of wavelengths >600 nm. Soft chemical plasma etching using a gas mixture of argon and nitrogen trifluoride might be a way to produce a smooth surface without causing physical damage to the layer.

6.3 p-nc-$SiO_{0.5}$ window layer in µc-Si cells

In this section, we present results on the use of p-type $SiO_{x\sim0.5}$ comprising a nanocrystalline silicon phase (p-nc-$SiO_{0.5}$) as a window layer in µc-Si solar cells and in section 0 we discuss the effect of the p-nc-$SiO_{0.5}$ layer on the electrical performance of the cell. The p-µc-Si and p-nc-$SiO_{0.5}$ layers compared in these two sections are deposited at 1 A/s and have the same thickness of ~20 nm if deposited on glass. In the cell, they are deposited directly onto the front ZnO layer without any grading or buffer layer. The p-nc-$SiO_{0.5}$ layers are deposited with H_2/SiH_4 = 100, TMB = 5‰ and CO_2 = 0.7; both the higher TMB and CO_2 lead to additional series resistance as calculated from the *J-V* measurements of the cells (see section 5.1 for more details on the SiO_x layers). At a wavelength of 400 nm, the absorption coefficients of the p-µc-Si and p-nc-$SiO_{0.5}$ layers are $2.4\cdot10^5$ cm^{-1} and $1.1\cdot10^5$ cm^{-1}, respectively, as determined from spectroscopic ellipsometry measurements (see section 2.2.2). This enhanced transparency leads to a significant increase in µc-Si cell EQE for the short wavelengths as shown in Figure 6-5. By comparing the different substrates, it can be seen that the EQE curves are higher on the rougher front electrodes. This effect is most probably due to the reduced effective p-layer thickness on the rougher substrates, where the same amount of material is distributed on a larger ironed surface. However, the gain in EQE with the p-nc-$SiO_{0.5}$ is similar on all of the different front electrodes used in this study. From the absorptance (1–R) measurements it can be seen that the anti-reflection effect (see section 4.3) of the p-nc-$SiO_{0.5}$ layer is significant only on the polished sample. The gain in EQE due to enhanced transparency is important for the single-junction configuration and will be less pronounced but not negligible in Micromorph cells, where only light with wavelengths >500 nm reaches the µc-Si cell.

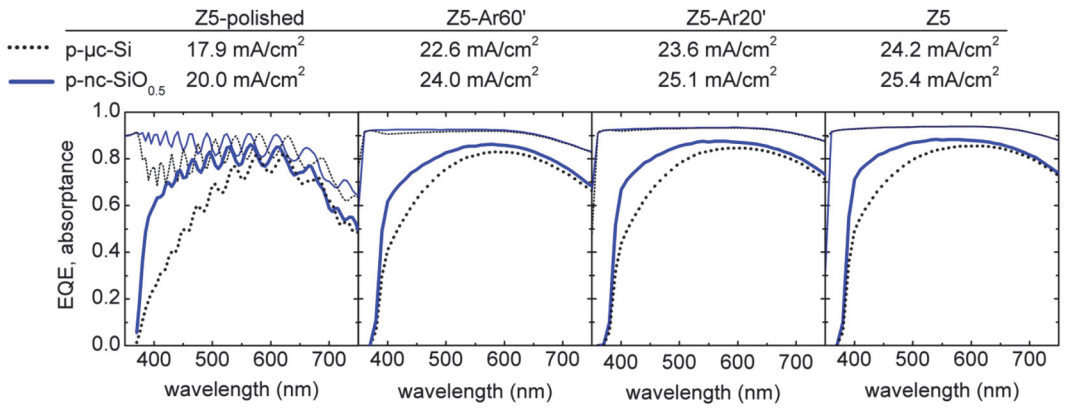

Figure 6-5: EQE and absorptance of 1.8 µm thick µc-Si cells with p-µc-Si and p-nc-$SiO_{0.5}$ layers deposited on different front electrodes. The J_{sc} values are indicated in the table.

6.4 Shunt-quenching effect of p-nc-$SiO_{0.5}$ layer in µc-Si cells

Figure 6-6 (a) shows the *J-V* curves of µc-Si cells with standard p-µc-Si and p-nc-$SiO_{0.5}$ layers (see section 6.3 for details on the deposition parameters). On the U-shaped Z5-Ar60', a good value of 0.36 V can be achieved for the product V_{oc} x *FF* and no significant difference can be observed when using p-µc-Si or p-nc-$SiO_{0.5}$ layers. However, on an untreated V-shaped Z5, the V_{oc} x *FF* product is only 0.27 V with the p-µc-Si and 0.30 V with the p-nc-$SiO_{0.5}$ layers. The low performance of µc-Si cells on V-shaped substrates is due to the formation of cracks in the µc-Si absorber layer that electrically behave as bad diodes and reduce the cell performance.[64,65] The effect of the p-layer and the substrate on the V_{oc} of µc-Si is also illustrated in Figure 6-6 (b). The lowest V_{oc} is obtained on V-shaped Z5, the V_{oc} increases on Z2 and Z5-Ar20', and the highest V_{oc} is obtained on U-shaped Z5-Ar60'. From the roughness values of the front electrode given below the graph, it can be clearly seen that the V_{oc} of µc-Si cells depends on the inclination angles of the front electrode surface (expressed by the most common inclination angle (α_{max})) and does not correlate with the size of the ZnO pyramids (expressed by the RMS roughness of the surface (R_{RMS})). The decrease of the V_{oc} with increasing sharpness of the front electrode shows the same tendencies when using p-µc-Si and p-nc-$SiO_{0.5}$ layers, but the decrease is significantly reduced when using the latter.

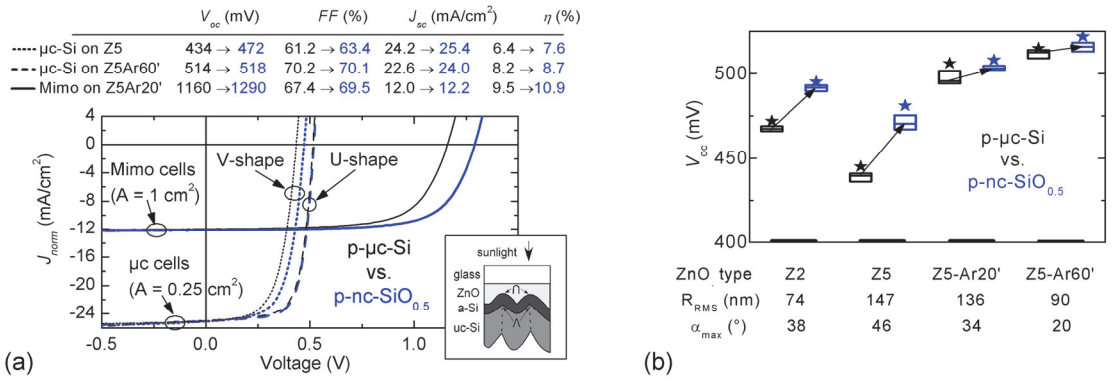

Figure 6-6: (a) *J-V* curves of different cells with p-µc-Si (black) and p-nc-$SiO_{0.5}$ (blue) layers. The *J-V* curves of the µc-Si cells are normalized to 25 mA/cm² for better comparison of the electrical characteristics. (b) V_{oc} of 1.8 µm thick µc-Si cells with p-µc-Si and p-nc-$SiO_{0.5}$ layers deposited on different front electrodes. The Boxplots show the best values (star), quartile, and median values (horizontal lines) of 16 cells for each sample.

The beneficial effect of p-SiO_x on the V_{oc} of µc-Si cells was previously reported by other groups and explained by the band offset at the p-SiO_x/i-µc-Si hetero-junction interface resulting in reduced recombination losses.[130-132] In our case, the optical gap of p-nc-$SiO_{0.5}$ is higher than that of p-µc-Si, which could indicate a higher mobility gap. However, the SiO_x in our case is not a homogeneous, but a mixed-phase material as illustrated by the plan-view EFTEM image of a 70 nm thick n-type $SiO_{x\sim0.5}$ film shown in Figure 6-7 (see section 5.3 for more details). We do not expect doping to change the phase separation of the film, but increasing film thickness probably leads to larger silicon clusters. We therefore expect the 20 nm thick p-nc-$SiO_{0.5}$ to

contain 2–5 nm large silicon grains, smaller than what is shown in the EFTEM image of the 70 nm thick film.

On the one hand, we expect that the mixed-phase structure of the film with 2–5 nm large silicon grains cancels the band offset at the p/i interface expected for a homogeneous p-SiO_x material and on the other hand, we showed that the gain in V_{oc} is dependent on front electrode roughness and disappears for cells deposited on smooth Z5-Ar60'. From these observations, we conclude that the gain in V_{oc} in our cells is not due to a general band offset at the p/i interface, as proposed in previous studies with p-SiO_x layers, but instead due to an effect that reduces the influence of spatial non-uniformities or so-called cracks on the electrical performances of the device. This can be achieved by adding a distributed resistance in series with the spatially non-uniform device, as demonstrated by Rau et al.[133,134] using a resistive ZnO layer to quench shunts in CIGS cells. For thin-film silicon solar cells, Despeisse et al.[20] demonstrated such a shunt-quenching effect, using n-type SiO_x at the back of a-Si cells, leading to a significant increase in device performance on rough front electrodes.

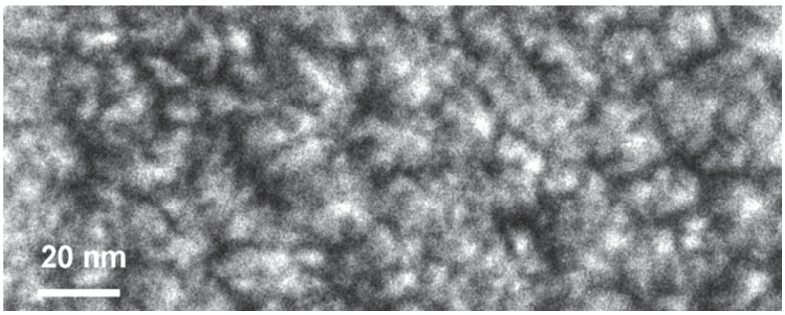

Figure 6-7: EFTEM plan-view map of the silicon phase (white) in a 70 nm thick SiO_x layer produced with $CO_2/SiH_4/H_2$ = 1/1/100.

For µc-Si cells, we know from previous studies by Python et al.[64-66] that as-grown rough ZnO electrodes lead to the formation of cracks in µc-Si absorber layers which electrically behave as localized bad diodes and so reduce the V_{oc} of the device. Figure 6-8 (a) shows a diode array model that can be used to describe such µc-Si solar cells with locally inhomogeneous diode behaviors. Good diodes (J_{01}) represent, in this illustration, the dense µc-Si material and bad diodes ($J_{02} >> J_{01}$) represent the cracks, located above the sharpest valleys of the ZnO electrodes. In solar cell devices, these regions with different electrical behaviors are connected in parallel by the front and back electrode layers. If a device is illuminated and operated in V_{oc} conditions (no current comes out of the cell), then the good-diode regions are operated below local V_{oc} conditions and generate current that is consumed in bad-diode regions (current circulates within the device).

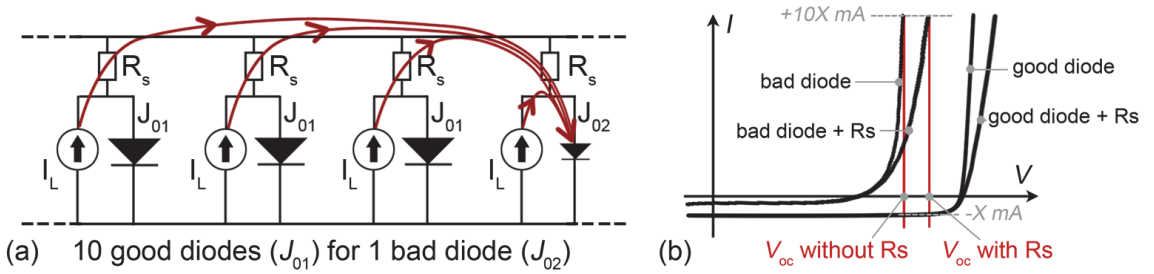

Figure 6-8: (a) Diode array model for a µc-Si solar cell with dense material (good diode: J_{01}) and cracks located above the valleys of the front electrode (bad diode: J_{02}). (b) *I-V* curves of good diodes and bad diodes with and without an additional resistance in series (R_s). The red lines indicate the V_{oc} with and without R_s, if the good diode regions are 10 times larger than the bad diode region.

Figure 6-8 (b) shows *I-V* curves of good and bad diodes with and without R_s. If the surface with good-diode behavior is ten times larger than the surface with bad-diode behavior, then this device has a V_{oc} operating point as indicated by the red line, where "one" bad diode is compensated by "ten" good diodes. If a resistance is added in series with this device, then this does not necessarily affect the operation of the good diode below local V_{oc} but it can increase the voltage drop on the bad diode operating above its local V_{oc} and so increase the overall V_{oc} of the device. As we maximize the oxygen content in the p-nc-$SiO_{0.5}$ layer to just below the limit where the series resistance becomes visible in the *J-V* curves, it has an optimized resistance to limit current drains without negatively affecting the *FF*. Furthermore, we know from SiO_x material studies (section 5.3) that SiO_x has a less-ordered structure in the valleys of the substrate (see Figure 5-9), which could lead to locally increased resistance of the p-nc-$SiO_{0.5}$ layer exactly where the shunts are located and so enhance shunt quenching in a favorable way.

The shunt-quenching effect seems at this point the most probable explanations, but other possibilities should not yet completely be discarded. p-nc-$SiO_{0.5}$ has a lower Raman crystallinity and a different chemical composition than p-µc-Si, which could lead to a change in the nucleation of the i-µc-Si layer and so change the V_{oc}. This possibility could not be demonstrated, nor excluded: We measured ~59% Raman crystalline fractions for cells with both µc-Si and nc-$SiO_{0.5}$ p-layers on Z5-Ar60', and a Raman crystalline fraction of ~55 % was measured for cells deposited on Z5. These measurements were performed with a red laser from the back of the cells and give information on the average nanostructure of the entire cell. To get information about the nucleation of the i-µc-Si layer, it is possible to measure the Raman crystalline fraction with a green laser from the glass side. However, in this measurement the p-layer also significantly contributes to the result which makes it difficult to extract information about the nucleation of the i-µc-Si absorber. We also performed TEM analysis in order to observe nucleation at the p/i interface. Although we could not see a difference in the nucleation of the i-layer, with this technique we cannot exclude it due to a limited resolution of the images and the three-dimensional roughness of the p/i interface, which makes its observation difficult. Another effect that could influence the V_{oc} is contamination of the p/i interface by boron, oxygen, or water vapor. With respect to this

possibility, the amorphous silicon oxide in p-nc-$SiO_{0.5}$ could have a beneficial effect either by better retaining impurities from the p-layer itself or by hindering the diffusion of impurities from the underlying ZnO into the i-layer during the deposition of the i-µc-Si layer with a hydrogen-rich plasma, or after deposition due to thermal agitation.

The influence of single layers on cell performance is easier to study in the single-junction configuration. However, it is then important to transfer the findings to the final configuration which in our case is the Micromorph cell. Figure 6-6 (a) shows two Micromorph cells deposited on Z5-Ar20' substrates in continuous vacuum (without air exposure between the depositions of the top and bottom cells). The a-Si cell has a V_{oc} of ~0.9 V on Z5-Ar20' and the µc-Si bottom cell is deposited with the same process conditions as the single-junction cells presented in Figure 6-6 (b) (500 mV on Z5-Ar20'); a relatively high V_{oc} value of ~1.36 V is therefore expected for the Micromorph configuration. However, only 1.16 V is achieved with standard p-µc-Si and 1.29 V with p-nc-$SiO_{0.5}$. We explain the low V_{oc} with the p-µc-Si layer as being due to sharper valleys after deposition of the a-Si top cell and the IRL, which deteriorate the performance of the µc-Si bottom cell. This effect is illustrated by the schematic in Figure 6-6 (a) and is studied in greater detail in section 3.3.

It has to be noted that Micromorph cells with the standard p-µc-Si layer shows similar performance to Micromorph cells with p-nc-$SiO_{0.5}$ when an air exposure of ~10' made after the deposition of the a-Si top cell, which finishes with an n-µc-Si layer. We speculate that the oxidation of the n-µc-Si material could have a beneficial shunt-quenching effect similar to the deposition of p-nc-$SiO_{0.5}$. However, more studies are necessary to gain a better understanding of the role of p-nc-$SiO_{0.5}$ in the bottom cell of a Micromorph configuration. Towards this, we study in section 0 the characteristics of tunneling recombination junctions making use of SiO_x layers.

6.5 Tunneling recombination junction and contact resistance

When doped SiO_x layers are used as the first or last layer of the silicon stack composing a solar cell, it has to be investigated whether these layers make good electrical contact with the ZnO front and back electrodes. In the Micromorph tandem configuration, it is additionally of interest how doped SiO_x layers can be used at the tunneling recombination junction (TRJ). These ZnO-contact and TRJ characteristics can be probed in the solar cell configuration, by correct interpretation of the *I-V* curves. However, it is simpler and faster to deposit ZnO/Si/ZnO layer stacks, whose *J-V* characteristics are more straight forward to interpret. In this section we show contact and TRJ characteristics of p- and n-type µc-Si and nc-$SiO_{0.5}$ layers, measured on layer stacks with a surface of 0.25 cm^2 (with the same patterning and *I-V* measurement procedures as we use for single-junction solar cells). The ZnO-contact and TRJ resistances are measured in the transverse direction and normalized with the stack area, and the values are given in $\Omega \cdot cm^2$, which are the units commonly used for series resistances (R_s). The current is here laterally extracted by the ZnO layers, which gives in this configuration a resistive contribution of ~ 2.8 Ω, which corresponds to a value of 0.7 $\Omega \cdot cm^2$ for stack with an area of 0.25 cm^2, and which sets the lower limit for the measureable ZnO-contact or TRJ resistance. Nevertheless, it is possible with this configuration to rapidly test different silicon layers and determine if they cause a series resistance higher than 1 $\Omega \cdot cm^2$, corresponding to relative power loss of 1% in a Micromorph cell, operated at V/J ~100 $\Omega \cdot cm^2$. The µc-Si layers investigated in this section are produced with H_2/SiH_4 = 60 and TMB/SiH_4 or PH_3/SiH_4 = 0.4‰, and the nc-$SiO_{0.5}$ layers with H_2/SiH_4 = 120, CO_2/SiH_4 = 0.7 and TMB/SiH_4 or PH_3/SiH_4 = 0.4‰, similar to the layers presented in Figure 5-1.

In order to measure the contact resistance between the ZnO and the n-type layers we fabricated ZnO/n-layer-1/n-layer-2/ZnO stacks with the four possible combinations with n-µc-Si and n-nc-$SiO_{0.5}$. The *I-V* curves of the stacks (not shown here) revealed that both n-µc-Si and n-SiO_x make good contact with the ZnO layer on which they are deposited, but that only the n-µc-Si layer makes a good contact with the back ZnO layer which is deposited on top of the silicon layers. The same results are obtained for stacks with p-type µc-Si and nc-$SiO_{0.5}$ layers. It has to be noted that the p-µc-Si layers used here are different from the standard p-µc-Si layers used in p-i-n µc-Si cells, which make a good contact at the front-ZnO/p interface, but lead to series resistance at the p/back-ZnO interface. The developments undertaken to reduce this contact resistance are summarized in Figure 6-9 (a), showing the R_s of ZnO/p-µc-Si/ZnO stacks with p-layers produced with different H_2/SiH_4 gas ratios and deposition times. It was shown previously that a high Raman crystalline fraction is necessary to make a good p/ZnO contact[38] and that the crystallinity increases with increasing H_2/SiH_4 source gas ratios and increasing film thickness. However, in our case, the lowest R_s of the ZnO/p-µc-Si/ZnO stacks is achieved with the lowest H_2/SiH_4 source gas ratios of 60 and is not dependent on the film thickness varying from 30–360 nm (deposition rate = 2 A/s for films deposited with H_2/SiH_4 = 60 and 1 A/s for films deposited with H_2/SiH_4 = 120).

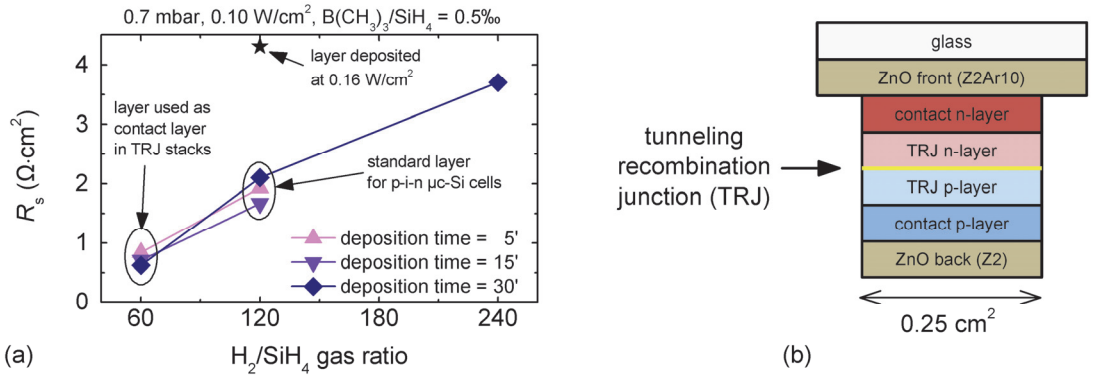

Figure 6-9: (a) R_s measured on Z2/p-µc-Si/Z2 stacks with p-µc-Si layers fabricated with different H_2/SiH_4 gas ratios and different deposition times. (The fabrication and measurements of the stacks were carried out by Michael Marending during an internship at IMT.) (b) Schematic of the layer stacks used to measure the tunneling recombination junction (TRJ).

The n-µc-Si layer makes good contact with the front ZnO, and the p-µc-Si layer deposited with H_2/SiH_4 = 60 makes good contact with the back ZnO. Therefore, we used these layers as contact layers in the stacks to test the TRJ illustrated by the schematic in Figure 6-9 (b). With ZnO/n-µc-Si/n-TRJ/p-TRJ/p-µc-Si/ZnO layer stacks it is possible to probe the TRJ characteristics of different materials by changing the n-TRJ and p-TRJ layers.

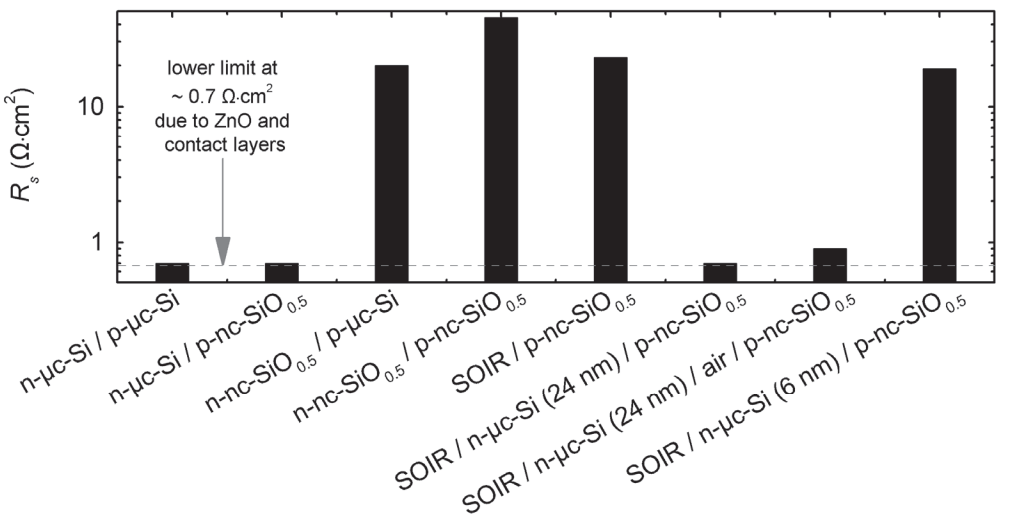

Figure 6-10: R_s measured on different p/n TRJ. The p/n TRJ is embedded in a ZnO/n-µc-Si/TRJ/p-µc-Si/ZnO stack in order to contact the TRJ, but gives a resistive contribution of 0.7 Ω·cm² below which the R_s of the TRJ cannot be measured. (The fabrication and measurements of the stacks were carried out by Michael Marending during an internship at IMT.)

Figure 6-10 shows that the R_s measured on n-µc-Si/p-µc-Si and n-µc-Si/p-nc-$SiO_{0.5}$ junctions is 0.7 Ω·cm², which corresponds to the contribution of the ZnO layers and the resistance for these TRJs must therefore be lower. In order to reproduce the exact configuration used in Micromorph cells, we also show that adding a 100 nm thick SOIR between the n-contact layer and the n-µc-Si TRJ layer does not change this result. The a-Si top cell and the µc-Si bottom cell are often deposited in different systems and air exposure is unavoidable for such cells. Such air

expsure of ~10 minutes at the n-µc-Si/air/p-nc-$SiO_{0.5}$ junction increases the R_s by 0.3 Ω·cm^2, which is expected to result in an acceptable relative efficiency loss of 0.3%. This observation about a moderate increase in R_s with the air exposure strengthens the discussion in section 0, where we speculated that oxidation of the n-µc-Si layer at the TRJ can have a shunt-quenching effect. In a Micromorph cell with a SOIR (n-$SiO_{x\sim1}$), a sufficient n-µc-Si layer thickness covering the SOIR is necessary to obtain a good TRJ, as demonstrated by high R_s measured on SOIR/p-nc-$SiO_{0.5}$ and SOIR/n-µc-Si(6nm)/p-nc-$SiO_{0.5}$ stacks. Compared to the SOIR, the n-nc-$SiO_{0.5}$ layers has lower oxygen content, but also lower dopant content and leads to a similar R_s at the TRJ as the SOIR.

In summary, both p- and n-type nc-$SiO_{0.5}$ make good electrical contact with the ZnO on which they are deposited, but not with the ZnO which is deposited on top of the nc-$SiO_{0.5}$ layers. This asymmetry is not clearly understood, but it is speculated that a lower carrier concentration and mobility in the ZnO nucleation layer could change the band alignment in an unfavorable way and so cause the appearance of contact resistance. For the TRJ, we showed that low R_s is achieved whenever a sufficiently thick (>10nm) n-µc-Si layer is used and that all n-SiO_x layers used in these experiments led to an increase in R_s. For the p-layer, however, no difference is observed between µc-Si and nc-$SiO_{0.5}$. The measurements on ZnO-contact and TRJ stacks are consistent with many experiments performed on µc-Si and Micromorph cells. The cell results are not shown here because the cell's R_s are more difficult to compare because they depend on many other parameters, such as electrode resistances, cell quality, and current matching.

6.6 High-efficiency Micromorph devices

In Figure 6-11, we summarize different functionalities of SiO_x that have helped to continuously increase Micromorph cell efficiencies in recent years. The SEM cross-section image of a 1.4 µm thick Micromorph cell shows a typical device structure with LP-CVD ZnO electrodes, and the locations of the newly developed p- and n-type SiO_x layers are illustrated in the first zoom (x 2.5). The enhanced transparency of doped SiO_x compared to the commonly used doped µc-Si layers reduces parasitic absorption losses and the low refractive index SiO_x between the cells leads to the reflection of light back into the a-Si top cell. The influence of these optical effects on the J_{sc} is illustrated by comparing the EQE of a cell with doped µc-Si layers and a cell with doped SiO_x layers. A second zoom (x 10, not from the same sample) shows an EFTEM image revealing the filamentous nanostructure in SiO_x. The silicon filaments provide doped SiO_x films with sufficient transverse conductivity, whereas the optical properties are given by the $SiO_{y\sim2}$ matrix. The shunt-quenching effect of SiO_x is achieved by tuning the silicon phase to achieve the desired transverse conductivity.

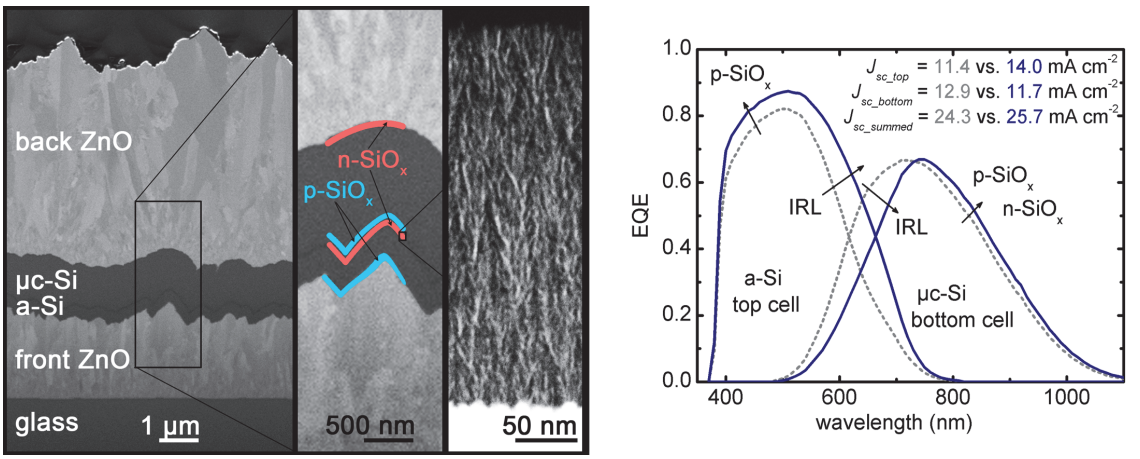

Figure 6-11: (Left) SEM cross-section image of a Micromorph cell (light enters the cell through the glass) with a first zoom (x 2.5) indicating the location of SiO_x layers and a second zoom (x 10, EFTEM image not from the same sample) showing silicon filaments (white) in a $SiO_{y\sim2}$ matrix (black). (Right) EQE curves of Micromorph cells with standard doped µc-Si layers (dotted grey) and doped SiO_x layers (solid blue). The arrows indicate the influence of the SiO_x layers and the J_{sc} calculated from the EQE curves are given.

The realization of state-of-the-art devices is an important step in validating new materials and configurations for thin-film silicon solar cells. Figure 6-12 shows the evolution of Micromorph cell initial efficiencies in our lab over the last 4 years. Our starting point is a Micromorph cell with a sputtered ZnO intermediate reflector at 11.8% initial efficiency developed by D. Dominé and J. Bailat.[135] With the introduction of the SOIR, and a smoother front electrode, cell efficiency improved to 12.6%.[10] We attribute the increase in V_{oc} and *FF* mostly to a more homogenous absorber layer due to a longer ArST, and to shunt-quenching properties of the SOIR. The next increase in efficiency was achieved with thicker absorber layers and the use of glass substrates with an anti-reflection coating (ARC) on the air/glass interface, provided by Schott Guinchard in Yverdon, CH.

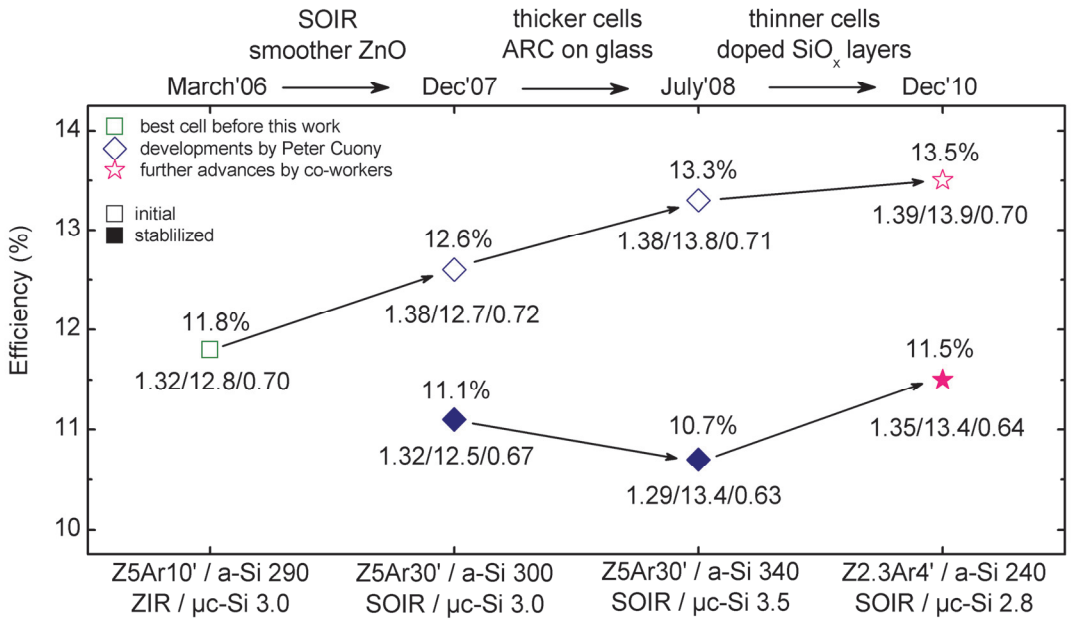

Figure 6-12: Best Micromorph cells at IMT over the timespan of this thesis report. The empty symbols indicate the initial efficiencies and the full symbols indicate the stabilized efficiencies after 1000 hours of light soaking. The cell efficiency is given above each symbol and the values below indicate V_{oc}(V)/J_{sc}(mA·cm^{-2})/*FF*().

The improvements in initial efficiency to 12.6% and 13.3% were achieved by optimizing and fine-tuning the SOIR, front electrode morphology, deposition procedures, and current matching, carried out by A. Billet, D. Dominé, and P. Cuony in PECVD reactor sysB. Device optimization in this small-scale system is time consuming as all the process steps are executed manually (the fabrication of one Micromorph cell takes about 10 hours). With the introduction of the automated KAI reactors, device optimization was therefore shifted towards these systems, and in 2010, an initial efficiency of 13.5% was reached with a Micromorph cell with a total silicon layer thickness of 3.1 µm. With a stabilized efficiency of 11.5%,[25] this work, acheived with direct contributions of M. Boccard, G. Bugnon, T. Söderström, and M. Despeisse resulted in a new lab record. The higher current density for thinner silicon absorber layers is mostly due to lower parasitic absorption losses, achieved with the introduction of doped SiO_x and improved ZnO layers. Although the initial efficiency of this cell is only slightly higher than the best cell from sysB, it results in a significantly better stabilized efficiency due to lower degradation. The increased stability is partially due to thinner absorber layers, mitigating the effect of Staebler-Wronski degradation.[42] However, as the V_{oc} is the parameter that mainly differentiates these two cells, we conclude that the improved stability of the 13.5% cell is due to the use of a front electrode with smaller ZnO pyramids, which reduces the impact of H_2O-induced degradation on the cell performance (see chapter 7). Thinner cells degrade less and are preferred from the industrial point of view because higher throughputs can be achieved. With developments in this direction, we achieved an initial efficiency of 12.7 % with a total silicon layer thickness of only 1.4 µm (cell shown in Figure 6-11) which resulted in a stabilized efficiency of 11.3%.[24] This cell implements p- and n-SiO_x layers in both sub-cells and was achieved with direct contributions from M. Charrière, A. Billet, M. Despeisse, M. Boccard, G.

Bugnon and S. Hänni. With respect to future increases in efficiency, we think that a better understanding of the different degradation mechanisms is necessary to mitigate their influence, which would allow one to take advantage of thicker cells on rougher substrates.

It can be noted that the presented cells are achieved after ~5–10 Micromorph deposition runs and are not fully optimized due to the limited workforce for Micromorph device optimization available in our research group. With better device optimization, higher efficiencies can be reached as recently demonstrated by Bailat et al.[59] who hold the current Micromorph world record[136] for a 1 cm^2 cell with a stabilized efficiency of 11.9 %.

6.7 Conclusion

By tuning the composition, the phase separation, and the doping of filamentous SiO_x, a large range of electrical and optical properties can be engineered, which can serve in different ways in thin-film silicon solar cells. The transparency of p-SiO_x makes it a good window layer on the front of the cell, while n-SiO_x with a low refractive index and sufficient transverse conductivity has established itself in different research groups as the preferred material for use as an IRL. The beneficial role of the p-SiO_x to the V_{oc} is not completely clarified at this point, but the shunt-quenching of doped SiO_x layers is definitely an advantage that can partially make up for the presence of shunts or bad diodes in the device. Furthermore, we showed that p-SiO_x layers make good electrical contact when deposited onto front LP-CVD ZnO layers and forms a good TRJ when deposited onto n-µc-Si.

The different functionalities of SiO_x layers were all demonstrated in small-scale system SysB, but most of the results were successfully transferred to the larger KaiS and KaiM reactors, where the same trends were observed. The results with SiO_x layers are of high industrial relevance as the processes are scalable and can be easily implemented in any thin-film silicon reactor with CO_2 available as a precursor gas.

No final breakthroughs were achieved in this work with the asymmetric (or non-conformal, or smoothened, or morphology adjusting) SOIR, which decouples the growth morphologies for the a-Si and µc-Si cells in the Micromorph configuration. But chemical plasma etching with nitrogen trifluoride or silicon tetrafluoride during or after the growth of the SOIR seems to be a promising route for achieving surface morphologies better adapted to the growth of µc-Si than the sharp valleys produced by the front electrode and the deposition of the a-Si cell and the IRL. A smoothened SOIR could revolutionize Micromorph cell design by allowing sharp and high aspect ratio front electrode morphologies for the a-Si cell, while providing non-flat but smoother surfaces for the growth of the µc-Si cell. Furthermore, if realized with an in-situ process such a process, could be transferred to industry rapidly (patent filed)[8].

7 Local V_{OC} mapping and V_{OC} stability of Micromorph cells

Lock-in thermography measurements are used in this chapter to map spatial variations of V_{oc} in Micromorph cells. Section 7.1 compares different biasing techniques and justifies an electrical bias with a constant forward current density as the most appropriate choice for comparison of Micromorph cells. In section 7.2 thermographs are used to correlate V_{oc} degradation with the appearance of a border effect. We show that V_{oc} degradation of the cells can be accelerated by exposing them to water vapor, that the degradation is partially reversible with annealing and that the borders of µc-Si cells are the most affected regions. Section 0 discusses different ways by which water vapor can reach the i-µc-Si layer and section 7.4 compares V_{oc} degradation of Micromorph cells on substrates with different roughness. Section 7.5 and 7.6 explain how, in the Micromorph configuration, V_{oc} degradation can be worsened by the presence of a possibly porous intermediate reflecting layer (IRL).

The main results shown in this chapter are to be published.[7]

7.1 Local V_{OC} analysis with lock-in thermography

Lock-in thermography is a sensitive technique used to map the heating of a solar cell.[137] In our lab we use a ThermoSensorik setup, consisting of an infrared camera, type CMT 384 M, with a spectral range of 3–5 µm. A pulsed electrical voltage or pulsed illumination (LEDs with 530 nm or 940 nm wavelengths) can be used to bias the solar cell, and a lock-in technique maps the heating caused by the bias.

A border effect on a µc-Si cell was first observed by X. Niquille with the thermographs shown in Figure 7-1. On this cell, three small heating points are visible in electrical reverse bias and the same three heating points plus the border of the cell appear in forward bias. This difference between reverse and forward bias can be understood with the schematic *I-V* characteristics shown in Figure 7-1 illustrating the three most common electrical behaviors found within a spatially non-uniform thin-film silicon solar cell: resistive shunts, bad diode regions (high reverse saturation current), and good diodes regions (low reverse saturation current). Because both good and bad diodes are blocking current in reverse bias, only the resistive shunts can dissipate heat and are thus detected in the thermographs. At moderate forward bias (near device V_{oc}) both resistive shunts and bad diodes dissipate heat. By comparing forward and reverse bias measurements it is thus possible to clearly separate these two spatially localized behaviors that can negatively affect solar cell performance.

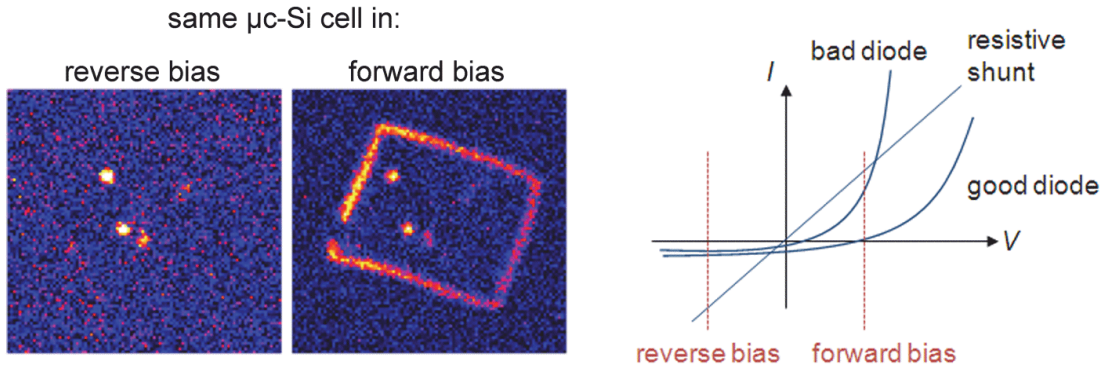

Figure 7-1 Lock-in thermographs of µc-Si cells (by X. Niquille) and *I-V* characteristics of the three most common electrical behaviors that can be found in different regions of spatially non-uniform thin-film silicon solar cells.

Figure 7-2 shows thermographs of a Micromorph cell in different electrical bias conditions. From the thermograph acquired with a reverse bias of –5 V, we can conclude that there are no shunts in this device. The forward bias voltages of 1.2, 1.6, and 2.2 V show how the local V_{oc} is first reached only at the borders of the cell, and that even for higher forward bias, significantly more current flows through the border regions. When comparing the second with the last image it can be seen that a similar result can be obtained with 7 times higher forward current by adapting the color scale with the same factor. Nevertheless, at high currents, the heat contribution from the TCO becomes visible because the resistive losses (heating) scale with the square of the current, whereas heating in diode regions scales almost linearly with current. In order to analyze the regions with the lowest local V_{oc}, low forward bias currents are therefore preferred for the following experiments. The heating points around the electrical contacts can be partly attributed to high current densities in the ZnO close to the contacts, but there is also a contact resistance between the metal pin and the ZnO layers. Because of resistive losses at this metal/ZnO contact, the applied voltage as indicated in Figure 7-2 is higher than the actual voltage experienced by the solar cell.

On our thermography setup, green or infrared LEDs can also be used to optically excite the solar cells at the lock-in frequency. In this case, the cells are biased with the device V_{oc} corresponding to the illumination intensity. This method is contactless and allows imaging

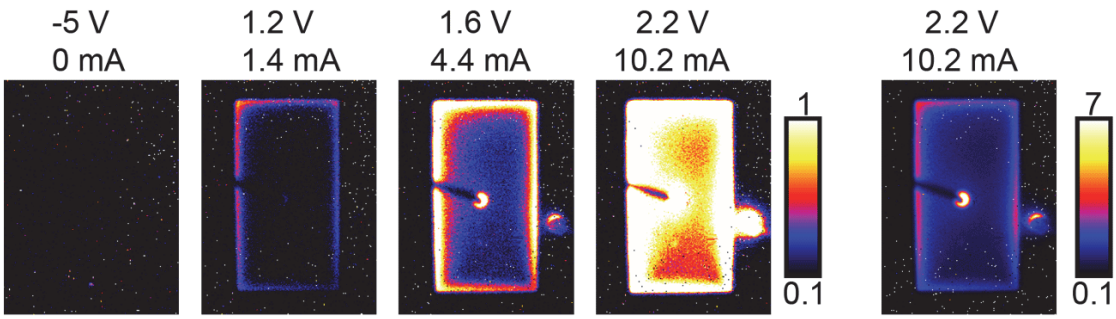

Figure 7-2: Thermographs of a Micromorph cell (Z5-Ar20',180,110,1.8) with electrical bias. The first four images have the same color scale and the color scale is changed for the last image. The black bar entering the cell from the left is the metal pin used to electrically contact the back ZnO layer of the cell. The two round spots indicate the spots where the front and back electrodes of the cells are contacted for the electrical bias.

many cells at once. Furthermore, solar cells can also be imaged if electrical contacting is not possible. These technical advantages are undisputed, but the interpretation of "optical" thermographs is tricky and three pitfalls are discussed in the following paragraphs.

When using infrared excitation, a large part of this light is absorbed and dissipates heat in the TCO layers. This is illustrated in Figure 7-3 (a) on a sample with 16 a-Si cells that do not absorb the infrared light at 940 nm wavelength. The images seen are entirely due to the contribution of the front and back ZnO layer. On the first image the background is nearly black, the front ZnO, visible between the a-Si cells is blue and the cells, where both the front and ZnO contribute to the heating, are orange. When increasing the color scale by a factor of two (second thermograph) the color of the cells is the same blue as the color of the front ZnO in the first image. This indicates that the front and back ZnO (both Z2 in this case) contribute equally to the orange color in the first image. If the front and back electrodes are different, their contributions will not be equal. When measuring the cells from the glass side, the color scale has to be significantly lowered, because of heat absorption in the glass.

When using green excitation, an optical border effect can be observed in thin-film silicon solar cells deposited on a rough front ZnO. In this configuration, light shining on the front ZnO is easily trapped in the ZnO and glass due to total internal reflection at the ZnO/glass, glass/air, and ZnO/air interfaces. Because green is not absorbed in the ZnO or the glass, it can travel laterally several millimeters to centimeters. If green light enters into the region of the solar cell, it is transmitted into the silicon layers due to the higher refractive index of the silicon compared to ZnO (no total internal reflection possible; the silicon layers act as a light sink). This effect is illustrated in Figure 7-3 (b) with a Micromorph cell, but has also been observed in a-Si and µc-Si single junction cells. For the thermograph shown in the same figure, the front ZnO on one side of the cell was covered with Tipp-Ex, which stopped the green light from reaching the front electrode, and canceled the border effect.

In Micromorph cells, an electrical problem arises when working with optical bias because of unequal light absorption in the sub-cells. Infrared light, for example, is absorbed only in the µc-

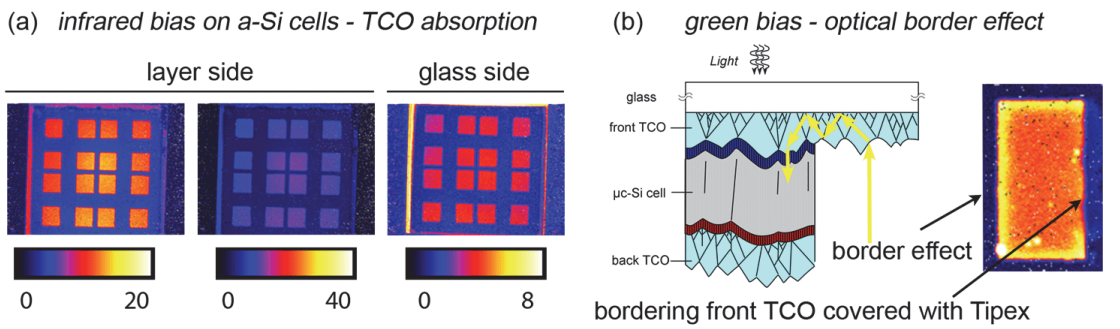

Figure 7-3: (a) Thermographs of 16 a-Si cells (0.25 cm^2) with infrared bias with different color scales, measured from the layer and the glass side. (b) Schematic and thermograph of a Micromorph cell (1.2 cm^2) showing a border effect caused by light trapping in the surrounding front ZnO layer. The front ZnO is covered with Tipp-Ex on one side of the cell, canceling this optical border effect.

Si bottom cell, and the a-Si cell blocks current in both directions. If the photo-generated current from the µc-Si cell is consumed in a region with lower V_{oc} (shunt or bad diode) then it can flow laterally through the back ZnO, but it has to flow also through thin doped silicon layers between the sub-cells. Due to the low lateral conductivity of the doped silicon layers, heating will occur in these layers. The distribution of the local V_{oc} can still be seen, but interpretation of the thermographs depends on the nature of the doped layers used between the sub-cells.

The thermographs of Micromorph cells shown in the following sections are mostly acquired with electrical bias, due to the difficult interpretation of thermographs with optical bias in the tandem configuration. Because of varying contact resistance between the metal tip and the ZnO, we compare measurements with the same forward bias current density of 1.2 mA/cm^2, which allows analyzing the spatial distribution of local V_{oc} in the Micromorph cells. The voltage is adapted to maintain the same forward current density applied to all cells and the color intensity of the thermographs in this configuration does not reflect the quality of the cell, but serves only to analyze the spatial distribution of the applied forward current.

7.2 V_{OC} degradation on µc-Si cell borders due to water vapor

When a solar cell is illuminated in V_{oc} conditions, all the photo-generated electron-hole pairs recombine again in the device and generate heat in the solar cell. Ideally, the recombination is homogenously distributed over the solar cell area, indicating also a homogenous distribution of local V_{oc}. If there is a spatially inhomogeneous distribution of recombination rates then currents will start to flow within the device giving rise to temperature inhomogeneities that can be detected with lock-in thermography. Figure 7-4 (a) shows a thermograph of two µc-Si cells deposited on a rough front electrode (Z5), illuminated with infrared light in open-circuit conditions. Figure 7-4 (b) shows a thermograph of the same µc-Si cells after five hours' exposure to damp heat conditions (60° C, 100% humidity). The V_{oc} of these cells is 62 mV lower after damp heat exposure and, it can be seen that the heat distribution becomes inhomogeneous, with strong heating at the borders of the cells. This border effect also appears in electrical forward bias, but cannot be seen in reverse bias indicating diode-like behavior. Such a cell can be described with a diode array model as shown in Figure 7-4 (c) with good regions represented by good diodes with low reverse saturation currents (J_{01}) in the center of the cell and contaminated, bad regions represented by diodes with higher reverse saturation currents (J_{02}) on the border. These regions with different electrical behaviors are connected in parallel by the front and back electrode layers. If this device is operated in V_{oc} conditions (no current flows out of the device), then the good diode regions are operated below local V_{oc} conditions and generate current that is consumed in bad diode regions which are operated above local V_{oc} conditions (current circulates within the device). Figure 7-4 (d) shows the *I-V* characteristics of the bad-diode and good-diode behaviors. If a device is governed by the two *I-V* curves shown in this particular case, the surface with good-diode behavior is three times

larger than the surface with bad-diode behavior, and lateral resistance in the ZnO is negligible, then this cell has a "device V_{oc}" as indicated by the red line, where "one" bad diode is compensated by the "three" good diodes.

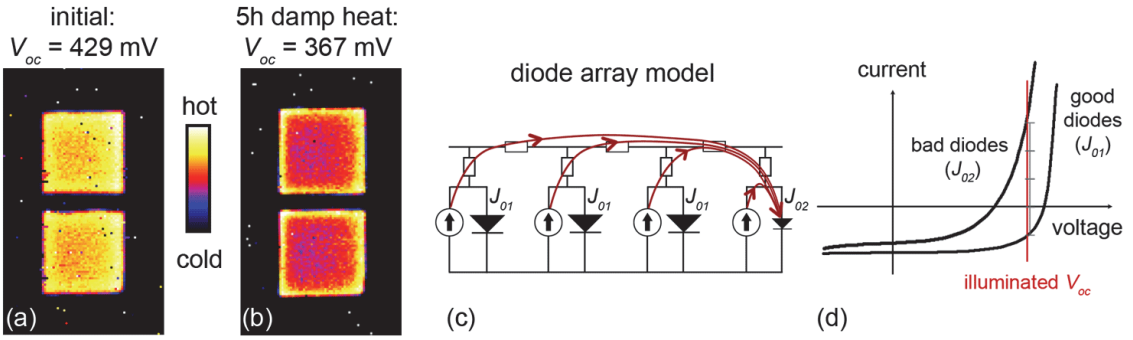

Figure 7-4: (a)-(b) Thermographs of the same two µc-Si cells (Z5/1.5), illuminated with infrared light (940nm) with the same color scale before and after damp heat exposure (60 °C and 100% humidity). (c)-(d) Diode array model and *I-V* curves for thin-film silicon solar cells with an inhomogeneous distribution of reverse saturation currents (J_0).

Figure 7-5 (a) shows the V_{oc} evolution of a Micromorph cell. After 10 months of air storage, the V_{oc} of this cell has lost 70 mV from the value measured after the first annealing that followed cell fabrication. After a second annealing, the V_{oc} recovers 60 mV almost reaching the first value. In damp heat conditions (85 °C, 85% humidity) the V_{oc} decreases again rapidly, indicating that water vapor is causing the V_{oc} degradation. In the Micromorph configuration, this V_{oc} loss can be caused by both the a-Si and the µc-Si sub-cells.

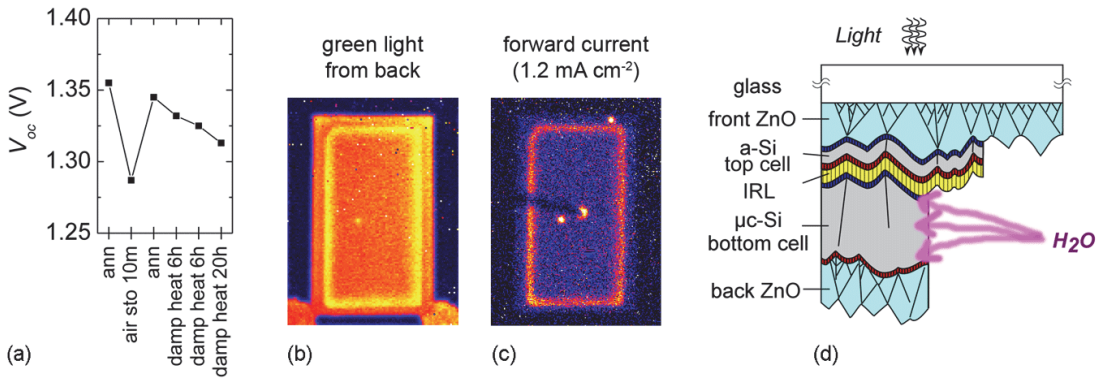

Figure 7-5: (a) V_{oc} evolution of a Micromorph cell (Z5-Ar30'/300/SOIR110/3.0). (b) Thermograph with green light bias of a different Micromorph cell (Z5-Ar20'/250/ZIR900+ArST/2.4, fabrication: D. Dominé) that was patterned with a two-level structure. (c) Same cell as (b) but with an electrical forward current bias. (d) Schematic of a two-level-patterned Micromorph cell.

Figure 7-5 (b) and (c) show thermographs of a Micromorph cell with a conducting ZnO intermediate reflector (ZIR) that has lost 40 mV in V_{oc} after prolonged air storage. To distinguish the borders of the two sub-cells, a two-level patterning is used as illustrated in Figure 7-5 (d) with the µc-Si bottom cell area being smaller than the a-Si top cell. In both optical and electrical thermographs a strong border effect can be seen for the smaller µc-Si cell indicating that water vapor in-diffusion and V_{oc} degradation is mainly affecting the borders of

the µc-Si bottom cell. This is in agreement with previous studies by Niwano et al.[138] identifying water vapor as a major source of oxidation of crystalline silicon surfaces stored in air, and by Smets et al.[139] showing that µc-Si bulk oxidation, most probably at grain boundaries, can have a strong impact on µc-Si cell performance.

Figure 7-6 shows V_{oc} and electrical thermographs of a strongly degraded Micromorph cell before and after laser scribing, used to electrically isolate the borders. The significant increase in device V_{oc} confirms that its degradation is mostly due to the border regions seen in thermographs.

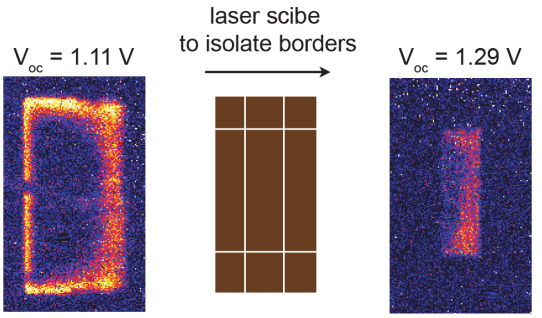

Figure 7-6: Thermographs of a Micromorph cell (Z5-Ar20'/220/130/3.3) with strongly degraded V_{oc} before and after electrical isolation of the border regions by laser scribing (Laser scribing: A. Miéville). The thermographs, which were taken with a constant forward current density of 1.2 mA/cm^2, indicate the spatial distribution of the recombination currents.

In summary, we observe that water vapor affects the borders of µc-Si cells, resulting in reduced local V_{oc} that can affect the electrical performance of the entire cell. In previous studies about water-vapor-induced V_{oc} degradation, it has been shown that the µc-Si layer deposition process has a strong influence on V_{oc} degradation.[140] This point was not addressed in our study and all cells presented in this chapter were deposited with the same i-µc-Si layer process leading to µc-Si cell efficiencies of 8.0 – 9.0%.[22] In the following sections we first present different paths for water vapor in-diffusion and then discuss the influence of ZnO electrode roughness and IRLs on the V_{oc} degradation process.

We would like to point out here that H_2O-induced V_{oc} degradation also happens during the standard light-soaking procedure. For µc-Si and Micromorph cells, therefore, one has to pay attention to different degradation processes, and not directly conclude that all losses after the light-soaking procedure are due to light-induced Staebler-Wronski degradation.[42]

7.3 Possible ways for water in-diffusion

In the previous section, we showed that the diffusion of water vapor into the border of the i-µc-Si absorber layer is the main process causing the partially reversible V_{oc} degradation. The border of the i-µc-Si layer is directly exposed to air and chemical reactions with oxygen can take place easily, but from thermographs, it can be seen that the border effect can penetrate up to several millimeters towards the center of the cell. For these regions millimeters away from the physical border, different paths can be imagined as illustrated in Figure 7-7.

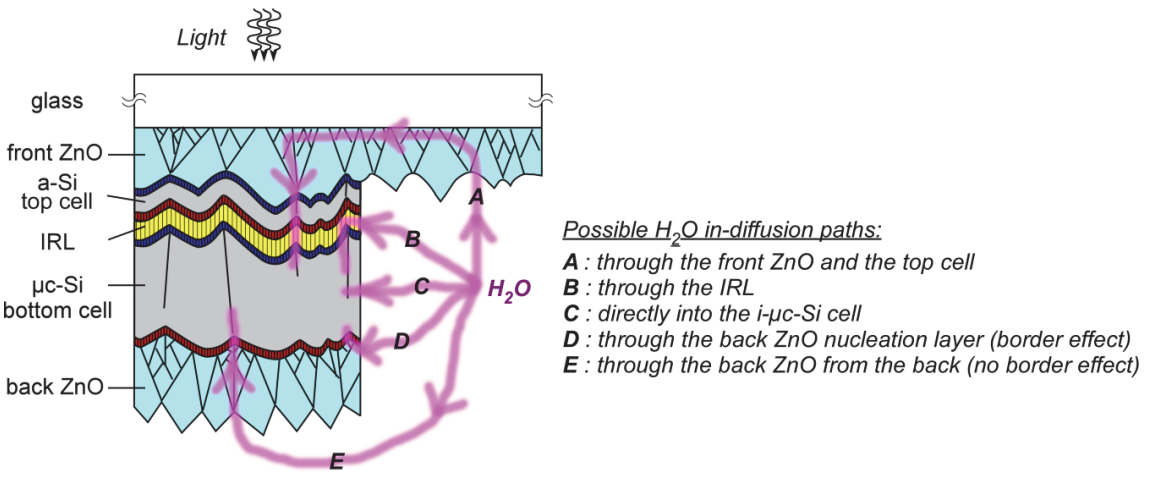

Figure 7-7: Schematic of a Micromorph cell with different paths by which water vapor can reach the i-µc-Si layer.

If, for example, the front ZnO is more permeable to water vapor than the µc-Si layer itself, it seems probable that water vapor reaches the center of the cell faster by first penetrating millimeter distances through the ZnO and by crossing the ~250 nm of a-Si cell and IRL (path A). This path should be favored on rough LP-CVD front ZnO, where the porous grain boundaries of ZnO laterally coincide with the regions of less dense material in the solar cells (cracks). Although this path might seem unlikely at first, it could be the one that dominates the local V_{oc}

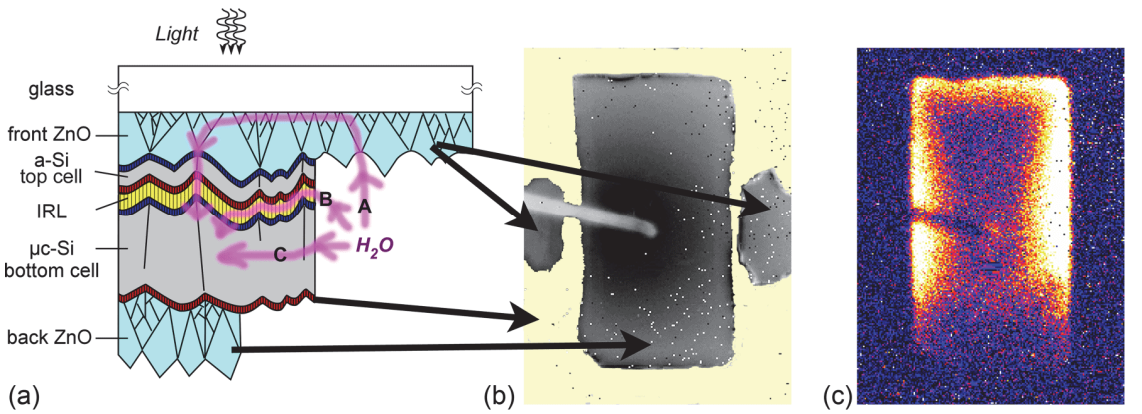

Figure 7-8: (a) Schematic of a Micromorph cell (Z5-Ar10'/300/260/3.2) with Jülich-type patterning. (b) Photograph and (c) electrical thermograph of a Micromorph cell with Jülich-type patterning. This cell had an initial V_{oc} of 1.30 V, which degraded to 1.16 V after 2 years of storage in air. The thermograph is in the degraded state.

distribution of the Micromorph cell shown in Figure 7-8. This cell has a Jülich-type patterning, which means that the cell size is defined by the layout of the back ZnO, that the surrounding silicon is not removed, and that the front contact is accessed through small openings in the silicon made for this purpose. This is different from our standard cell patterning, where we remove all the silicon around the cell (Figure 7-7). Figure 7-8 (b) shows a photograph of a Jülich-type cell with the large, dark grey rectangle showing the back ZnO of the cell, the small, dark grey ovals the regions where the silicon was removed to access the front ZnO, and the light yellow regions the surrounding silicon, which is not part of the solar cell. Figure 7-8 (c) shows the thermograph acquired with 1.2 mA/cm^2 forward bias current, and the strongest heating can be observed at the border regions closest to the regions where the silicon layers were removed and the front ZnO lays open in order to make electrical connections. The center of the cell does not heat at all, which means that the border regions with locally lower V_{oc} can absorb 1.4 mA with voltages lower than the local V_{oc} of the regions in the center of the cell. For this cell, V_{oc} degradation could seems likely to be dominated by the water vapor in-diffusion along path A, but path B or C could also result in a similar degradation pattern.

Figure 7-9 shows thermographs of Micromorph cells with a different heating pattern. On these cells a permanent marker pattern is drawn onto the bottom cell and erased before deposition of the back ZnO. The pattern is removed with acetone, but some traces are left on the cell, forming a porous entry between the bottom cell and the back ZnO as illustrated in (a). The heating patterns revealed by the thermographs correspond exactly to the marker-traces. The heat lines crossing the cells are stronger at the border and reduce in intensity toward the center of the cell. Although this example is not representative of our standard fabrication process, it shows water vapor in-diffusion along path D, which could also play an important role in standard fabrication processes if the nucleation layer of the back ZnO deposited on rough µc-Si cell is porous.

From these results it becomes clear that, depending on the fabrication method, different in-diffusion processes can account for V_{oc} degradation. In the following sections we show evidence for paths B, C, and E, according to the illustration in Figure 7-7.

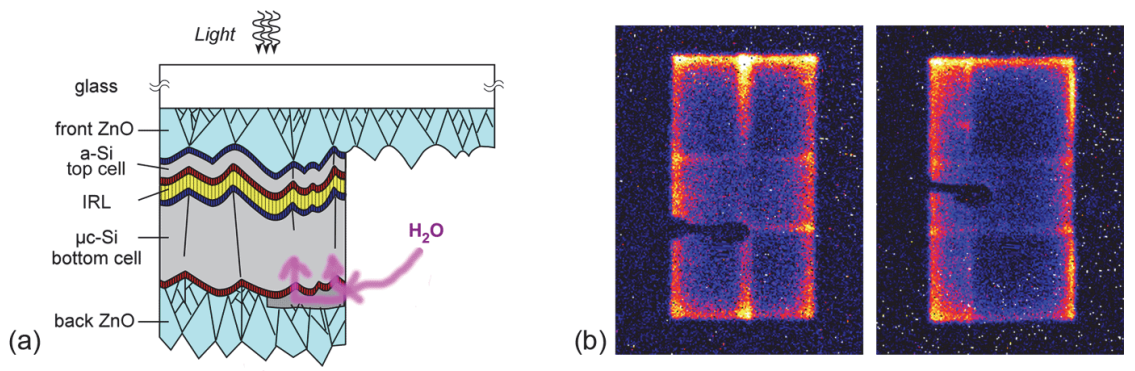

Figure 7-9: (a) Schematic of a Micromorph cell (Z5-Ar10',180,30,1.8) with badly cleaned permanent marker between the bottom cell and the back ZnO. (b) Electrical thermograph. This cell had an initial V_{oc} of 1.30 V that degraded to 1.01V after 15 months in air, and recovered to 1.17 V after annealing. The thermograph was taken after annealing.

7.4 Front electrode roughness and V_{OC} degradation

Figure 7-10 demonstrates repeated, strong V_{oc} degradations of 200 mV (points D and G) for a Micromorph cell deposited on a rough, 5 µm thick ZnO electrode that was exposed to only 10' argon surface treatment (Z5-Ar10') before cell deposition. In this case, the V_{oc} degradation is not completely reversible with the standard 1.5h annealing (point E) and an additional 3 hours of annealing (point F) do not further recover the V_{oc}. The same Micromorph cell deposited on a Z5-Ar20' substrate shows significantly better V_{oc} stability, and on Z5-Ar60', the V_{oc} is almost completely stable.

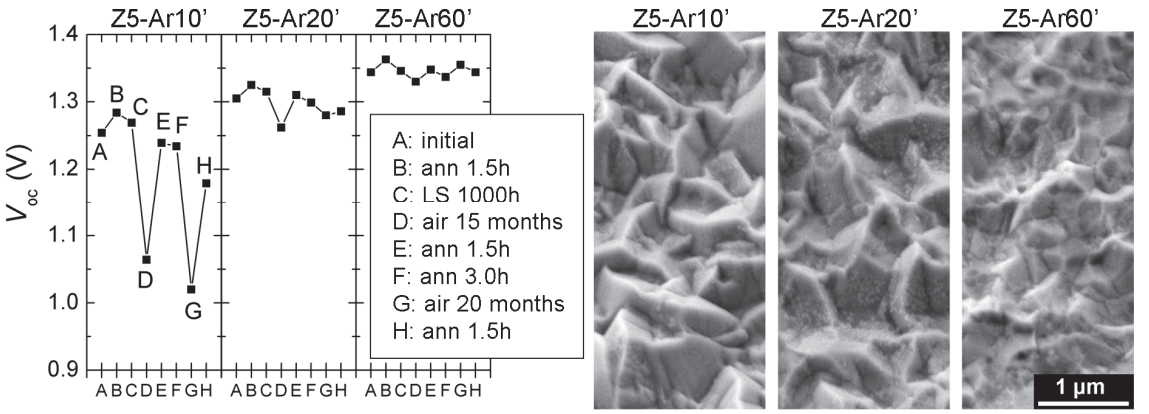

Figure 7-10: V_{oc} evolution of Micromorph cells (Z5-ArX',180,-,1.8) without IRL deposited on Z5 front electrodes modified with 10', 20', and 60' argon surface treatments and corresponding SEM images. (SEM by M. Boccard)

The local distributions of V_{oc} after 20 months of air storage and after subsequent annealing (points G and H in Figure 7-10) are shown by electrical thermographs in Figure 7-11. After air storage, the cell on Z5-Ar60' with a good V_{oc} shows a small border effect, but the center heats homogenously. The local V_{oc} for this cell is only slightly lower at the border than in the center, and probably does not affect the overall cell performance. We conclude that there is no significant H_2O in-diffusion in this case. The cell on Z5-Ar20' shows a stronger border effect and the center of the cell remains dark. The 1.4 mA during the thermography measurement, on the cell with an area of 1.2 cm^2, flows (and heats) entirely in the border regions. The water-vapor-induced V_{oc} degradation on the border (in-diffusion path C) is significant enough to reduce the device performance. The cell on Z5-Ar10' again shows more homogenous heating, but in this

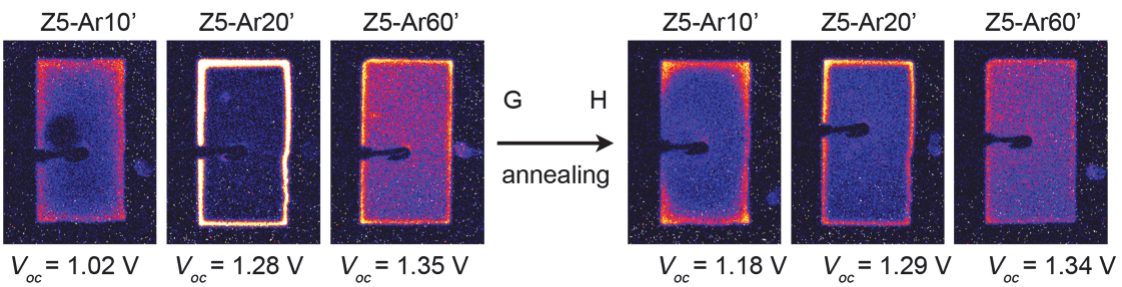

Figure 7-11: Electrical thermographs (1.2 mA/cm^2 forward current) of Micromorph cells deposited on different front electrodes after 20 months of storage in air (same cells as in Figure 7-10, point G) and after subsequent annealing (point H).

case with a homogenously bad V_{oc} (close to 1V) after 20 months' air storage. Water vapor in-diffusion along path E can explain uniform cell degradation without a significant border effect. Alternatively an in-diffusion process from the border can cause uniform degradation if it is fast enough and penetrates the whole cell.

Looking at the reasonably good cells (on Z5-Ar20' and Z5-Ar60'), the annealing reduces the border effect, but does not significantly change the V_{oc} of the cells. The water-vapor-induced V_{oc} degradation visible in thermographs is entirely located at the cell borders in these cases. The cell on Z5-Ar10' shows only 1 V after long air storage which is getting close to the V_{oc} of the a-Si sub-cell (~850mV). Here, water vapor must have penetrated into the whole µc-Si cell, explaining the big V_{oc} variations as well as the absence of a strong border effect before and after annealing.

Figure 7-12 shows cross-section SEM images of Micromorph cells on rough Z5-Ar10' and smooth Z5-Ar60' electrodes. The rough front electrode morphology leads to a high density of cracks in the first case, whereas no cracks are visible in the second. From the front electrode SEM images in Figure 7-10 it can be concluded that cracks starting in the valleys of the ZnO surface are not isolated one-dimensional features, but must form a network following the valleys of the as-grown rough ZnO. These crack-networks can, on the one hand, favor lateral water vapor in-diffusion through the silicon layers, but on the other hand the cracks laterally coincide with grain boundaries in the front and back ZnO layers which can also favor the in-diffusion of water vapor from the ZnO layers into the µc-Si cell.

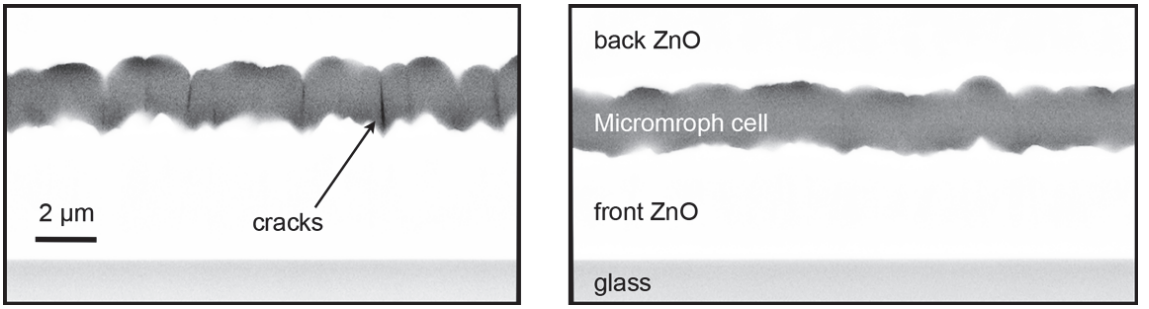

Figure 7-12: Cross-section SEM of Micromorph cells on Z5-Ar10' (left) and Z5-Ar60' (right) from Figure 7-10. The dark lines crossing the cell show the cracks, which are regions of porous material.[66] (The samples were prepared and imaged by M. Leboeuf as described in [141])

The increasing influence of border contamination observed between Z5-Ar60' and Z5-Ar20' electrodes (Figure 7-11) seem consistent with the increasing numbers of cracks on rough substrates, resulting in faster and stronger water vapor in-diffusion from the cell border through the i-µc-Si layer toward the center of the cell. The cell on Z5-Ar10' shows strong V_{oc} degradation and the entire cell seems contaminated. This is rather surprising because the surface morphologies of Z5-Ar10' and Z5-Ar20' are similar (see Figure 7-10). The large difference in V_{oc} stability for similar front ZnO morphologies, which become even more similar after deposition of a-Si cells, is therefore difficult to explain by an increase in crack density or crack sizes in the µc-Si cell. Due to similar surface morphologies after the µc-Si cell deposition,

we also do not expect significant differences in the growth of the back ZnO. By exclusion, we therefore speculate that the V_{oc} degradation in the case of the Z5-Ar10' is due to water vapor in-diffusion through the front ZnO, reaching the i-µc-Si layer by passing through the a-Si cell. Such an in-diffusion process could be stopped by little morphology changes on the front electrode due to slightly longer argon surface treatment times: Either water vapor from the front electrode is blocked by the presence of fewer and smaller cracks in the thin a-Si cell (the a-Si layer is sensitive to slight surface morphology changes of the front ZnO because it grows directly on top of it), or the argon surface treatment process forms an amorphous ZnO layer on top of the polycrystalline ZnO pyramids. This could create a barrier for water vapor trying to reach the silicon layers from the front ZnO.

Polycrystalline ZnO is sensitive to water vapor exposure, which causes the creation of electronic defects at the grain boundaries, thereby increasing grain boundary barrier height and width and decreasing the Hall mobility of carriers in the ZnO layers.[57,142] The grain boundaries of poly-crystalline ZnO are shown in the SEM image (Figure 7-13 (a)) of a Z5 substrate after chemical mechanical polishing (section 2.6). Figure 7-13 (b) shows the same polished ZnO after 10' argon surface treatment at a pressure of 100 mT. The grain boundaries have almost completely disappeared, probably due to re-deposition of amorphous ZnO during the argon surface treatment process (see section 3.2), strengthening the above hypothesis of reduced water vapor permeability after sufficient argon surface treatment.

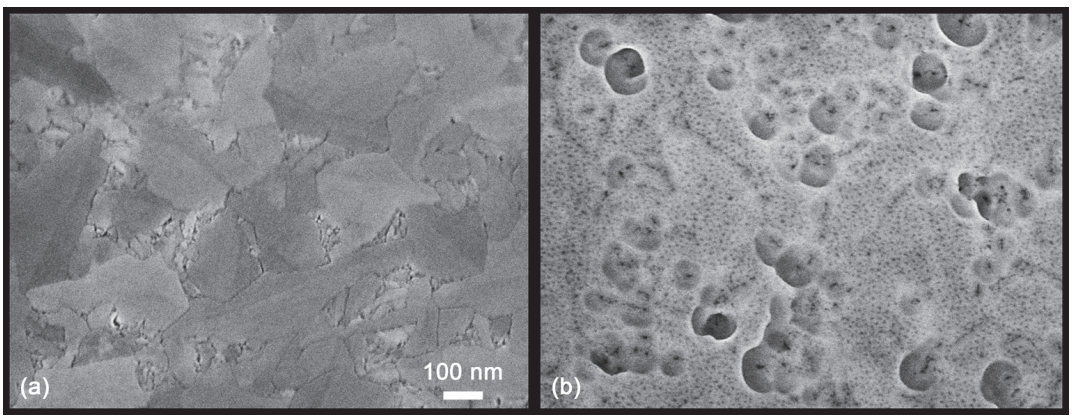

Figure 7-13 Polished Z5 before (a) and after ArST (b) (SEM images: M. Boccard)

In summary, we showed that µc-Si cells deposited on a smooth Z5-Ar60' front electrode have a stable V_{oc}. A small border effect can be observed, but it does not affect device performance. On a rougher Z5-Ar20' electrode, the water-vapor-induced degradation of the local V_{oc} is much stronger and affects a larger border region and device performance is in this case negatively affected. On an even rougher Z5-Ar10' substrate, V_{oc} degradation is strong (–200 mV) and the whole cell area is contaminated. We showed that the degradation is stronger on rougher front electrodes, but Figure 7-10 also shows a commonly observed lower initial V_{oc} on rough electrodes. At this point it is not clear how much this initial value is already affected by contamination, or in other words how high the V_{oc} would be on such a substrate if no contamination were present.

7.5 ZnO intermediate reflectors and V_{OC} degradation

ZnO has a lower refractive index than silicon and can therefore be used as an IRL between the a-Si and the µc-Si absorbers of a Micromorph cell. If a ZnO intermediate reflector (ZIR) is deposited with the same conditions as the pyramidal front ZnO, then nano-rough ZnO pyramids are created on top of the big bumps that stem from the front ZnO plus the a-Si cell (Figure 7-14 (a)). With a post-deposition plasma surface treatment, this morphology can be smoothened. While no variations in the initial Micromorph cell parameters are observed, a significant improvement in V_{OC} stability is demonstrated for cells with smoothened ZIRs. Thermographs show a reduction of the border effect with increasing oxygen plasma surface treatment, and we note that the same effects are observed with argon plasma surface treatments. With respect to the presence of shunts (white spots), we note that the shunting of Micromorph cells with ZIRs is one of the problems that we have not been able to solve. Contrary to what we expected, the number of shunts usually increased with plasma surface treatments of the ZIR. These shunts significantly reduce cell performance in low illumination, but do not necessarily have a detrimental effect at 1-sun illumination conditions.

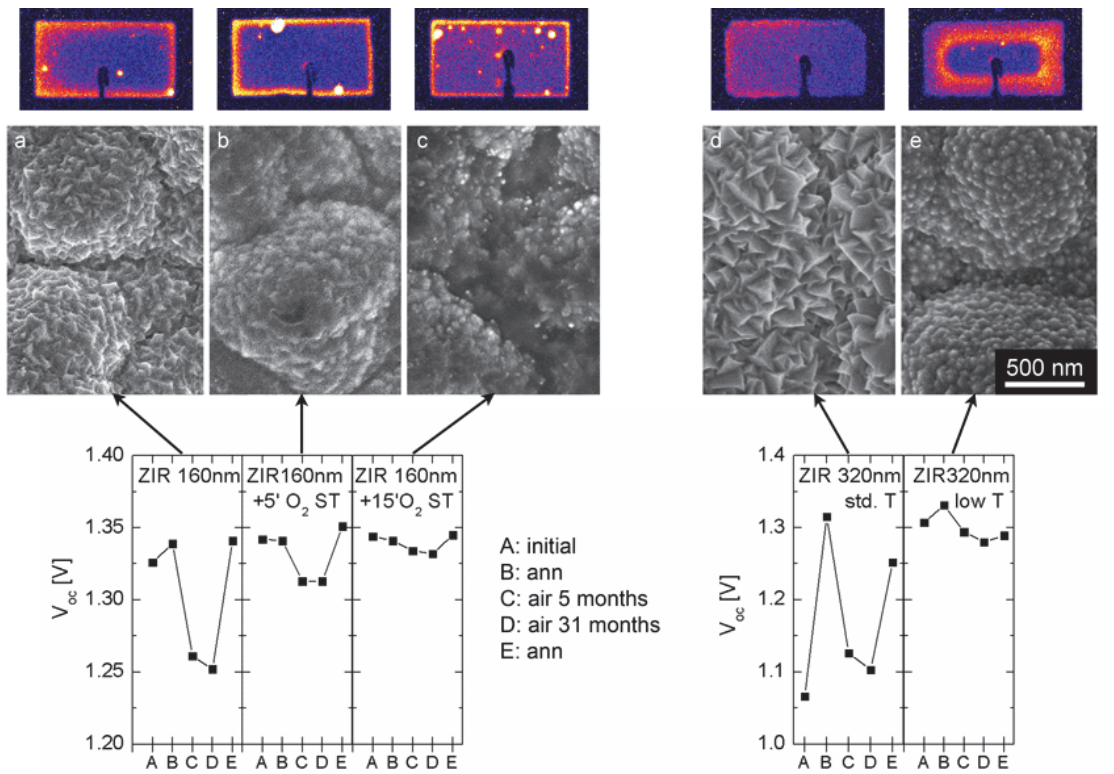

Figure 7-14: (Bottom) V_{OC} evolution of Micromorph cells (Z5-Ar20'/300/ZIR/3.0) with different ZIRs modified by plasma surface treatments or by changing the ZnO deposition temperature. (Middle) SEM images of the different ZIR morphologies. (Top) Thermographs (1.2 mA/cm^2 forward current) of the cells after 31 months of air storage (point D). (Cell fabrication: D. Dominé; SEM images: M. Boccard)

The nano-roughness of the ZIR can be increased by increasing the ZIR thickness as demonstrated in Figure 7-14 (a) and (d). Larger ZnO pyramids cause significantly stronger V_{OC}

degradation (note the change of scale). ZIR morphology can also be influenced by changing the substrate temperature during ZIR deposition. At low temperatures, ZnO grows less crystalline, leading to a "bumpy" surface morphology (Figure 7-14 (e)), significantly better V_{oc} stability, and a "new" type of not understood in-homogeneity in the thermograph. Note that the color intensity of the thermographs does not represent the cell quality, but gives information only about the spatial uniformity of the local V_{oc}.

In section 7.4, we demonstrated that increasing front electrode roughness leads to large cracks crossing the entire µc-Si cells and so enhances contamination by in-diffusion of water vapor. Similarly, increased ZIR roughness also correlates with higher V_{oc} degradation, but the observed feature sizes in this section are much smaller than those described in section 7.4. The roughness introduced by the ZIR (typical feature sizes <100 nm) is not expected to induce a significant change in crack density or crack size in the 3 µm thick µc-Si layer. Taking into account the results from sections 7.4 and 7.6, we propose two explanations for the results shown in this section: V_{oc} degradation is due mainly to water vapor in-diffusion through a network of nano-cracks in the µc-Si layer near the p-i interface, caused by ZIR-induced nano-roughness. Or, the ZIR is the dominant route for lateral water vapor in-diffusion. This second process could be stopped with an amorphous ZnO sealing layer formed during a plasma surface treatment or by the use of an amorphous ZnO material (low T ZIR).

7.6 SOIR and V_{OC} degradation

The previous sections showed that the surface roughness of the front electrode and the presence of a rough ZIR increase V_{oc} degradation. Figure 7-15 shows that increasing SOIR thickness leads to increased V_{oc} degradation for the three different front electrodes used.

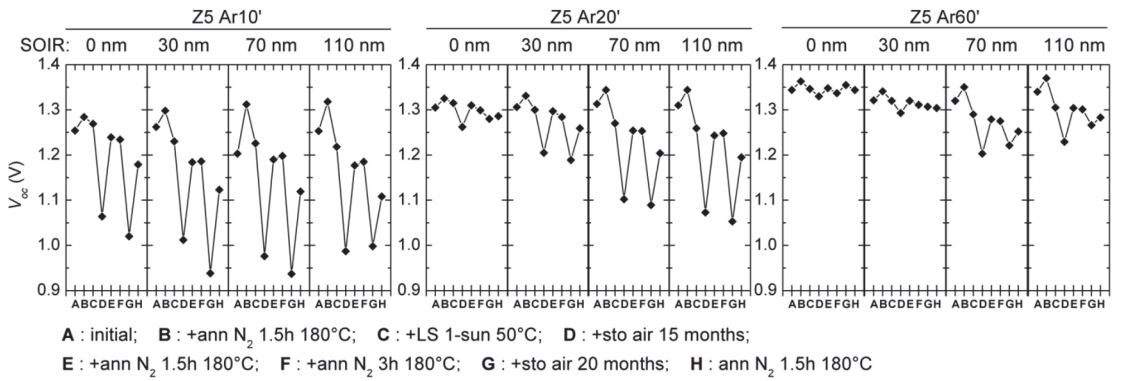

Figure 7-15: V_{oc} evolution as a function of argon surface treatment and SOIR thickness for Micromorph cells (Z5-ArX',180,X,1.8).

Figure 7-16 shows thermographs of the cells on Z5-Ar20' electrodes after 20 months of air storage (point G in Figure 7-15). Without an IRL, the border effect is confined to less than one millimeter from the border of the cell, whereas with increasing SOIR thickness the border

effect penetrates up to several millimeters toward the center of the cells. Annealing the samples leads to less intense and smaller border regions, in agreement with observations in Figure 7-11. To illustrate the good correlation of border effects seen in thermographs with V_{oc} degradation, it is interesting to note that on the for Z5-Ar20' electrodes, the "30 nm SOIR point G" and "70 nm SOIR point H" have similar thermographs and almost the same V_{oc}. The clearly visible asymmetry in heating is due to known inhomogeneities in the argon surface treatment and silicon layer deposition systems. At the edges of these reactors, the argon surface treatment is stronger and the silicon deposition denser (better i-µc-Si quality), commonly leading to higher V_{oc} in µc-Si cells. The cell border that shows less heating was processed close to the reactor's edge and the cell border with stronger heating was processed closer to the center of the plasma reactor.

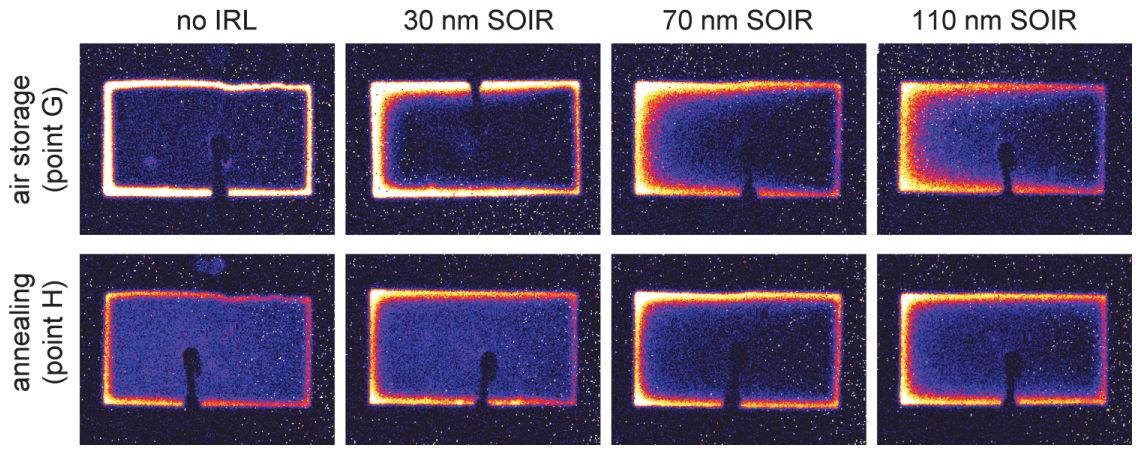

Figure 7-16: Electrical thermographs of Micromorph cells (Z5-Ar20',180,X,1.8 - same as in Figure 7-15) after 20 months of air storage and subsequent annealing. The same color scale is used for all thermographs.

Different substrate morphologies for µc-Si growth cannot be the cause of the observed V_{oc} degradation here because the SOIR layers are deposited by PECVD which can alter the substrate slightly (section 3.3) but cannot significantly change the substrate roughness. Figure 7-17 shows cross-sectional SEM images of two Micromorph cells on Z5-Ar60' without a SOIR and with a 110 nm SOIR. No cracks can be identified in either case. It also seems unlikely that a Micromorph cell on strongly smoothened Z5-Ar60' with a 70 nm SOIR (max. V_{oc} deg: 150 mV) has more cracks than a Micromorph cell on Z5-Ar20' without a SOIR (max. V_{oc} deg.: 60 mV). From Figure 5-10 (a) we know that in-plane resistivity increases rapidly when the SiO_x layers are exposed to air, indicating that SOIR layers are porous enough for in-diffusion of water vapor. This nano-porosity is confirmed by X-ray reflectometry (Figure 5-10 (b)) and TEM (Figure 5-8) and also explains why the SOIR gives a darker contrast in the SEM image of Figure 7-17 compared to the silicon layers and the glass substrate.

To conclude, we speculate that with SOIRs, similar to the results with ZIRs, a main route for water in-diffusion could be through the IRL several millimeters towards the center of the cell, reaching the p-i interface of the µc-Si cell after crossing only the n- and p-type µc-Si layers (~ 30 nm).

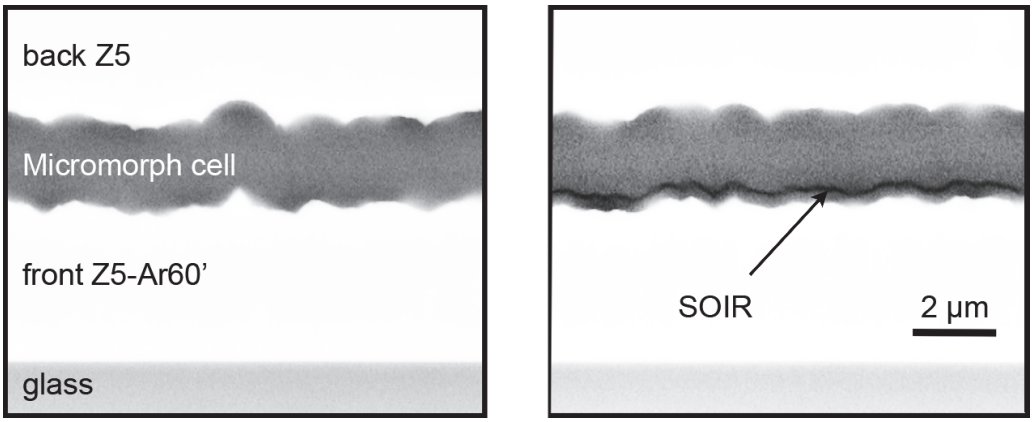

Figure 7-17 SEM cross-sections of Micromorph cells on Z5-Ar60' without a SOIR (left) and with a 110 nm SOIR (right). (SEM images: M. Leboeuf)

7.7 Conclusion

In this chapter we correlated the V_{oc} degradation of Micromorph cells with the contamination of the border regions, most likely due to in-diffusion of water vapor from the atmosphere into the i-µc-Si layer. We showed evidence that water vapor in-diffusion can increase with the presence of crack-networks in the µc-Si layer, caused by rough front electrode substrates, but we pointed out that other layers with possibly higher porosity (e.g. ZnO and SiO_x) could act as channels where water vapor can travel millimeter-long distances toward the center of the cells, and then reach the i-µc-Si layer by crossing only the thin doped layers. Micromorph cells on rough substrates degrade more than on smooth substrates, but their initial performance is also lower. As annealing can only partially reverse the degradation effect, at the moment it is not clear how much the initial efficiency is already affected by the water-vapor-induced degradation process. In the present cell fabrication process, the i-µc-Si layer is already exposed to water vapor during the deposition of the back ZnO and during the lift-off procedure. It is speculated that cells on rough front electrodes could show significantly higher performances if they were never exposed to water vapor.

In order to stop water vapor in-diffusion and so avoid V_{oc} degradation of µc-Si cells, different solutions should be investigated in the future: First, cells could be encapsulated to stop water vapor from the atmosphere from reaching the cell. Second, V_{oc} degradation can be reduced by reducing i-µc-Si porosity, either by the use of adapted PECVD conditions[140] or by using smooth substrates (section 7.4). Water contamination in these cases will still occur, but is limited to a narrow border region, and will not significantly influence the overall cell characteristics. Third, special n- and p-type layers (doped a-Si, doped SiO_x, or amorphous TCO) could be added in cells in order to stop water vapor diffusion from the surrounding layers into the i-µc-Si layer. Fourth, after the completion of the cell or module fabrication, a water vapor impermeable layer such as silicon nitride could be deposited by PECVD or sputtering to directly seal the cells before the lamination of the entire module.

8 Back reflectors

The back reflector is an important component of every thin-film silicon solar cell because of the incomplete light absorption in the thin absorber layer. The most common back reflector currently used in research is composed of a sputtered ZnO layer (~80 nm) and a sputtered silver (Ag) layer (~200 nm).[49] This layer stack shows excellent reflectivity if deposited on a flat cell structure, but on rough cells the reflectivity is decreased by the excitation of surface plasmon polaritons (SPP) at the ZnO/silver interface. Springer et al.[143] showed SPP-related absorption peaks at ~440 nm and an absorption tail that can extend into the spectrum of interest for µc-Si and Micromorph cells (500–1100 nm in air). The origin of SPP absorption and the role of the ZnO layer were investigated in greater detail by Haug et al.[144]

In our lab, we use a thick 2–5 µm LP-CVD ZnO layer with sufficiently low sheet resistance to laterally collect the current in combination with a dielectric, diffusely reflecting sheet (3 mm thick PTFE polymer from Gore) at the back of the solar cell.[50] White paint, white paste, or Tipp-Ex give similar results and can also be used as alternatives to the white sheet. In this back reflector there is no absorption in the dielectric reflector, but there is free carrier absorption (FCA) in the ZnO layer due to the electrical requirements for the lateral collection of the current.[17] For rough cell configurations, it is not clear which of these two solutions allows for lower parasitic absorption and thus for higher solar cell current densities. Unfortunately, we lack in our lab an optimized sputtering process that allows one to make a fair comparison between the two configurations on rough µc-Si or Micromorph cells.

In this chapter we show preliminary results for a configuration that may be better, making use of the advantages of both solutions described above. An LP-CVD ZnO film, with low free carrier density and slightly thicker than the peak-to-peak distance of the µc-Si cell is polished and covered with a sputtered silver layer. This configuration should prevent SPP absorption thanks to a flat ZnO/silver interface, and at the same time avoid FCA in the ~1 um thick ZnO layer that has been freed from in-plane conductivity requirements. Towards the realization of such a zero-absorption back reflector we present in section 8.1 experimental results of different back reflector configurations making use of as-grown rough and polished LP-CVD ZnO. In section 8.2 we analyze the influence of the interface morphology and the material properties on absorption in LP-CVD-ZnO/silver reflectors.

The results shown in this chapter are not published elsewhere.

8.1 Comparison between different back reflector configurations

The visible part of the solar spectrum is easily absorbed by thin silicon layers, but the red and near-infrared part, where the absorption coefficient of silicon is lower, are not. Light that is not absorbed after passing through the silicon layers (wavelength >500 nm) can be internally reflected by the Si/back-ZnO interface, or at the back reflector behind the back-ZnO electrode. In this section we compare three back reflectors: a 250 nm thick silver layer deposited by magnetron sputtering onto the back-ZnO; a dielectric sheet with 100% diffuse reflection pressed against the back-ZnO; and a foil (metal film on plastic substrate) with nearly 100% specular reflection pressed against the back-ZnO.

Figure 8-1 (a) compares the EQE of 1.1 µm thick µc-Si cells deposited on rough Z5-Ar20' front electrodes with different back reflectors. The lowest EQE in the infrared is obtained when no back reflector is applied to a 5 µm thick, lowly doped, LP-CVD back-ZnO electrode. A higher EQE in the IR is achieved with a 2 µm thick un-doped LP-CVD back-ZnO electrode covered with a sputtered silver film and annealed at 180 °C. This configuration allows reducing the FCA in the back-ZnO as the current is laterally extracted by the silver layer. However, it can be seen that the EQE between 500 and 700 nm is lower that without back reflector. This is attributed to a strong SPP absorption at the rough back-ZnO/silver interface, which will be investigated in section 8.2. The highest EQE is obtained when a dielectric reflector is applied to the back-ZnO electrode, and no difference is observed in this configuration between diffuse and specular reflectors. Figure 8-1 (b) shows the same experiment but for cells deposited on a flat front electrode (polished un-doped Z7) with a rough Z5 back electrode. For these cells, the EQE in the infrared part of the spectrum is significantly lower due to the absence of light scattering at the front-ZnO/Si/back-ZnO interfaces. As in Figure 8-1 (a), the lowest EQE is observed with no back reflector and the highest with dielectric back reflectors.

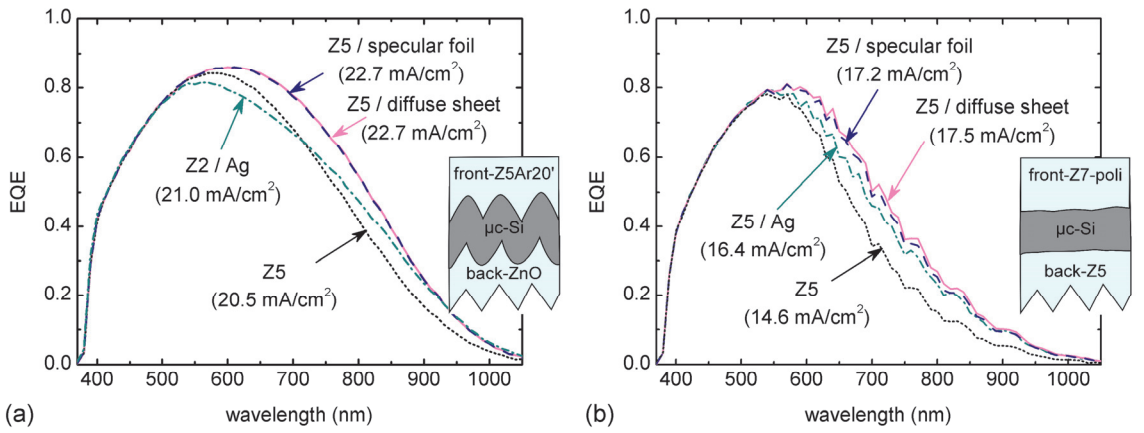

Figure 8-1: EQE of 1.1 µm thick µc-Si cell deposited on (a) Z5-Ar20' and on (b) polished Z7 with different back reflectors. The cells are annealed at 180 °C and the corresponding short-circuit current densities are given in parentheses.

Figure 8-2 (a) shows the EQE of the same µc-Si cells deposited on smoothened Z5-Ar60', with a flat back-ZnO electrode (polished Z5). In this configuration, the sputtered silver film and the specularly reflecting foil give the same EQE, because there is no SPP absorption in the flat silver layer. Furthermore, it can be observed that the use of a diffuse back reflector increases the EQE in the infrared for µc-Si cells deposited on a smoothened Z5-Ar60' front electrode with incomplete light scattering at the front-ZnO/Si/back-ZnO interfaces. This observation is confirmed in Figure 8-2 (b) for µc-Si cells with 2 µm thick un-doped back-ZnO layers. On a polished back-ZnO electrode, a significant increase in EQE can here be achieved with a diffuse reflecting sheet compared to the specularly reflecting foil. Differently, the EQE is the same when the specular or diffuse reflector is applied on a rough back-ZnO electrode with an air gap before the back reflector because light is in this configuration scattered at the rough back-ZnO/air interface. The influence of the back reflector on the EQE depends on the degree of light-scattering on the other optical interfaces in the solar cell, which is in agreement with recent studies by Sai et al.[145] analyzing the influence of front-ZnO/Si and Si/back-ZnO interface roughness on light-scattering in µc-Si solar cells. In summary, our experiments indicate that light-scattering at the back reflector can improve the solar cell current if the scattering is not complete at the front-ZnO/Si/back-ZnO interfaces. This is not necessarily intuitive because the angular distribution of light-scattered at the back reflector will be narrowed when transmitted from the ZnO into the silicon[87] and is therefore expected to play a minor role compared to light-scattering at the optical interfaces with the silicon layers.

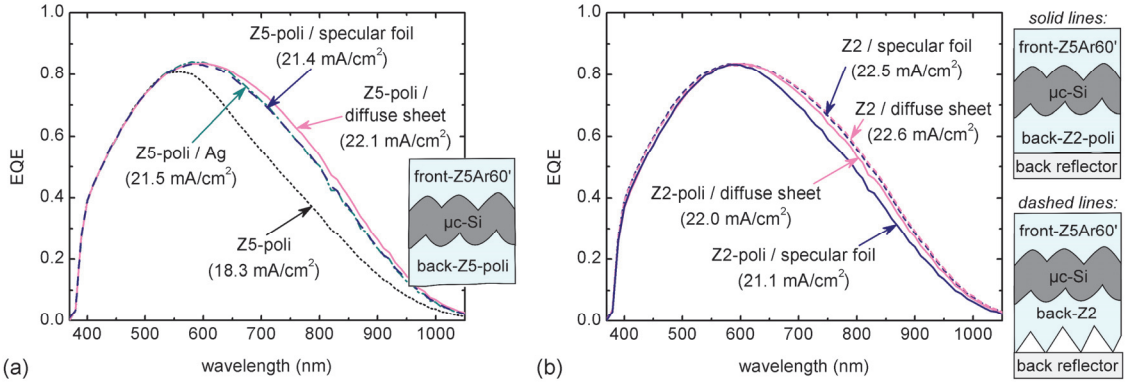

Figure 8-2: EQE of 1.1 µm thick µc-Si cells deposited on Z5-Ar60' with (a) polished back-ZnO electrodes (Z5) and (b) rough and polished back-ZnO electrodes (Z2) with different back reflectors. The cells are annealed at 180 °C and the corresponding short-circuit current densities are given in parentheses.

8.2 Rough ZnO/silver back reflector

Silver is a good reflector in the flat configuration, but in Section 8.1 we showed that there are significant EQE losses when sputtered silver is used as back reflector on top of a rough back-ZnO electrode. In order to correlate back-ZnO morphology with SPP absorption losses in the ZnO/silver reflector, in this section we study the reflectance of glass/Z2/silver stacks, which simulate conditions in thin-film silicon solar cells with rough-ZnO/silver back reflectors.

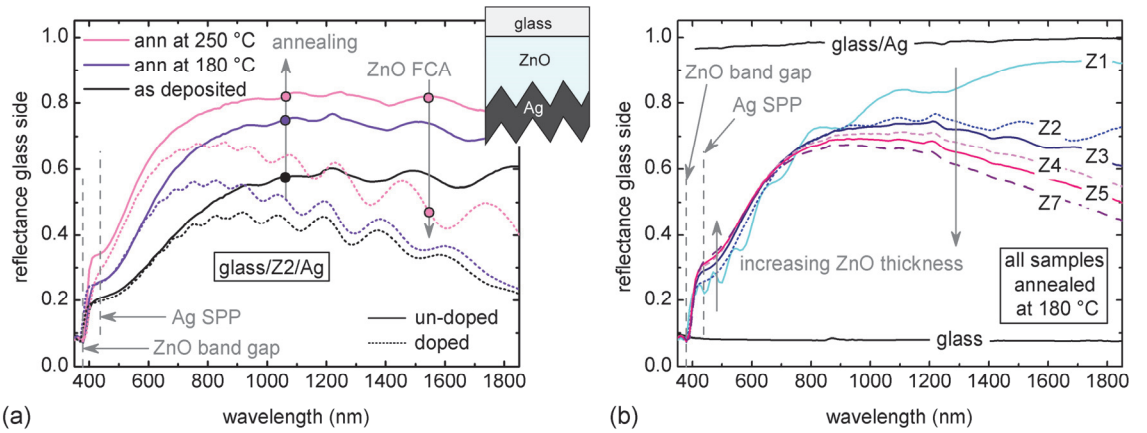

Figure 8-3: (a) Reflectance of glass/Z2/silver stacks with Z2 layers with standard doping and un-doped Z2 layers, as deposited and after annealing and 180 °C and 250 °C. (b) Reflectance of glass/ZnO/silver stacks with 1–7 µm thick, un-doped ZnO layers (Z1–Z7) after 180 °C annealing.

Figure 8-3 (a) shows the reflectance of glass/un-doped-Z2/silver stacks as deposited and after annealing at 180 °C and 250 °C. The low reflectance (high absorptance) of these stacks for wavelengths <370 nm is due to the band-gap absorption of ZnO. Between 400 and 800 nm the absorption is dominated by the SPP absorption with the peak at ~440 nm, in agreement with previous studies.[143,144] Annealing these samples results in a lower and narrower SPP absorption peak, presumably due to the improved silver material properties after annealing as reported by Söderström et al.[146] After a higher annealing temperature of 350 °C (not shown here), all silver layers clotted into silver balls and bands with openings in between, which significantly decreased the reflectance of the layers. The partial transmittance of light for these films makes the observation of possible further improved silver material quality impossible. Regardless, in the p-i-n configuration the annealing temperatures are limited to 200 °C because higher temperatures can lead to a degradation of the cell parameters.

For wavelengths above 800 nm, there is FCA in the ZnO layer that plays an increasing role in reducing the measured reflectance. This is illustrated by the comparison of the non-intentionally doped Z2 (solid lines; with free carrier density of $3 \cdot 10^{19}$ cm^{-3}) with the Z2 with standard doping in order to obtain a sheet resistance of 10 Ω (dotted lines; free carrier density of $8 \cdot 10^{19}$ cm^{-3}).[75] The FCA steadily reduces the reflectance with increasing wavelengths. This absorption can be reduced by reducing the doping or the thickness of the ZnO layer. Reducing the FCA can significantly improve the EQE of µc-Si cells in the infrared but leads to a trade-off

with the increasing resistance of the ZnO film, which can negatively affect the *FF* of the cell. We studied the effect of FCA on the EQE of µc-Si and Micromorph cell performance and detailed discussions of this subject are published by Dominé et al.[10,87] and Boccard et al.[17] With respect to the reflectance measurements presented here, it has to be noted that the absolute levels of reflectance (1–absorptance) of the glass/ZnO/silver stacks are not completely representative of the silicon/ZnO/silver configuration in thin-film silicon solar cells. This is because in the layer stacks the diffuse light reflected at the ZnO/silver interface is again reflected at the air/glass/ZnO interfaces and can be partially trapped in the ZnO, which enhances the absorption. Light-trapping within the ZnO is reduced in the solar cell configuration due to the higher refractive index of silicon in contact with the ZnO/silver stack. The absorption observed in the glass/ZnO/silver stacks therefore exaggerates the absorption in the solar cells configuration, but the observed tendencies are expected to be the same.

Figure 8-3 (b) shows the reflectance of glass/ZnO/silver stacks with increasing ZnO layer thickness and increasing ZnO pyramid sizes (Z1-Z7, with RMS roughness from ~40 to 250 nm; for more details see sections 3.1 and 3.2). This experiment demonstrates that the plasmonic absorption in our ZnO/silver stacks does not significantly depend on the size of the pyramids that form the ZnO/silver interface. Even though these samples are all un-doped, the increasing FCA for wavelengths >800 nm can clearly be observed with increasing ZnO layer thickness. It is also interesting to note that the glass/Z1/silver stack shows a high reflectivity of ~90% for wavelengths >1500 nm and it can be concluded that the plateau in reflection observed for the glass/un-doped-Z2/silver stacks is due to equivalent, but counteracting reductions in plasmonic absorption and increases in FCA with increasing wavelengths.

Figure 8-4 (a) shows the reflection of glass/doped-Z2/silver stacks from both the glass side and the silver side. The ZnO layers in this experiment are exposed to 0', 2', 5', 10', and 20' argon surface treatments (ArST) before the deposition of the silver layer in order to smoothen the ZnO/silver interface (see section 3.2). Unlike the pyramid size, the pyramid shape shows a strong influence on the intensity and broadness of the SPP absorption at the ZnO/silver interface. The influence of the ZnO roughness on the reflectance can also be observed on the as-deposited samples from the silver side, where the ZnO morphology is reproduced approximately. After annealing (Figure 8-4 (b)), however, all the samples show approximately the same reflectance measured from the silver side, most probably due to a change in surface morphology and material quality.[146] Nonetheless the reflectance measured after annealing from the glass side still shows the same trends as before annealing, possibly because the ZnO/silver interface morphology remains un-changed due to the ZnO layer. The unchanged interface morphology could explain why the absorption peak intensity remains the same after annealing, while the broadness of the absorption peak is reduced for all samples after annealing, possibly because of an improvement in silver material quality.

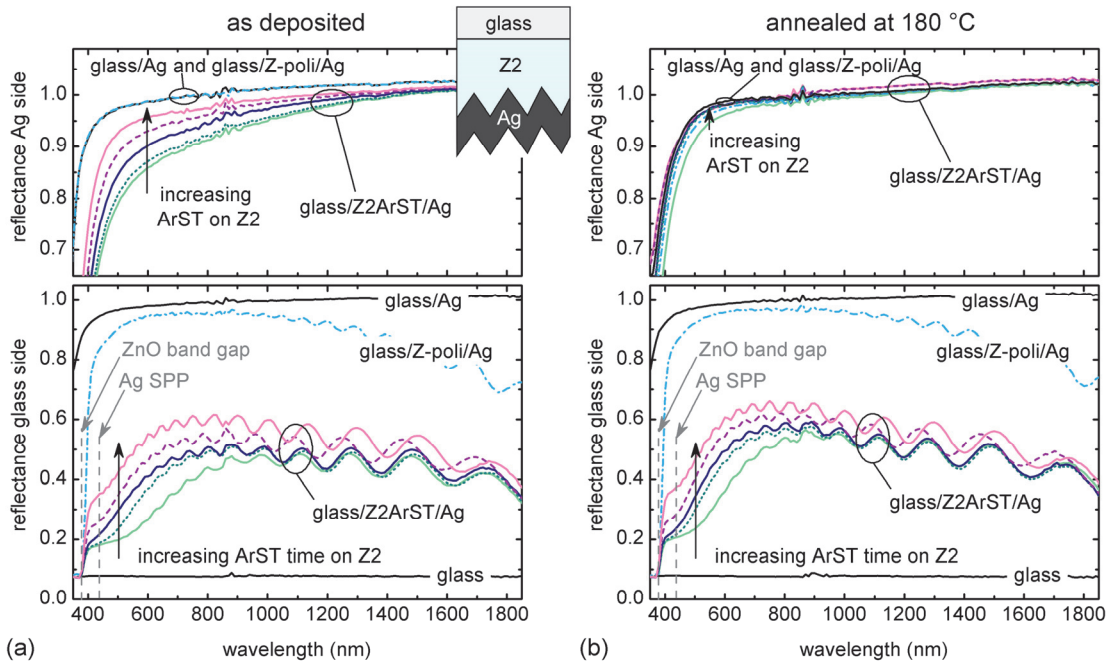

Figure 8-4: Reflectance of glass/doped-Z2/silver stacks as deposited (a) and after annealing at 180 °C (b). The reflectance measured from the glass side is shown on the bottom and the reflectance measured from the silver side is shown on the top. The Z2 layers are exposed to 0', 2', 5', 10', 20' ArST before the sputtering of the silver layer.

8.3 Conclusion

In summary, we showed that a weakly doped, rough back-ZnO electrode in combination with a dielectric bulk diffuser is an excellent back reflector for µc-Si cells. This is the standard solution in our lab and was used for all measurements presented in this report. We demonstrated that sputtered silver on the very rough back-ZnO leads to strong absorption losses and lower µc-Si EQE. We argued that such absorption losses are dependent on the silver quality, which can be influenced by deposition parameters or by subsequent annealing, and on the inclination angle of the morphology features at the interface. In the range represented by our samples, no clear dependence on the size or height of the pyramids forming the interface was observed. We showed that the EQE of a µc-Si cell with a ZnO/silver reflector can be increased by polishing the back LP-CVD ZnO electrode, which cancels the SPP absorption. The flat ZnO/silver reflector does not absorb, but it does not scatter light either and we showed that such scattering is beneficial for EQE for µc-Si cell configurations with incomplete light-scattering at the ZnO/µc-Si/ZnO interfaces. For µc-Si and Micromorph cells deposited on electrodes such as untreated LP-CVD ZnO (Z3-Z5), however, the light scattering is believed to be complete at the ZnO/Si/ZnO interfaces and it is speculated that the best back reflector for such configurations could be a polished low-FCA ZnO electrode in combination with a flat SPP-free silver layer. CMP is not believed to be a industrially valid solution, but we speculate that sufficiently flat ZnO/silver interfaces could be achieved by adapting the deposition parameters of LP-CVD ZnO.

9 Final conclusions and outlook

For a Micromorph cell in the p-i-n configuration, a rough front electrode plays a key role in maximizing the cell's conversion efficiency. Roughness at the interface between the front electrode and silicon absorber layers enhances light coupling into the cell, but also leads to non-uniformities in the material properties of the silicon layers, which deteriorates the electrical performance of the device. In order to achieve high-efficiency thin-film silicon solar cells one has therefore to fine-tune the front electrode surface morphology with respect to the trade-off between light absorption, which is favored by rough morphologies, and electrical performance, which is favored by flat morphologies. The optimum front electrode surface morphology is different for a-Si, µc-Si, and Micromorph cells and furthermore depends on many other parameters such as the deposition conditions for the silicon layers and the properties of the doped layer. For the optimization of different cell configurations, it is thus important to adjust the front electrode surface morphology according to its application. With respect to these requirements, we presented in chapter 1 a large variety of front electrode surface morphologies that can be obtained with as-grown rough LP-CVD ZnO and after post-deposition argon plasma surface treatment. In order to better understand the impact of surface morphology on solar cell performance, we correlated the morphological parameters with the light-scattering properties in transmission and reflection. We showed that common roughness parameters are not suited to describe the observed tendencies, and concluded that the inclination angles of the surface features give a more pertinent picture for application in thin-film silicon solar cells.

Whereas most of the research on thin-film silicon solar cells was based on experiments carried out on a single front electrode surface morphology, we stressed throughout this PhD thesis report the morphology dependence of nearly all the results. In chapter 4 we presented TiO_2 (produced by reactive sputtering) and p-SiO_x (produced by PECVD) as two materials that can be used to reduce reflection at the ZnO/silicon interface and so increase the current density of the solar cell. We quantified the gain with the anti-reflection layer as a function of the front ZnO surface morphology and we showed that reflection losses on a relatively flat sputtered ZnO/silicon interface can be successfully reduced by up to 7.4% at 550 nm by a single TiO_2 layer. Our work is aimed mainly at improving Micromorph cell efficiency on rough LP-CVD ZnO, where no significant gain is obtained with such anti-reflection layers; the work on this topic was therefore stopped at this point. However, when working with front electrodes with lower inclination angles (e.g. sputter-etched ZnO), when using other device structures such as triple junctions, or when introducing new light in-coupling schemes with light scattering at the back electrode, it will be of interest to continue this work on anti-reflection layers.

In chapter 5 we elucidated the material properties of mixed-phase SiO_x layers. With energy-filtered TEM, we revealed phase separation, and discovered a filamentous nano-structure in SiO_x films produced with high H_2 dilution of the precursor gas mixture. Whereas homogeneous SiO_x films can be produced with a H_2/SiH_4 precursor gas ratio of three, we showed that for

H_2/SiH_4 = 300 we obtained a $SiO_{y\sim2}$ matrix containing silicon filaments tens of nanometers long, but only a few nanometers wide. In a growth model, we proposed that the main role of hydrogen ions is to increase low-impact energy transfer from the plasma to the growing film surface (local heating), enabling $Si/SiO_{y\sim2}$ phase separation which was previously observed only after high-temperature annealing of homogenous SiO_x films. Similar to silicon films, mixed-phase SiO_x films can be doped p-type and n-type with boron and phosphorous, respectively. Phosphorous-doped filamentous SiO_x films show electrical anisotropy with in-plane conductivity five orders of magnitude lower than the transverse conductivity along the silicon filaments. Mixed-phase SiO_x films are transparent and have a low refractive index due to the $SiO_{y\sim2}$ matrix, while sufficient transverse conductivity for use in thin-film silicon solar cells is maintained by the silicon filaments. The voluntary spatial unlinking of electrical and optical material properties is a new approach in thin-film silicon solar cells and opens new possibilities to engineer material properties. Mixed-phase SiO_x is a promising material for rapid application in the PV industry, because it is fabricated with the same PECVD reactors that are used to deposit the silicon absorber layers. Within the framework of this PhD thesis, we used only the H_2 dilution to control phase separation, and the deposition rate for such films drops almost proportionally with increasing H_2. Different ways to increase the deposition rate of phase-separated filamentous SiO_x films are currently underway with promising preliminary results.

No SiO_x materials were used in the cells of our research group four years ago, but today, filamentous phosphorous-doped $SiO_{x\sim1}$ has established itself as the preferred material for use as an intermediate reflecting layer, and boron-doped $SiO_{x\sim0.5}$ has become the standard p-layer due to its enhanced transparency and shunt-quenching properties. These layers have significantly contributed to increasing the best Micromorph initial efficiency from 11.8% in 2006 (with *ex-situ* ZIR) to 13.5% in 2010 (with *in-situ* SOIR). The 13.5% efficiency was achieved with 3.1 µm thick absorber layers and resulted in a stabilized efficiency of 11.5%. With a reduced absorber layer thickness of 1.4 µm, we reached an initial efficiency of 12.7% and a stabilized efficiency of 11.3%. One of the main present limitations for these devices is that the optimum substrate morphology is different for a-Si and µc-Si cells, which necessarily leads to a trade-off in the Micromorph configuration. We proposed the fabrication of an asymmetric SOIR as a way to alleviate this trade-off and reach higher device efficiencies. We imagined an ideal device structure with as-grown rough LP-CVD ZnO as the substrate for deposition of the a-Si cell, and a smooth but not flat SOIR surface that reduces the formation of cracks during the growth of the µc-Si cell. This idea should be further investigated, especially with chemical etching with nitrogen trifluoride diluted in argon, now available in the new PECVD systems in our lab.

In the quest to increase stabilized efficiency, we were often disappointed by surprisingly high degradation rates of initially good cells on rough front electrodes and with intermediate reflecting layers. In chapter 7 we identified that, for such cells, exposure to water vapor can cause important V_{oc} losses. With lock-in thermography measurements we showed that the border regions of µc-Si cells are affected by in-diffusion of water vapor, and we also showed evidence that porous front or back electrodes and the presence of a porous intermediate reflecting layer can facilitate in-diffusion of water vapor towards the cell center, thus degrading larger border regions. Recent developments in the i-µc-Si deposition process and the use of doped SiO_x layers have moved the optimal front electrode surface towards rougher morphologies and have allowed for an increase in initial cell efficiencies. Stabilized efficiencies of these cells have so far not reached the expected levels because the water-vapor-induced degradation specially penalizes such cells. Currently, the best cell results are achieved on

smaller pyramids with lower light-scattering capability, but which lead to more stable devices. Solutions that alleviate the water-vapor-induced degradation could allow us to move towards rougher morphologies with better optical properties, and so lead to higher stabilized efficiencies.

For front electrode morphologies that do not allow for complete light scattering at the ZnO/Si/ZnO interfaces, we showed that additional light scattering at the back reflector can lead to an increase in solar cell current. However, for cell configurations with rough front electrode morphologies, light scattering and trapping are influenced mostly by the rough ZnO/Si/ZnO interfaces, and the role of the back reflector is to allow for extraction of the current, while reflecting the light with as little absorption as possible. The commonly used ZnO/silver back reflector shows good performance on relatively flat structures, but for rough ZnO/silver interfaces, we showed that the reflectivity of ZnO/silver decreases and that this decrease depends mostly on the inclination angles of the pyramids at the interface and not on their size. Throughout this work we used a thick LP-CVD ZnO layer in combination with a dielectric white sheet as a back reflector. In this combination, there are no absorption losses in the dielectric sheet, but there is free carrier absorption in the ZnO. However, this absorption is not dependent on the roughness of the solar cell and is therefore well suited for comparing a large variety of front electrode morphologies and device configurations. In order to achieve a back reflector without parasitic absorption in a rough Micromorph cell, we proposed polished, un-doped ZnO without free carrier absorption in combination with a sputtered, flat silver back reflector without surface plasmon polariton absorption.

Finally, we hope that this contribution will bring thin-film silicon PV one step further in its current competition with the well-established crystalline silicon technologies. A lot of questions must still be answered and many novel device structures and configurations remain untested. We believe that significant efficiency improvements are achievable with intensified research, and that such advances are necessary to bring thin-film silicon PV closer to the goal of providing the world with clean, cheap, and widely available energy.

Appendix A – Graphical *FF* determination of Micromorph cells

The *FF* is a difficult parameter to interpret when working with Micromorph tandem cells. On one hand, the *FF* depends on material properties that influence the carrier collection in the absorber layers, the series resistance in the electrodes, the tunneling recombination junction, etc. On the other hand, the *FF* also depends on the current matching of the sub-cells which is influenced by the illumination conditions used for the measurement and the distribution of light in the solar cell. In the Micromorph configuration, the a-Si and µc-Si cells are electrically connected in series and they are therefore operated at the same current density (*J*). To show the two *J*(*V*) curves of the sub-cells on the same graph, it is convenient to flip the curve of the µc-Si cell on the *J*-axis as proposed by T. Repmann in Appendix A of his thesis report.[147] This way of representing the *J*(*V*) curve of the a-Si top cell and the *J*(-*V*) curve of the µc-Si bottom cell allows one to graphically determine different working points of the Micromorph cell:

- At $J = 0$, the V_{oc} of the Micromorph is given by the sum of the two sub-cells' V_{oc} (red arrow).
- At the crossing of the two *J*(*V*) curves the output voltage of the Micromorph device is zero. This point corresponds to the J_{sc} of the Micromorph cell. At $J_{sc\_Micromorph}$ as shown in Figure A-1, the a-Si cell is in forward bias and the µc-Si cell is in reverse bias conditions.

For any value of *J* in the interval $J_{sc\_Micromorph} < J < 0$, a rectangle can be drawn with one side lying on the *V*-axis and one corner on each of the *J*(*V*) curves (dashed area). The rectangle with the largest area represents the maximum power output conditions (J_{mp}, V_{mp}). Similarly a rectangle can be drawn with the V_{oc} and J_{sc} of the Micromorph cell (dotted area). The ratio of the areas of the two rectangles $(J_{mp} \times V_{mp})/(J_{sc} \times V_{oc})$ is the graphical representation of the Micromorph's *FF*.

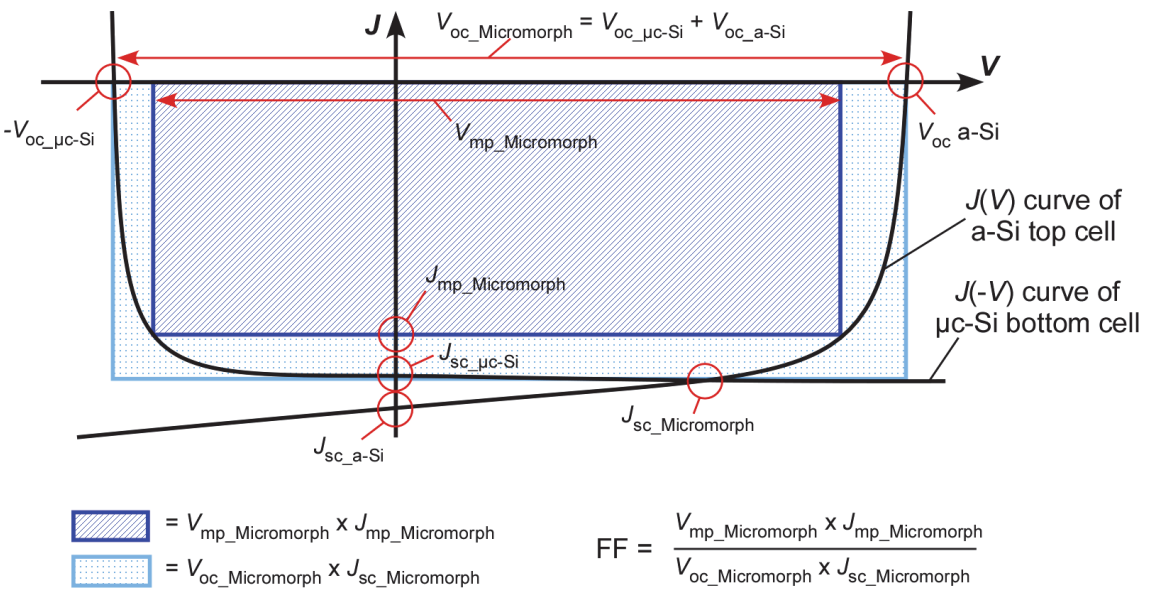

Figure A-1: *J*(*V*) curves of a-Si and µc-Si sub-cells in a slightly bottom-limited Micromorph cell.

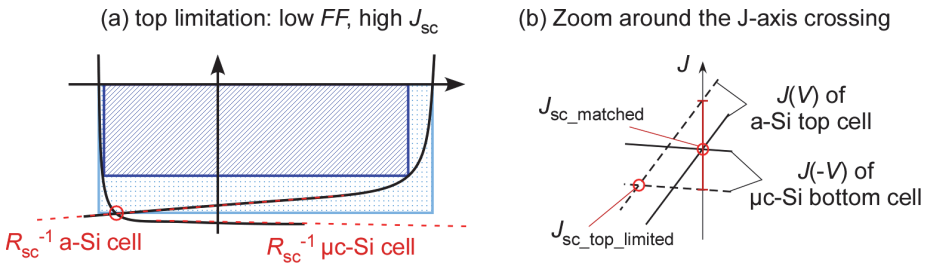

Figure A-2: (a) *J*(*V*) curves of sub-cells in a top-limited Micromorph cell. The dashed red lines indicate the slope of the *J*(*V*) curves around the *J*-intercept, expressed by the R_{sc}^{-1} value. (b) Zoom of *J*(*V*) curves around the *J*-intercept. The solid lines represent a current-matched Micromorph cell and the dashed lines a top-limited Micromorph cell.

Figure A-2 (a) illustrates that the *FF* of a Micromorph cell is dominated by the current-limiting cell (the cell that is in reverse bias at $J_{sc\_Micromorph}$); more precisely, by the slope of its *J*(*V*) curve at *V* = 0. This slope is commonly expressed by R_{sc}^{-1}, the inverse of the short-circuit resistance. Figure A-2 (b) shows a zoom around the *J*-axis of two cells with the same summed current densities. A current-matched cell is represented by the solid lines and a slightly top-limited cell by the dashed lines. If the R_{sc}^{-1} is higher in the a-Si than in the µc-Si cell, as illustrated, then the highest $J_{sc\_Micromorph}$ is obtained in slightly top-limiting conditions.

With respect to the *FF*, D. Dominé showed in chapter 7.2 of his thesis report,[87] that for state-of-the-art a-Si and µc-Si cells the highest stabilized Micromorph efficiency can be achieved under slightly bottom-limited conditions. This is because the loss in J_{sc} by a slight mismatch can be compensated by a gain in *FF*, which is due to a low R_{sc}^{-1} value of the µc-Si cell. Figure A-3 illustrates this behavior graphically.

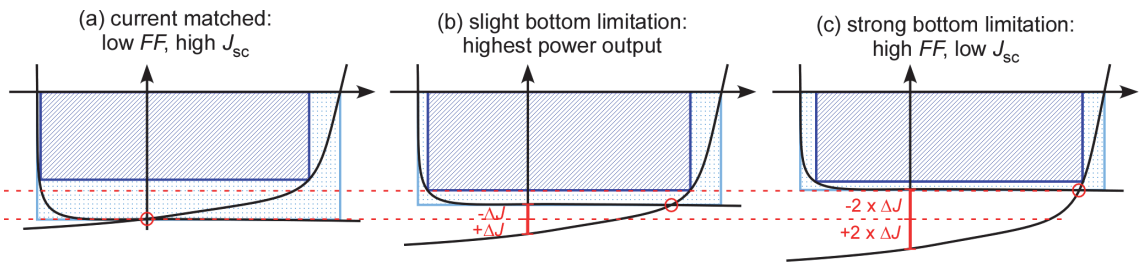

Figure A-3: Graphical representation of *FF*, J_{sc}, and power output in a Micromorph cell with different matching conditions. The dotted lines are guides to the eyes. (a) A current-matched Micromorph cell, where the *FF* is mostly influenced by the high R_{sc}^{-1} of the a-Si cell (especially valid in the stabilized state). (b) A slightly bottom-limited cell, with the same summed current density as in (a). These conditions lead to a lower J_{sc}, but a higher *FF* resulting in an increase in output power. (c) A strongly bottom-limited cell, where an increased gain in *FF* cannot any more compensate for the loss in J_{sc}, resulting in a reduced power output. Under such strongly mismatched conditions, the *FF* can become significantly higher than the *FF* of the individual sub-cells.

In summary, the graphical representation of the *FF* and the power output of tandem cells gives a way to understand common tendencies observed when working with Micromorph cells. It shows that the limiting cell has a bigger influence on the *FF*, that the highest $J_{sc\_Micromorph}$ is obtained when the sub-cell with the higher R_{sc}^{-1} is in reverse bias, and that the highest power output is obtained when the sub-cell with the lower R_{sc}^{-1} is in reverse bias at $J_{sc\_Micromorph}$.

Appendix B – Influence of local bad diodes on the overall V_{oc}

Similar to the graphical approach used in Appendix A to understand the *FF* of Micromorph cells, we show here a graphical approach to understand the influence of local bad diodes on the V_{oc}. In spatially inhomogeneous solar cells, there are different $J(V)$ behaviors electrically connected in parallel. Due to the parallel connection, these different behaviors are operated at the same voltage and for a graphical representation, in this case it is convenient to flip one of the curves around the V-axis. Figure B-1 shows the $J(V)$ curve of a good diode (low J_{01}, high local V_{oc}) and the $-J(V)$ curve of a bad diode (high J_{02}, low local V_{oc}).

Thin-film silicon solar cells deposited on rough LP-CVD ZnO often contain less dense regions (cracks) in the silicon absorber layer which are electrically characterized by bad-diode behavior. They negatively influence cell performance as demonstrated in detail by Python et al.[64-66] The SEM image shows that these bad diodes have a surface significantly smaller than the good diodes and to find the V_{oc} that results from these two electrical behaviors one has therefore to plot the $I(V)$ curves (scaling of the $-J(V)$ curve of the bad diode in the direction of the *J*-axis by the factor 1/20 in this example) corresponding to the respective surfaces of good and bad diodes. The crossing of the dashed red line with the black line represents the V_{oc} of a single junction device with two different diode behaviors.

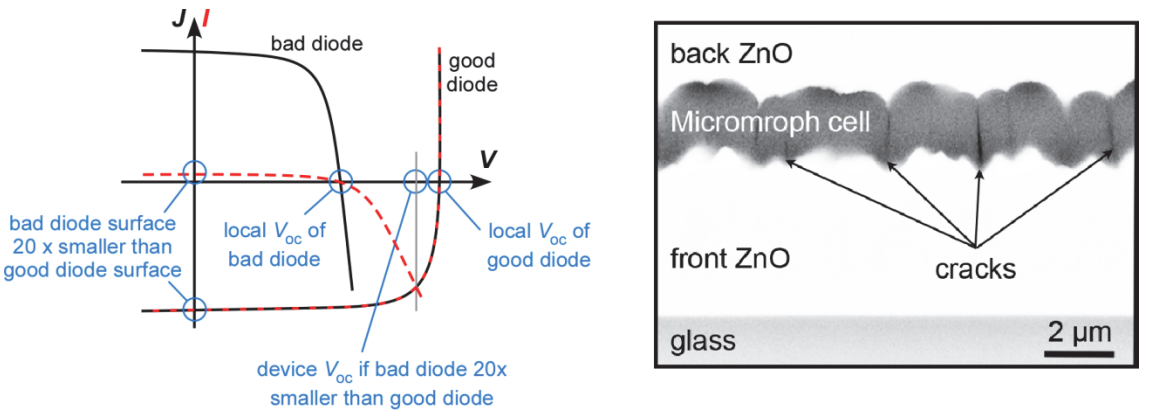

Figure B-1: (Left) $J(V)$ curves (black) and $I(V)$ curves (red) of good diodes (high local V_{oc}) and bad diodes (low local V_{oc}). The curves of the bad diodes are flipped around the V-axis. The grey line indicates the V_{oc} for a device for which the surface of the good diode is 20 times larger than the surface of the bad diode. (Right) SEM cross-section of a Micromorph cell without an IRL. The cracks in the valleys of the ZnO electrically behave as bad diodes.

This approach is a strong simplification of reality since there are not only two different $J(V)$ characteristics in spatially non-uniform thin-film silicon solar cells, but a broad distribution of $J(V)$ characteristics. Nevertheless this graphical representation can help one to understand the influence of spatially separated $J(V)$ characteristics on the overall device $J(V)$. Similar to Appendix A, the *FF* of the shunt-influenced single-junction device can also be graphically represented by drawing rectangles with V_{oc}, I_{sc}, V_{mp}, I_{mp} (first proposed for this representation by M. Boccard).

Abbreviations and Symbols

Abbreviation used to describe the surface morphology of the front ZnO electrode:
Z5-Ar20’ = 5 µm thick ZnO after 20’ plasma treatment at 30mTorr

Abbreviation used to describe the device structure of a Micromorph cell:
(Z5-Ar20’,180,80,2.5) = (Z5-Ar20’ front ZnO, 180 nm a-Si, 80nm SOIR, 2.5 µm µc-Si)

General Abbreviations:

AFM	atomic force microscopy
ARL	anti-reflection layer
a-Si	amorphous silicon
CVD	chemical vapor deposition
EFTEM	energy filtered TEM
IRL	intermediate reflecting layer
LP-CVD	low pressure CVD
µc-Si	microcrystalline silicon
PECVD	plasma-enhanced CVD
SEM	scanning electron microscopy
SOIR	silicon oxide based intermediate reflector
TEM	transmission electron microscopy

Symbols:

V_{oc}	open-circuit voltage
J_{sc}	short-circuit current density
I_{sc}	short-circuit current
FF	fill factor
n	refractive index
R_c	Raman crystalline fraction
R_s	Series resistance
α	absorption coefficient
σ	dark conductivity
η	solar cell conversion efficiency

References

Publications as first Author:

1 **Buehlmann P., Billet A., Bailat J. & Ballif C.** *Anti-reflection layer at the TCO/Si interface for high efficiency thin-film solar cells deposited on rough lp-cvd front ZnO.* in Proceedings of 22nd EU-PVSEC, 2182–2185, 2007, Milan, Italy.

2 **Buehlmann P., Bailat J., Dominé D. *et al.*** *In situ silicon oxide based intermediate reflector for thin-film silicon micromorph solar cells*. Appl Phys Lett 91, 143505, (2007).

3 **Buehlmann P., Bailat J., Feltrin A. & Ballif C.** *Conducting two-phase silicon oxide layers for thin-film silicon solar cells*. Mater. Res. Soc. Symp. Proc. 1123, P03-09, (2009).

4 **Cuony P., Marending M., Alexander D. T. L. *et al.*** *Mixed-phase p-type silicon oxide containing silicon nanocrystals and its role in thin-film silicon solar cells*. Appl Phys Lett 97, 213502, (2010).

5 **Cuony P., Alexander D. T. L., Löfgren L. *et al.*** *Mixed phase silicon oxide layers for thin-film silicon solar cells*. Mater. Res. Soc. Symp. Proc. 1321, (2011).

6 **Cuony P., Alexander D. T. L., Perez-Wurfl I. *et al.*** *Silicon filaments in silicon oxide for next-generation photovoltaics*. (submitted for publication).

7 **Cuony P., Dominé D., Niquille X. *et al.*** *H_2O-induced Voc degradation in microcrystalline silicon solar cells*. (to be published).

Patents:

8 **Dominé D., Cuony P. & Bailat J.** *Patent WO2010/057907 A3: Multiple-junction photoelectric device and its prodution process*. (2010).

9 **Cuony P., Despeisse M., Parascandolo G. & Ballif C.** *Patent filed but not yet published: Multiple-junction photoelectric device and its prodution process*. (2010).

Publications as Co-Author:

10 **Dominé D., Buehlmann P., Bailat J. *et al.*** *Optical management in high-efficiency thin-film silicon micromorph solar cells with a silicon oxide based intermediate reflector*. Physica Status Solidi (Rapid Reasarch Letters) 2, 163–165, (2008).

11 **Dominé D., Buehlmann P., Bailat J. *et al.*** *High-efficiency micromorph silicon solar cells with in-situ intermediate reflector deposited on various rough LPCVD ZnO.* in Proceedings of 23rd EU-PVSEC, 2008, Valencia, Spain.

12 **Meillaud F., Feltrin A., Bailat J. *et al.*** *Micromorph tandem solar cells grown at high rate with in-situ intermediate reflector in industrial KAI PECVD reactors.* in Proceedings of 33rd IEEE PVSC, 258–261, 2008, San Diego, USA.

13 **Meillaud F., Feltrin A., Bugnon G. *et al.*** *Micromorph cells grown at high rate with in-situ intermediate reflector in industrial KAI PECVD reactors.* in Proceedings of 23rd EU-PVSEC, 2396–2399, 2008, Valencia, Spain.

14 **Despeisse M., Ballif C., Feltrin A. *et al.*** *Research and developments in thin film silicon photovoltaics.* in Proceedings of SPIE Optics and Photonics Conference, 2009, San Diego.

15 **Meillaud F., Feltrin A., Dominé D. *et al.*** *Limiting factors in the fabrication of microcrystalline silicon solar cells and microcrystalline/amorphous ('micromorph') tandems*. Philos Mag 89, 2599–2621, (2009).

16 **Battaglia C., Söderström K., Escarre Palou J. *et al.*** *Efficient light management scheme for thin film silicon solar cells via transparent random nanostructures fabricated by nanoimprinting*. Appl Phys Lett 96, 213504, (2010).

17 **Boccard M., Cuony P., Battaglia C. *et al.*** *Unlinking absorption and haze in thin film silicon solar cells front electrodes*. physica status solidi (RRL) - Rapid Research Letters 4, 326–328, (2010).

18 **Boccard M., Cuony P., Söderström K. *et al.*** *Transparent conducting oxide electrodes requirements for high efficiency micromorph solar cells* in Proceedings of 25th EU-PVSEC and 5th WC-PEC, 2010,

19 **Despeisse M., Boccard M., Bugnon G. *et al.*** *Low-conductivity doped layers for improved performance of thin film silicon solar cells on highly textured substrate.* in Proceedings of 25th EU-PVSEC and 05th WC-PEC Conference, 2010, Valencia, Spain.

20 **Despeisse M., Bugnon G., Feltrin A. *et al.*** *Resistive interlayer for improved performance of thin film silicon solar cells on highly textured substrate*. Appl Phys Lett 96, (2010).

21 **Söderström T., Dominé D., Feltrin A. *et al.*** *ZnO Transparent conductive oxide for thin film silicon solar cells.* in Proceedings of SPIE, 3–12, 2010, San Fransisco, USA.

22 **Boccard M., Cuony P., Despeisse M. *et al.*** *Substrate dependent stability and interplay between optical and electrical properties in μc-Si:H single junction solar cells*. Sol Energ Mat Sol C 95, 195–198, (2011).

23 **Meillaud F., Feltrin A., Despeisse M. *et al.*** *Realization of high efficiency micromorph tandem silicon solar cells on glass and plastic substrates: Issues and potential*. Sol Energ Mat Sol C 95, 127–130, (2011).

24 **Despeisse M., Battaglia C., Boccard M. *et al.*** *Optimization of thin film silicon solar cells on highly textured substrates*. physica status solidi (a) 208, 1863–1868, (2011).

25 **Boccard M., Söderström T., Cuony P. *et al.*** *Optimization of ZnO front electrodes for high efficiency Micromorph thin film Si solar cells* (to be published).

Other Publications:

26 **Hermann W. A.** *Quantifying global exergy resources*. Energy 31, 1685–1702, (2006).

27 European Photovoltaic Industry Association. *Solar Generation 6.* (2011).

28 International Energy Agency. *Technology Roadmap.* (2010).

29 European Photovoltaic Industry Association. *Global Market Outlook for Photovoltaics until 2015.* (2011).

30 European Photovoltaic Industry Association. *Solar Europe industry initiative - implementation plan 2010-2012.* (2010).

31 **Meier J., Dubail S., Flückiger R. *et al.*** *Intrinsic Microcrystalline Silicon (µc-Si:H) - a Promising New Thin Film Solar Cell Material.* in Proceedings of 1st WC-PEC, 409–412, 1994,

32 **Shah A.** *Thin-film silicon solar cells.* ISBN 9781420066746 (EPFL Press, 2010).

33 SunShine Optical simulator software, v.1.0, by University of Ljubljana (2006).

34 **Iida H., Mishuku T., Ito A. & Hayashi Y.** *The Structure of Natively Textured Sno2 Film and Its Application to an Optical Confinement-Type a-Si-H Solar-Cell*. Ieee T Electron Dev 34, 271-276, (1987).

35 **Meier J., Spitznagel J., Kroll U. *et al.*** *High-efficiency amorphous and "micromorph" silicon solar cells*. Proceedings of 3rd World Conference on Photovoltaic Energy Conversion, Vols A-C, 2801-2805, (2003).

36 **Faÿ S., Feitknecht L., Schlüchter R. *et al.*** *Rough ZnO layers by LP-CVD process and their effect in improving performances of amorphous and microcrystalline silicon solar cells*. Sol Energ Mat Sol C 90, 2960–2967, (2006).

37 **Kluth O., Rech B., Houben L. *et al.*** *Texture etched ZnO : Al coated glass substrates for silicon based thin film solar cells*. Thin Solid Films 351, 247-253, (1999).

38 **Ma W., Aoyama S., Okamoto H. & Hamakawa Y.** *A study of interface properties in a-Si solar cells with mu c-Si(C)*. Sol Energ Mat Sol C 41-2, 453-463, (1996).

39 **Tawada Y., Tsuge K., Kondo M. *et al.*** *Properties and Structure of Alpha-Sic-H for High-Efficiency Alpha-Si Solar-Cell*. J Appl Phys 53, 5273-5281, (1982).

40 **Lim K. S., Konagai M. & Takahashi K.** *A Novel Structure, High Conversion Efficiency P-Sic Graded P-Sic/I-Si/N-Si/Metal Substrate-Type Amorphous-Silicon Solar-Cell*. J Appl Phys 56, 538-542, (1984).

41 **Platz R., Fischer D., Hof C. *et al.*** *H2-Dilution vs. Buffer Layers for Increased Voc.* in Proceedings of Mater. Res. Soc. Symp. Proc., 51, 1996,

42 **Staebler D. L. & Wronski C. R.** *Reversible Conductivity Changes in Discharge-Produced Amorphous Si*. Appl Phys Lett 31, 292–294, (1977).

43 **Platz R., Wagner S., Hof C. *et al.*** *Influence of excitation frequency, temperature, and hydrogen dilution on the stability of plasma enhanced chemical vapor deposited a-Si:H*. J Appl Phys 84, 3949-3953, (1998).

44 **Vaucher N. P., Rech B., Fischer D. *et al.*** *Controlled nucleation of thin microcrystalline layers for the recombination junction in a-Si stacked cells*. Sol Energ Mat Sol C 49, 27-33, (1997).

45 **Meier J., Fluckiger R., Keppner H. & Shah A.** *Complete Microcrystalline P-I-N Solar-Cell - Crystalline or Amorphous Cell Behavior*. Appl Phys Lett 65, 860-862, (1994).

46 **Torres P., Meier J., Fluckiger R. *et al.*** *Device grade microcrystalline silicon owing to reduced oxygen contamination*. Appl Phys Lett 69, 1373-1375, (1996).

47 **Vetterl O., Finger F., Carius R. *et al.*** *Intrinsic microcrystalline silicon: A new material for photovoltaics*. Sol Energ Mat Sol C 62, 97-108, (2000).

48 **Van Den Donker M. N., Klein S., Rech B. *et al.*** *Microcrystalline silicon solar cells with an open-circuit voltage above 600 mV*. Appl Phys Lett 90, (2007).

49 **Kothandaraman C., Tonon T., Huang C. & Delahoy A. E.** *Improvement of a-Si:H P-I-N devices using zinc oxide based back-reflectors*. Mater. Res. Soc. Symp. Proc. 219, 475–480, (1991).

50 **Meier J., Kroll U., Spitznagel J. *et al.*** *Progress in up-scaling of thin film silicon solar cells by large-area PECVD KAI systems.* in Proceedings of 31st IEEE PSC, 2005, 1464-1467,

51 **Deckman H. W., Wronski C. R., Witzke H. & Yablonovitch E.** *Optically Enhanced Amorphous-Silicon Solar-Cells*. Appl Phys Lett 42, 968-970, (1983).

52 **Eisele C., Nebel C. E. & Stutzmann M.** *Periodic light coupler gratings in amorphous thin film solar cells*. J Appl Phys 89, 7722-7726, (2001).

53 **Senoussaoui N., Krause M., Muller J. *et al.*** *Thin-film solar cells with periodic grating coupler*. Thin Solid Films 451, 397-401, (2004).

54 **Sai H., Kanamori Y. & Kondo M.** *Flattened light-scattering substrate in thin film silicon solar cells for improved infrared response*. Appl Phys Lett 98, (2011).

55 **Naughton M. J., Kempa K., Ren Z. F. *et al.*** *Efficient nanocoax-based solar cells*. Phys Status Solidi-R 4, 181-183, (2010).

56 **Vanecek M., Neykova N., Babchenko O. *et al.*** *New 3-dimensional nanostructured thin film silicon solar cells.* in Proceedings of 25th EU-PVSEC, 2010, Valencia, Spain.

57 **Faÿ S., Steinhauser J., Nicolay S. & Ballif C.** *Polycrystalline ZnO: B grown by LPCVD as TCO for thin film silicon solar cells*. Thin Solid Films 518, 2961–2966, (2010).

58 **Benagli S., Borrello D., Vallat-Sauvain E. *et al.*** *High-efficiency amorphous silicon devices on LPCVD-ZnO TCO prepared in industrial KAI-M R&D reactor.* in Proceedings of 24th EU-PVSEC Conference, 2009, Valencia, Spain.

59 **Bailat J., Fesquet L., Ohran J.-B. *et al.*** *Recent developments of high-efficiency Micromorph tandem cells in KAI-M PECVD reactors.* in Proceedings of 25th EU-PVSEC Conference, 2010, Valencia, Spain.

60 **Ichikawa Y., Fujikake S., Ohta H. *et al.*** *12% two-stacked a-Si:H tandem cells with a new p-layer structure.* in Proceedings of Photovoltaic Specialists Conference, 1991., Conference Record of the Twenty Second IEEE, 1296-1301 vol.1292, 1991,

61 **Sakai H., Yoshida T., Hama T. & Ichikawa Y.** *Effects of Surface-Morphology of Transparent Electrode on the Open-Circuit Voltage in a-Si-H Solar-Cells*. Jpn J Appl Phys 29, 630–635, (1990).

62 **Nasuno Y., Kondo M. & Matsuda A.** *Effects of substrate surface morphology on microcrystalline silicon solar cells*. Jpn J Appl Phys 2 40, L303–L305, (2001).

63 **Bailat J., Vallat-Sauvain E., Feitknecht L. *et al.*** *Influence of substrate on the microstructure of microcrystalline silicon layers and cells*. J Non-Cryst Solids 299, 1219-1223, (2002).

64 **Python M., Vallat-Sauvain E., Bailat J. *et al.*** *Relation between substrate surface morphology and microcrystalline silicon solar cell performance*. J Non-Cryst Solids 354, 2258–2262, (2008).

65 **Python M., Madani O., Domine D. *et al.*** *Influence of the substrate geometrical parameters on microcrystalline silicon growth for thin-film solar cells*. Sol Energ Mat Sol C 93, 1714–1720, (2009).

66 **Python M., Dominé D., Söderström T. *et al.*** *Microcrystalline silicon solar cells: effect of substrate temperature on cracks and their role in post-oxidation*. Progress in Photovoltaics: Research and Applications 18, 491–499, (2010).

67 **Bailat J., Domine D., Schluchter R. *et al.*** *High-efficiency p-i-n microcrystalline and micromorph thin film silicon solar cells deposited on LPCVD ZnO coated glass substrates.* in Proceedings of 4th WC-PEC, 1533–1536, 2006, Hawaii, USA.

68 **Guo L. H., Kondo M., Fukawa M. *et al.*** *High rate deposition of microcrystalline silicon using conventional plasma-enhanced chemical vapor deposition*. Jpn J Appl Phys 2 37, L1116-L1118, (1998).

69 **Gordijn A., Francke J., Hodakova L. *et al.*** *Influence of pressure and plasma potential on high growth rate microcrystalline silicon grown by VHFPECVD*. Amorphous and Nanocrystalline Silicon Science and Technology-2005 862, 87-92, (2005).

70 **Bugnon G., Feltrin A., Meillaud F. *et al.*** *Influence of pressure and silane depletion on microcrystalline silicon material quality and solar cell performance*. J Appl Phys 105, -, (2009).

71 **Niikura C., Kondo M. & Matsuda A.** *High rate growth of device-grade microcrystalline silicon films at 8 nm/s*. Sol Energ Mat Sol C 90, 3223-3231, (2006).

72 **Kunii T., Murata K., Matsumoto M. *et al.*** *Efficient Production Technology for Microcrystalline Silicon Solar Cells Using a Localized Plasma Confinement (LPC) CVD Method*. Pvsc: 2008 33rd Ieee Photovoltaic Specialists Conference, Vols 1-4, 1045-1049, (2008).

73 **Gordijn A., Schicho S., Muthmann S. *et al.*** *Significantly decreased production times for a-Si/mu c-Si tandem cells on texture-etched ZnO:Al*. Physica Status Solidi a-Applications and Materials Science 207, 678-681, (2010).

74 **Knauss H., Salabas E. L., Fecioru M. *et al.*** *Reduction of cell thickness for industrial micromorph tandem modules.* in Proceedings of 25th EU-PVSEC and 5th WC-PEC, 2010,

75 **Steinhauser J.** *Low pressure chemical vapor deposited Zinc Oxide for thin film silicon solar cells.* PhD thesis, University of Neuchâtel, (2008).

76 **Howling A. A., Derendinger L., Sansonnens L. *et al.*** *Probe measurements of plasma potential nonuniformity due to edge asymmetry in large-area radio-frequency reactors: The telegraph effect*. J Appl Phys 97, (2005).

77 **Szczyrbowski J., Brauer G., Ruske M. *et al.*** *Some properties of TiO2 layers prepared by medium frequency reactive sputtering*. Surf Coat Tech 112, 261–266, (1999).

78 **Fujibayashi T., Matsui T. & Kondo M.** *Improvement in quantum efficiency of thin film Si solar cells due to the suppression of optical reflectance at transparent conducting oxide/Si interface by TiO2/ZnO antireflection coating*. Appl Phys Lett 88, (2006).

79 **Droz C., Vallat-Sauvain E., Bailat J. *et al.*** *Relationship between Raman crystallinity and open-circuit voltage in microcrystalline silicon solar cells*. Sol Energ Mat Sol C 81, 61–71, (2004).

80 **Horcas I., Fernandez R., Gomez-Rodriguez J. M. *et al.*** *WSXM: A software for scanning probe microscopy and a tool for nanotechnology*. Rev Sci Instrum 78, (2007).

81 **Schamm S., Bonafos C., Coffin H. *et al.*** *Imaging Si nanoparticles embedded in SiO_2 layers by (S)TEM-EELS*. Ultramicroscopy 108, 346–357, (2008).

82 **Schaffer B., Grogger W. & Kothleitner G.** *Automated spatial drift correction for EFTEM image series*. Ultramicroscopy 102, 27–36, (2004).

83 **Springer J., Poruba A. & Vanecek M.** *Improved three-dimensional optical model for thin-film silicon solar cells*. J Appl Phys 96, 5329–5337, (2004).

84 **Domine D., Haug F. J., Battaglia C. & Ballif C.** *Modeling of light scattering from micro- and nanotextured surfaces (vol 107, 044504, 2010)*. J Appl Phys 107, (2010).

85 **Oh B. Y., Lee W. K., Kim Y. H. & Seo D. S.** *Zinc oxide nanolevel surface transformation for liquid crystal orientation by ion bombardment*. J Appl Phys 105, (2009).

86 **Campbell P.** *Light Trapping in Textured Solar-Cells*. Sol Energ Mater 21, 165-172, (1990).

87 **Domine D.** *The role of front electrodes and intermediate reflectors in the optoelectronic properties of high-efficiency micromorph solar cells.* PhD thesis, University of Neuchâtel, (2009).

88 **Yablonovitch E.** *Statistical Ray Optics*. J Opt Soc Am 72, 899–907, (1982).

89 **Han S. E. & Chen G.** *Toward the Lambertian Limit of Light Trapping in Thin Nanostructured Silicon Solar Cells*. Nano Letters 10, 4692–4696, (2010).

90 **Rockstuhl C., Fahr S., Bittkau K. *et al.*** *Comparison and optimization of randomly textured surfaces in thin-film solar cells*. Opt Express 18, A335–A342, (2010).

91 **Parascandolo G., Bartlome R., Bugnon G. *et al.*** *Impact of secondary gas-phase reactions on microcrystalline silicon solar cells deposited at high rate*. Appl Phys Lett 96, (2010).

92 **Natsuhara H., Ohashi T., Ogawa S. *et al.*** *Hydrogen-radical durability of TiO2 thin films for protecting transparent conducting oxide for Si thin film solar cells*. Thin Solid Films 430, 253–256, (2003).

93 **Matsui T., Fujibayashi T., Sato A. *et al.*** *Improved spectral response of silicon thin film solar cells by TiO2-ZnO antireflecting inter-bilayer at TCO/Si interface*. 20th European Photovoltaic Solar Energy Conference, 2005, Barcelona, Spain, (2005).

94 **Yamada N., Hitosugi T., Kasai J. *et al.*** *Direct growth of transparent conducting Nb-doped anatase TiO2 polycrystalline films on glass*. J Appl Phys 105, (2009).

95 **Marending M.** *Boron-doped SiOx layers containing silicon nanocrystals for the use as p-layer in microcrystalline p-i-n thin film silicon solar cells.* Master thesis, EPFL, (2010).

96 **Atwater H. A. & Polman A.** *Plasmonics for improved photovoltaic devices*. Nature Materials 9, 865–865, (2010).

97 **Flückiger R., Meier J., Shah A. *et al.*** *Structural, Optical and Electrical Properties of <p> μc-Si:H Very Thin Films Deposited by the VHF-GD Technique*. MRS Proceedings 336, 511, (1994).

98 **Saleh R. & Nickel N. H.** *Raman spectroscopy of B-doped microcrystalline silicon films*. Thin Solid Films 427, 266–269, (2003).

99 **Lucovsky G., Yang J., Chao S. S. *et al.*** *Oxygen-Bonding Environments in Glow-Discharge Deposited Amorphous Silicon-Hydrogen Alloy-Films*. Phys Rev B 28, 3225–3233, (1983).

100 **Iftiquar S. M.** *The roles of deposition pressure and rf power in opto-electronic properties of a-SiO : H films*. J Phys D Appl Phys 31, 1630–1641, (1998).

101 **He L. N., Wang D. M. & Hasegawa S.** *Study of plasma-deposited amorphous SiO_x:H (0≤x≤2.0) films using infrared spectroscopy*. J Non-Cryst Solids 261, 67–71, (2000).

102 **Smith F. W. & Yin Z.** *Free energy model for bonding in a-Si alloys*. J Non-Cryst Solids 137–138, 871–874, (1991).

103 **Iacona F., Bongiorno C., Spinella C. *et al.*** *Formation and evolution of luminescent Si nanoclusters produced by thermal annealing of SiOx films*. J Appl Phys 95, 3723–3732, (2004).

104 **Nicotra G., Lombardo S., Spinella C. *et al.*** *Observation of the nucleation kinetics of Si quantum dots on SiO_2 by energy filtered transmission electron microscopy*. Appl Surf Sci 205, 304–308, (2003).

105 **Tsai C. C., Knights J. C., Chang G. & Wacker B.** *Film Formation Mechanisms in the Plasma Deposition of Hydrogenated Amorphous-Silicon*. J Appl Phys 59, 2998-3001, (1986).

106 **Parratt L. G.** *Structure of Thin Evaporated Copper Films by Total Reflection of X-Rays*. Phys Rev 99, 1635–1635, (1955).

107 **Krumrey M., Hoffmann M., Ulm G. *et al.*** *Thickness determination for SiO2 films on Si by X-ray reflectometry at the Si K edge*. Thin Solid Films 459, 241–244, (2004).

108 **Iacona F., Franzo G. & Spinella C.** *Correlation between luminescence and structural properties of Si nanocrystals*. J Appl Phys 87, 1295–1303, (2000).

109 **Boninelli S., Iacona F., Franzo G. *et al.*** *Thermal evolution and photoluminescence properties of nanometric Si layers*. Nanotechnology 16, 3012–3016, (2005).

110 **Matsuda A.** *Growth mechanism of microcrystalline silicon obtained from reactive plasmas*. Thin Solid Films 337, 1–6, (1999).

111 **Sriraman S., Agarwal S., Aydil E. S. & Maroudas D.** *Mechanism of hydrogen-induced crystallization of amorphous silicon*. Nature 418, 62–65, (2002).

112 **Fujiwara H., Kondo M. & Matsuda A.** *Microcrystalline silicon nucleation sites in the sub-surface of hydrogenated amorphous silicon*. Surf Sci 497, 333–340, (2002).

113 **Nienhaus H., Kravets V., Koutouzov S. *et al.*** *Quantum size effect of valence band plasmon energies in Si and SnO_x nanoparticles*. J Vac Sci Technol B 24, 1156–1161, (2006).

114 **Conibeer G., Green M., Cho E. C. *et al.*** *Silicon quantum dot nanostructures for tandem photovoltaic cells*. Thin Solid Films 516, 6748–6756, (2008).

115 **Fujii M., Mimura A., Hayashi S. & Yamamoto K.** *Photoluminescence from Si nanocrystals dispersed in phosphosilicate glass thin films: Improvement of photoluminescence efficiency*. Appl Phys Lett 75, 184–186, (1999).

116 **Hao X. J., Cho E. C., Scarder G. *et al.*** *Phosphorus-doped silicon quantum dots for all-silicon quantum dot tandem solar cells*. Sol Energ Mat Sol C 93, 1524–1530, (2009).

117 **Conibeer G.** *Third-generation photovoltaics*. Mater Today 10, 42–50, (2007).

118 **Perez-Wurfl I., Hao X. J., Gentle A. *et al.*** *Si nanocrystal p-i-n diodes fabricated on quartz substrates for third generation solar cell applications*. Appl Phys Lett 95, 153506, (2009).

119 **D. Fischer, S. Dubail, Selvan J. a. A. *et al.*** *The ''micromorph'' solar cell: Extending a-Si:H technology towards thin film crystalline silicon*. 25th IEEE PVSEC, 1053–1056, (1996).

120 **Yamamoto K., Nakajima A., Yoshimi M. *et al.*** *Novel hybrid thin film silicon solar cell and module*. 3rd WC-PEC, 2789–2792, (2003).

121 **Yamamoto K., Nakajima A., Yoshimi M. *et al.*** *A high efficiency thin film silicon solar cell and module*. Sol Energy 77, 939–949, (2004).

122 **Sasaki T., Koi Y., Yamamoto K. *et al.*** *Patent WO2005/011001: Stacked Photoelectric Converter*. (2004).

123 **Lambertz A., Dasgupta A., Reetz W. *et al.*** *Micricrystalline silicon oxide as intermediate reflector for thin film silicon solar cells.* in Proceedings of 22nd EU-PVSEC, 1839–1842, 2007, Milan, Italy.

124 **Castens L., Bailat J., Benagli S. *et al.*** *Advanced light management in Micromorph solar cells*. Energy Procedia 2, 35–39, (2010).

125 **Yan B., Sivec L., Yue G. *et al.*** *Effect of dual-function nano-structured silicon oxide thin film on multi-junction solar cells.* in Proceedings of 37th IEEE PV-SC, 2011,

126 **Chung J. W., Lee J. E., Jang J. H. *et al.*** *THE PROPERTIES OF n-mu c-SiO:H INTER-LAYERS FOR THIN-FILM SILICON TANDEM SOLAR CELLS*. 2009 34th Ieee Photovoltaic Specialists Conference, Vols 1-3, 369-372, (2009).

127 **Delli Veneri P., Mercaldo L. V., Usatii I. *et al.*** *Doped silicon nitride as intermediate reflector in micromorph tandem solar cells.* in Proceedings of 23th EU-PVSEC, 2008, Valencia, ES.

128 **Bielawny A., Upping J., Miclea P. T. *et al.*** *3D photonic crystal intermediate reflector for micromorph thin-film tandem solar cell*. Physica Status Solidi a-Applications and Materials Science 205, 2796-2810, (2008).

129 **Losurdo M., Giangregorio M. M., Capezzuto P. *et al.*** *Dielectric function of nanocrystalline silicon with few nanometers (< 3 nm) grain size*. Appl Phys Lett 82, 2993-2995, (2003).

130 **Pingate N., Yotsaksri D. & Sichanugrist P.** *Microcrystalline SiO and its application to solar cell*. Conference Record of the 2006 IEEE 4th World Conference on Photovoltaic Energy Conversion, 1507, (2006).

131 **Krajangsang T., Yunaz I. A., Miyajima S. & Konagai M.** *Effect of p-μc-$Si_{1-x}O_x$:H layer on performance of hetero-junction microcrystalline silicon solar cells*. Current Applied Physics 10, 357–360, (2010).

132 **Krajangsang T., Kasashima S., Yunaz I. A. *et al.*** *Hetero-Junction Microcrystalline Silicon Solar Cells with Wide-Gap P-Mu C-Si(1-X)O(X):H Layer*. 35th Ieee Photovoltaic Specialists Conference, (2010).

133 **Rau U. & Schmidt M.** *Electronic properties of ZnO/CdS/Cu(In,Ga)Se-2 solar cells aspects of heterojunction formation*. Thin Solid Films 387, 141–146, (2001).

134 **Rau U., Grabitz P. O. & Werner J. H.** *Resistive limitations to spatially inhomogeneous electronic losses in solar cells*. Appl Phys Lett 85, 6010, (2004).

135 **Dominé D., Bailat J., Steinhauser J. *et al.*** *Micromorph solar cell optimization using a zno layer as intermediate reflector*. 4th WC-PEC, (2006).

136 **Green M. A., Emery K., Hishikawa Y. & Warta W.** *Solar cell efficiency tables (version 37)*. Progress in Photovoltaics: Research and Applications 19, 84-92, (2011).

137 **Breitenstein O. & Langenkamp M.** *Lock-in Thermography.* ISBN 3-540-43439-9, (Springer, 2003).

138 **Niwano M., Kageyama J., Kurita K. *et al.*** *Infrared-Spectroscopy Study of Initial-Stages of Oxidation of Hydrogen-Terminated Si Surfaces Stored in Air*. J Appl Phys 76, 2157–2163, (1994).

139 **Smets A. H. M., Matsui T. & Kondo M.** *Infrared analysis of the bulk silicon-hydrogen bonds as an optimization tool for high-rate deposition of microcrystalline silicon solar cells*. Appl Phys Lett 92, (2008).

140 **Frammelsberger W., Lechner P., Lechner R. *et al.*** *Status of the development of Micromorph cells and modules at schott solar thin film GmbH.* in Proceedings of 25th EU-PVSEC and 5th WC-PEC, 2788–2792, 2010, Valencia, Spain.

141 **Python M.** *Microcrystalline silicon solar cells : growth and defects.* PhD thesis, University of Neuchâtel, (2009).

142 **Steinhauser J., Fay S., Oliveira N. *et al.*** *Electrical transport in boron-doped polycrystalline zinc oxide thin films*. Physica status solidi (a) 205, 1983–1987, (2008).

143 **Springer J., Poruba A., Mullerova L. *et al.*** *Absorption loss at nanorough silver back reflector of thin-film silicon solar cells*. J Appl Phys 95, 1427–1429, (2004).

144 **Haug F. J., Soderstrom T., Cubero O. *et al.*** *Plasmonic absorption in textured silver back reflectors of thin film solar cells*. J Appl Phys 104, (2008).

145 **Sai H., Jia H. J. & Kondo M.** *Impact of front and rear texture of thin-film microcrystalline silicon solar cells on their light trapping properties*. J Appl Phys 108, (2010).

146 **Söderström K., Haug F. J., Escarré J. *et al.*** *Highly Reflective Nanotextured Sputtererd Silver Back Reflector for Flexible High-Efficiency n-i-p Thin-film Silicon Solar Cells*. Sol Energ Mat Sol C, (submitted for publication).

147 **Repmann T.** *Stapelsolarzellen aus amorphem und mikrokristallinem Silizium.* PhD thesis, Forschungszentrum Jülich, (2003).

Acknowledgements

This work was supported by the Swiss Federal Office for Energy (grant number 101191) and by the European project ATHLET (contract 019670).

I sincerely thank Christophe Ballif for having supported and guided my work throughout my PhD thesis. With his motivation, commitment and excellent overview of the PV community, he was able to create an inspiring environment for exciting research.

Then I would like to thank the jury members, Bernd Rech, Tobias Roschek, Alan Howling, Cécile Hébert for assisting at my PhD thesis defense and for their constructive comments and corrections.

A special thank goes to my first thesis supervisor Julien Bailat, for having given me an excellent introduction to our field of research, to my second supervisor Andrea Feltrin for a fruitful continuation, and to my third supervisor Matthieu Despeisse, for his help in bringing this work to a successful end.

Furthermore, I would like to thank all my colleagues for the pleasant and motivating collaboration, and special thanks go to Didier Dominé, Mathieu Boccard, and Simon Hänni who participated significantly to the work presented here with their scientific understanding and experimental work. Warm thanks go to Adrian Billet, Didier Dominé and Corsin Battaglia for the nice atmosphere in our office.

I also thank Reto Tscharner, Cédric Bucher, Adrian Billet, Xavier Niquille, Sylvain Dunand, and Jérémie Bettex for their continuous and high-quality work in order to maintain infrastructure in excellent shape. I thank Jean-Luc Kumin and Joel Currit for their help in mechanics and I thank Hassan Laaroussi, Mary-Claude Gauteaub, Joëlle Banjac, Brigitte Khan for logistic and administrative support.

And last but not least I would like to thank all my family for continuous help and support.

Peter CUONY (Buehlmann)
Rue Desor 3
2000 Neuchâtel
peter@cuony.ch

31 years
married
2.5 children
Swiss

Electrical Engineer and PhD CANDIDATE at IMT-NE, EPFL
Analytical, Innovative, Open-minded

EXPERIENCE

During my PhD, I developed new materials and showed how they can improve thin-film silicon solar cell efficiency. I mostly worked with doped silicon oxides, to elucidate their optical and electrical properties and I was implicated in writing two patents covering the newly discovered results. I had the chance to participate in two industrial projects where we successfully transferred silicon oxide based layers to two different European companies. I enjoyed the intense collaboration with my colleagues and supervised several Bachelor and Master Projects and civil service internships.
The complete list of my scientific publications can be consulted on: http://peter.cuony.ch

STUDIES

- PhD thesis at the Institute of Microengineering (IMT) in Neuchâtel, part of the Swiss Federal Institute of Technology Lausanne (EPFL) 2007-2010
- Bachelor and Master Degree in Electrical Engineering at EPFL, in Lausanne 2001-2006
- Exchange Year at Indian Institute of Technology Madras in India 2003-2004
- Gymnasium Bern-Kirchenfeld, Maturity (university entrance): science 1996-2001
- Exchange Year and High-School Graduation in Garwin, Iowa, USA 1997-1998

TECHNICAL SKILLS

At IMT, I worked with 3 plasma enhanced chemical vapor deposition and 3 sputtering systems and I used a broad spectrum of characterization techniques for solar cells and thin films such as JV, EQE, AFM, spectroscopic ellipsometry, Raman, FTIR and others. I have good knowledge of the Microsoft Office applications and basic knowledge with respect to various other programs in the field of mathematics, graphics, and simulations.

LANGUAGE SKILLS

Fluent in German, French and English and intermediate level in Spanish

SOCIAL SKILLS AND SPECIAL INTERESTS

I like running, climbing, skiing and soccer. I'm a certified J+S group leader for skiing, and mountaineering with regular leading activities for groups of 10-15 year olds in the mountains. I have been singing for 5 years in the choirs of Lausanne and Neuchâtel Universities. I accomplished my military training as mountaineering specialist and then changed to civil service, and worked for an environmental organization in Quito, Ecuador and an institution for alcohol addicts in St-Aubin, Switzerland.